Final Report

THERMAL POLLUTION MATHEMATICAL MODEL

(Volume Six of Seven Volumes)

VERIFICATION OF THREE-DIMENSIONAL FREE-SURFACE MODEL AT ANCLOTE ANCHORAGE

by
Samuel S. Lee, Subrata Sengupta,
S. Y. Tuann, and C. R. Lee
Department of Mechanical Engineering
University of Miami

Volume VI

August 1980

Final Report

THERMAL POLLUTION MATHEMATICAL MODEL

(Volume Six of Seven Volumes)

VERIFICATION OF THREE-DIMENSIONAL FREE-SURFACE MODEL AT ANCLOTE ANCHORAGE

Volume VI

by

Samuel S. Lee, Subrata Sengupta,
S. Y. Tuann and C. R. Lee
Department of Mechanical Engineering
University of Miami
Coral Gables, Florida 33124

Prepared for

National Aeronautics and Space Administration
and
Environmental Protection Agency
(NASA Contract NAS 10-9410)

August 1980

STANDARD TITLE PAGE

1. Report No.	2. Government Accession No.	3. Recipient's Catalog No.
CR-165623		

4. Title and Subtitle	5. Report Date
Thermal Pollution Math Model Volume VI, Verification of Three-Dimensional Free-Surface Model at Anclote Anchorage	6. Performing Organization Code: TR 43-4
7. Author(s) Drs. Samuel Lee and Subrata Sengupta; S. Y. Tuann and C. R. Lee	8. Performing Organization Report No.
9. Performing Organization Name and Address: John F. Kennedy Space Center, Kennedy Space Center, Florida 32899, Project Manager: Roy A. Bland Code PT-FAP	10. Work Unit No.
	11. Contract or Grant No.: NAS10-9410
	13. Type of Report and Period Covered: Final
12. Sponsoring Agency Name and Address: National Aeronautics and Space Administration and Environmental Protection Agency, Research Triangle Park, N.C.	14. Sponsoring Agency Code

15. Abstract

The free-surface model, presented in this volume, is for tidal estuaries and coastal regions where ambient tidal forces play an important role in the dispersal of heated water. The model is time dependent, three-dimensional and can handle irregular bottom topography. The vertical stretching coordinate is adopted for better treatment of kinematic condition at the water surface. The results include surface elevation, velocity and temperature.

The model has been verified at the Anclote Anchorage site of Florida Power Company. Two data bases at four tidal stages for winter and summer conditions were used to verify the model. Differences between measured and predicted temperatures are on an average of less than $1^{o}C$.

16. Key Words

Thermal Pollution
Math Models
Nuclear or Fossil Fuel Power Plants
Waste Heat

17. Bibliographic Control	18. Distribution
Announce in Star Category 43	Unlimited

19. Security Classif.(of this report)	20. Security Classif.(of this page)	21. No. of Pages	22. Price
None	None		

PREFACE

This report is one in a series on the University of Miami's thermal pollution models. Much of the background, formulations, solutions techniques and applications of these models has been summarized in a three-volume report by Lee and Sengupta (1978). These mathematical models were developed by the Thermal Pollution Group at the University of Miami and were funded by the National Aeronautics and Space Administration. The primary aim was to have a package of mathematical models which has general application in predicting the thermal distribution of once-through, power plant heated discharge to the aquatic ecosystem. The joint effort was planned so that the calibration and verification of these models depend on simultaneous remote sensing and ground-truth data acquisition support. The concept is the development of adequately calibrated and verified models for direct prediction of thermal dispersion by the user communities. The intended user communities include the utility companies and the regulatory agencies at the federal and state level.

The purpose of the present effort is to further verify these models at widely different sites using minimal calibration, and then to provide the program code and user's manual to the Environmental Protection Agency (EPA) for future users.

Two sites chosen were Anclote Anchorage on the west coast of Florida and Lake Keowee in South Carolina. The free-surface model was applied to Anclote Anchorage and the rigid-lid to Lake Keowee. Two data acquisition trips, one in the summer and the other in the winter, were carried out at each site. The acquisition was a collaborated effort jointly by the UM, EPA, NASA-KSC (Kennedy Space Center) and the corresponding utility company personnels.

The two-year project consisted of two phases. During Phase I, the individual model was modified and calibrated to fit the corresponding site; then the model was verified against the remote sensing isotherms and in-situ measured velocity and temperature data under both summer and winter conditions. In general, the computed isotherms were comparable with isotherms based on remote sensing. In Phase II, source programs of both models were documented and transferred to the EPA, and the user's guides were prepared to familiarize the potential users. The results of the two-year effort are summarized in a set of three final reports.

ABSTRACT

To assess the environmental impact of waste heat disposal by power plant operation into natural water bodies, mathematical models are essential, especially for predictive studies. The Thermal Pollution Group at the University of Miami has developed a package of models for this purpose. A joint effort with EPA, NASA, Duke Power Company and Florida Power Company was conducted to verify these models with remote sensed IR data and in-situ measurements.

The free-surface model, presented in this volume, is for tidal estuaries and coastal regions where ambient tidal forces play an important role in the dispersal of heated water. The model is time dependent, three dimensional and can handle irregular bottom topography. The vertical stretching coordinate is adopted for better treatment of kinematic condition at the water surface. The results include surface elevation, velocity and temperature.

The model has been verified at the Anclote Anchorage site of Florida Power Company. Two data bases at four tidal stages for winter and summer conditions were used to verify the model. Differences between measured and predicted temperatures are on an average of less than 1°C.

CONTENTS

FIGURES

FIGURES

FIGURES

FIGURES

TABLES

SYMBOLS

A_v	Vertical eddy viscosity, $cm^2\ sec^{-1}$
H_h	Horizontal eddy diffusivity, $cm^2\ sec^{-1}$
B_v	Vertical eddy diffusivity, $cm^2\ sec^{-1}$
f	Coriolis factor, sec^{-1}
	Relative humidity in fraction of unit
g	Acceleration of gravity, $cm\ sec^{-2}$
h	Local water depth with respect to mean sea level, cm
H	Total water depth, cm
I	Node index in the direction of the x-axis
J	Node index in the direction of the y-axis
K	Node index in the direction of the z-axis
K_s	Surface heat exchange coefficient, BTU ft^{-2} day deg
L	Reference length, cm
P	Pressure, dynes cm
t	Time, sec
T	Water temperature, deg C
T_a	Air temperature, deg F
T_{ave}	Average of air and dewpoint temperatures, deg F
T_d	Dewpoint temperature, deg F
T_e	Equilibrium temperature, deg F
T_s	Ambient surface temperature, deg F
u	Component of water velocity along x-axis, $cm\ sec^{-1}$
	Wind speed, mph
v	Component of water velocity along y-axis, $cm\ sec^{-1}$
w	Component of water velocity along z-axis, $cm\ sec^{-1}$
η	Displacement of the free surface with respect to the mean water level, cm
ρ	Water density, $gm\ cm^{-3}$
Ω	Nondimensional vertical fluid velocity
σ	Nondimensional vertical coordinate

ACKNOWLEDGMENTS

This work was supported by a contract from the National Aeronautics and Space Administration (NASA-KSC) and the Environmental Protection Agency (EPA-RTP).

The authors express their sincere gratitude for the technical and managerial support of Mr. Roy A. Bland, the NASA-KSC project manager of this contract, and the NASA-KSC remote sensing group. Special thanks are also due to Dr. Theodore G. Brna, the EPA-RTP project manager, for his guidance and support of the experiments, and to Mr. Albert W. Morneault from Florida Power Company (FPC), Tarpon Springs, and his data collection group for data acquisition. The support of Mr. Charles H. Kaplan of EPA was extremely helpful in the planning and reviewing of this project.

SECTION 1

INTRODUCTION

BACKGROUND

The problem of disposing of the waste heat produced as a result of generation of electrical energy, whether by fossil-fuel or by nuclear-fuel, is a dominant consideration in making power production compatible with ecological concerns. For every unit of energy converted to electricity, approximately two units are rejected in the form of waste heat. The ultimate heat sink for the heat removed by the condenser-cooling-water system is the earth's atmosphere. The cooling water taken from natural or man-made water bodies is circulated once through the condenser, and the heated water is discharged back to the same bodies, which usually are lakes, rivers, estuaries, or coastal waters. Eventually, the heat is transferred to the atmosphere through evaporation, radiation and conduction over relatively large areas at the air-water interface.

The use of natural water bodies as an intermediate means for disposal of waste heat must take into account the effect upon the environment of the circulation and temperature rises produced in the receiving water. The rate of oxygen consumption by aquatic species increases with rising water temperature; however, the ability of water to hold dissolved oxygen decreases with rising water temperature. There are possibilities of impairment of biological functions of fish and of breaking important links in the food chain. The lethal effects of thermal pollution are sometimes obvious; the sublethal effects on hydrobiological systems and waste assimilation capacities are not easy to foresee unless interactive hydrothermal, chemical and biological studies are conducted in an integrated fashion.

Accurate understanding of hydrothermal behavior of the receiving water bodies is an important factor in a power plant system for the following reasons:

1. To provide a priori information about the nature and extent of thermal impact on the aquatic life forms.

2. To analyse the circulation pattern of the receiving water body so that recirculation between intake and outlet and consequent decrease in cooling efficiency can be minimized.

3. To assess the thermal impact on the aquatic life forms existing in the receiving ecosystem so that post-operational remedies can be done to

reduce the hazards.

It is therefore apparent that not only environmental but planning and designing interests also are at stake.

The above-mentioned objectives can only be met by having large data sets over the entire discharge flowfield under various extreme hydrological and meteorological conditions. Measurement for temperature and velocity made over the affected domain could be used to develop maps for velocity and temperature distributions. These in-situ measurements can serve for diagnostic and monitoring purposes under limited circumstances; however, they are not relevant for predictive objective. The physical modeling is useful for hydrodynamical behavior studies when properly verified; it is generally expensive and time-consuming. Frequently, physical dimensions necessitate distortion in the model, making exact dynamic similitude impossible. Mathematical modeling is tractable and predictive; it has become a powerful means in simulating complex environmental flows.

In order to establish the rationale of model formulation, the physical mechanisms underlying the heat dispersion from a heated discharge need to be outlined. The following mechanisms govern the heat dispersal.

1. Entrainment of ambient fluid into the thermal discharge.

2. Buoyant spreading of discharged heated effluent.

3. Diffusion by ambient turbulence.

4. Interaction with ambient currents.

5. Heat loss to the atmosphere through air-water interface.

The first four mechanisms redistribute heat and momentum in the receiving water body. The last mechanism eventually transfers heat to the atmosphere. It has been customary, therefore, to make assumptions and approximations which enable the model solvable. For example, the ambient turbulence is considered by assuming the eddy viscosity and diffusivity dependent on the mean velocity field. There assumptions necessitate careful calibration of models to assure reliability. Large data bases are needed for proper calibration, especially for three-dimensional, time-dependent models. Remote sensing is the only available method of obtaining large synoptic data bases. Sengupta et al. (1975) has discussed the need for remotely sensed data for adequate development of time-dependent, hydrothermal models.

UNIVERSITY OF MIAMI MODELS

Critical evaluation of mathematical models used for thermal pollution analysis has been made by Dunn et al. (1975). They compared the per-

formance of various models in predicting a standard data base. A general conclusion that can be made from their analysis is that, though some models may perform well under certain conditions, a generalized three-dimensional model which accounts for wind, current, tide, bottom topography and diverse meteorological conditions is yet to be developed. One of the first three-dimensional models was by Waldrop and Farmer (1973, 1974 a, b). This model was essentially a free-surface formulation. One of the first three-dimensional models which adequately accounts for bottom topography and comprehensive meteorological conditions was a rigid-lid model developed by Sengupta and Lick (1974 a, 1976). They used a vertical stretching to convert the variable depth, a concept customarily adopted by numerical weather forecasting peoples.

The thermal pollution research team at the University of Miami has for the past several years been developing a package of three-dimensional mathematical models which could have general application to problems of power plant heated discharge to the aquatic ecosystem. The primary motivation behind the effort was to develop a series of models with minimal restrictive assumptions, enabling applications to diverse basin configurations and to various driving forces of ambient flow. The effort is closely integrated with simultaneous remote sensing and ground-truth data acquisition support. Our aim is to develop adequately calibrated and verified models for production purpose; that is, for direct application by the user communities. The user communities are the power industries and the regulatory agencies like the Environmental Protection Agency and the Nuclear Regulatory Commission.

For the time-dependent, free-surface model which is the main concern of this volume, the governing equations are the incompressible Navier-Stokes equations, conservation of mass, energy and an equation of state. The conventional hydrostatic and Boussinesq approximations are made. The mean velocity field closure is assumed in defining eddy viscosity coefficient. The boundary conditions at water-land interfaces are no-slip, no-normal velocity and adiabatic conditions. At the air-water interface, wind stress and heat transfer coefficients are specified. At open-to-sea boundaries, conditions are specified for surface elevation and temperature. Otherwise, normal derivatives of temperature and velocity are equal to zero. Initial condition is assumed to be equilibrium; that is "cool start." Conditions at intake and outlet are completely specified in space and time.

The features of the UM's free-surface model can be summarized as follows:

1. Gravity, earth's rotation, nonlinear inertia and bottom friction terms are included in the hydromechanic part.

2. The driving forces include wind, tide, river outflow and power plant intake and discharge.

3. Convection, diffusion and heat transport at water surface are

included in the thermodynamic part.

4. The σ system of coordinate, devised by a meteorologist for avoiding difficulties at the free surface, is incorporated.

5. It predicts spatial and temporal variation of surface elevation due to tide surge and wind set-up.

6. It has means for graphically representing velocity and temperature fields.

This free-surface model is general enough to be applied with minor modifications to a large variety of sites, such as lakes, rivers, estuaries, tidal inlets and coastlines. This model has been successfully applied to Lake Okeechobee for hydrodynamic study, Biscayne Bay for dispersion study and Hutchinson Island for hydrothermal study. This model can simulate the receiving water body in the far-field and detailed features of thermal plumes and mixing zones in the near-field.

DESCRIPTION OF ANCLOTE ANCHORAGE

The UM's thermal pollution team has been studying the Anclote Anchorage on the west central coast of Florida near the town of Tarpon Springs (Figure 1) since the summer of 1978. The Anclote power plant, operated by the Florida Power Corporation, has two 515 MW, oil-fired electrical generating units. The once-through cooling water for the two units is to be drawn from the Anclote River by six pumps delivering a total of 930,000 gpm. After a temperature rise of 6.1°C, this water is diluted with a flow of 1,060,000 gpm at ambient temperature to reduce the temperature rise to 2.8°C at the outlet to Anclote Anchorage. This mixing is done in a 1250 meter-long man-made channel leading to an outlet.

The Anclote Anchorage (Figure 2) consists of shallow coastal water separated from the Gulf of Mexico by a series of barrier island parallel to the coast line. The Anchorage has a relatively unrestricted exchange of water with the Gulf through natural channels to the north and to the south of the Anclote Keys. Depth ranges from 0.3 to 3.6 m, with a mean of 1.8 m. Shallow regions of less than 0.6 m comprise approximately 5 km in length and 6 km in average width. Currents in the Anchorage are tidal- and wind-driven, with the tide entering from the south stronger than that from the north.

Prior to power plant construction, the Marine Science Institute of the University of South Florida (USF) was contracted by the Florida Power Corporation (FPC) to investigate the possible environmental impact of the plant operation. The USF's Anclote Environmental Project beginning in 1970 was comprehensive in nature. Much of their efforts was to obtain a detailed picture of the Anclote environment prior to alternation of the environment by power plant construction and operation.

Valuable background data were collected in a variety of areas, including general physical characteristics of the Anclote River and Anchorage, suspended sediments, turbidity, temperature, salinity, water quality, seagrasses, benthic invertebrates and fishes. All information was applied to preconstruction plant design in order to minimize environmental impact. This application resulted in major changes in intake and discharge channel dredging, outfall design and thermal dishcarge characteristics. The same team also monitored the undergoing changes of the environment during and after the dredging operations for the intake and discharge channels.

Unit I of the Anclote Power Plant commenced operation during the fall of 1974, after which a post-operation ecological monitoring program for evaluating the nature and degree of thermal impact was carried out and maintained by the USF. At the time of this study, the planned Unit 2 was still pending permission.

Since the nature of thermal impact at Anclote Anchorage is not clear, it is decided that a joint effort by UM, NASA-KSC, EPA and FPC to use a three-dimensional model with support of remotely sensed data and in-situ data for calibration and verification may be appropriate to study this thermal impact at Anclote. It is for this purpose that the existing free-surface model was adapted to the Anclote site, as we have done in its application to Biscayne Bay. As the original program was developed for well-mixed shallow coastal waters, except for some modification to accommodate the tidally influenced Anclote River flow, the program was ready for calibration. We shall account for this application in a later section.

SECTION 2

CONCLUSIONS

A numerical simulation of the hydrothermal characteristics of a well-mixed, shallow, coastal water body at Anclote Anchorage under the effect of waste heat disposal by a power plant in the summer and winter situations is presented. The model takes into consideration the effects of Coriolis force, wind, tide, bottom topography, power plant intake and discharge, river outflow and surface heat transfer. Results obtained with the model have been verified with in-situ measurements and IR data. Reasonable agreement has been obtained. From the experiences and results of these simulation runs, the conclusions may be summarized as follows:

1. Inputs for the description of open boundaries, discharge, wind and heat transfer must be found experimentally from field data for accurate hydrothermal predictions.

2. The shape of the thermal plume was dominated by the stage of the tidal cycles, as clearly exhibited in the plots of IR and calculated isotherms.

3. Tide plays a main role in the Anchorage as a driving force; its influence from the south is stronger than that from the north. A dividing line is observed. On the northern side of this line, the water flows north, while on the south side it flows south. At this ridge line, the water has minimal transverse motion. The location of this line varies with time as the tide from both ends is not in phase.

4. It is important to impose correct boundary conditions, especially the correct tidal functions on the south and north boundaries, for obtaining a good prediction of the thermal plume.

5. Wind does appear to be an important external force affecting surface currents. It is found that the surface currents are close to the wind direction when wind speed is in excess of 15 mph.

6. An estimation of the Rossby Number revealed that the nonlinear inertia terms can be safely neglected for Anclote site. This is because the ratio of inertia force to the Coriolis force is small compared with unity.

7. The recirculation of cooling water should be prevented by proper design of intake and discharge location, since the heated water

recirculating back to the intake will cause a reduction in the efficiency of the power plant.

Numerically the model behaves very well for both summer and winter simulation runs. The model is able to include very shallow water depths. A problem associated with the analysis is computing the response of the thermal plume to very strong winds such as hurricane, since the formula used in this study to estimate the vertical eddy viscosity coefficient does not involve wind speed. A brief investigation was made regarding the effects of hurricane-force winds. It was found that currents become unrealistically large in such cases unless the vertical eddy viscosity coefficient was increased with wind speed. This general problem of computing the response of shallow coastal water to very strong winds requires additional research.

SECTION 3

RECOMMENDATIONS

One of the difficulties encountered in model verification with the remote sensing temperature field was the lack of measured current data of comparable accuracy. We believe that, at the verification state, the accuracy of velocity calculation needs to be assessed in order to clear ambiguities about the limitations of comparison of calculated surface isothermal maps with the IR imagery mosaics.

In the initial phase of mixing, the plume shape is governed by the volume of discharge, the geometry of outlet and the initial temperature difference between the discharge and receiving waters. Consequently, for predicting the details of the near-field thermal plume a finer grid is needed near the outlet. Thus, a combination of grid structures would be desired for the computation with a course grid for far-field and a fine grid for the near-field. This, however, would result in higher computational costs.

For any non-reactive, dissolved, chemical constituent, the governing transport equation is completely analogous to the temperature equation of the present model. Thus, without much endeavor, the model can be extended to include the dispersal of these constituents.

For situations of deep and stratified water, the bouyancy effects are important factors in shaping the plume. Therefore, a coupled system of momentum and energy equations should be considered as the basis of formulation.

SECTION 4

MATHEMATICAL FORMULATION AND MODEL DESCRIPTION

GENERAL BACKGROUND ON FREE-SURFACE (TIDAL) MODELS

Recent concern about the ecological future of our estuaries and coastal waters has generated a need for practical and reliable methods of predicting the environmental impact of the widespread use of natural seashores as industrial zones. The tendency of setting up once-through, seawater-cooled, fossil- or nuclear-fueled power generation plants is increasingly strong, due to the demand for electrical power at competitive prices and prohibitive costs of cooling towers and man-made cooling lakes. Thus, it is of special importance that mathematical models be developed for simulating and predicting thermal pollution. The estuaries, tidal inlets and coastal waters which serve as the receiving body for waste heat are usually of complex configuration and topography. The flow is driven by tide, wind, run off and buoyancy force. Thus, a complete hydrothermal model for coastal waters must, in addition to solving the three-dimensional equations of mass, momentum and energy, include the salinity equation to determine closely the local density. A model of this type is still far beyond feasibility. Therefore, assumptions and approximations must be made to render the system closed and tractable.

Hindwood and Wallis (1975) have compiled a bibliography of 141 papers concerning computer models for tidal hydrodynamics. In general, the output from the hydrodynamic/hydraulic model is recorded on magnetic tape. This tape is then entered into the thermal dispersion model. The dispersion model operates through successive solution of the finite difference equations for the change of temperature (with time and space) due to diffusion (eddy mixing), advection (velocity transport), and heat flux through the water surface. Therefore, it is appropriate to say that the hydrodynamic/hydraulic model serves as the backbone to the thermal pollution model of the well-mixed water. Commonly, the hydrodynamic models are two-dimensional and based on the vertically-integrated equations of motion and continuity for an incompressible fluid. Thus, the vertical structure of the circulation was not considered. This procedure turned out to be sufficient for the investigation of tidal processes.

Of the two-dimensional models, we should briefly mention the Leendertse (1967) model and Reid and Bodine (1969) model for their comprehensiveness and popularity. In Leendertse's model, the unknowns are vertically-averaged velocities and water level; the bottom friction is in terms of Chezy coefficient which is to be calibrated. Reid and Bodine used

vertically integrated transports and water level as unknowns and Darcy friction coefficient. Both models used the space-staggered system which gives the simplest scheme consistent with the control volume approach to deriving difference equations. However, in the Leendertse model, the finite difference equations are expressed in an alternating direction implicit (ADI) form, with two successive time-level operations being executed during each time cycle; while in the Reid and Bodine model a time-split explicit (leap-frog) method is used for marching forward, the time step is limited by numerical stability requirement (cf. Platzman, 1958), less than the value $\min(\Delta x, \Delta y) / 2gD_{max}$), in which D_{max} is the maximum depth.

In the context of two-dimensional tidally-driven flows, we should include the finite element method models which were developed in the last few years. This is a method combining finite element for spacial discretization and finite difference for temporal discretization. The variables in discrete element is approximated by simple polynomials whose coefficients are expressed in terms of nodal values of the variables and their derivatives. Correctly formulated, the physical conservation principles are satisfied and, in theory, the element shape and interpolation function are quite free as long as certain compactibility conditions are satisfied. The freedom of using irregular grid to fit complicated geometry is the primary advantage of this method.

At the present stage, FEM (finite element method) models for tidal hydrodynamics are all two-dimensional. Wang's CAFE (Circulation Analysis by Finite Element) model and Brebbia's shallow water model (in his Finite Element Hydrodynamic Problem Orientated Language (FEHPOL) package) are both productive. CAFE (Wang, 1978) has a linear triangular element for all variables, vertically-integrated transports and water level, and has split-time method for time integration. Patridge and Brebbia (1976) use a six-node, quadratic triangular element for all variables; in this case, they are vertically-averaged velocities and free-surface elevation. The 4th order Runge-Kutta (explicit) and Trapezoidal Rule (implicit) methods are used for time integration. In general, the flexibility of the grid layout, the consistency of FEM formulation and the easiness in taking into account the spatially variable properties are the advantages. However, the time integration scheme is very much problem-oriented, and more fruitful research could lead to a better time integration method. It is worthwhile to point out that, in the FDE (finite difference method) for two-dimensional hydrodynamics, the explicit method had advantage over the implicit method in terms of computer time.

In the classical approach of two-dimensional computations of tides and storm surges in a shallow sea, it is assumed that the velocities are uniform over the vertical; however, the vertically uniform velocities are of little evidence in the case of those propagation and transport processes which are essentially vertically structured. The application of a three-dimensional model requires extensive computation on a large number of grid points if relatively good resolution is needed. This precludes the

use of the implicit method which requires that matrix solutions of a row or column of variables be found. In fact, Leendertse et al. (1973) developed a three-dimensional model which really uses the explicit leap-frog method instead of the implicit methods such as the ADI method Leendertse used in his two-dimensional model.

Leendertse's three-dimensional model is a vertically-integrated, multi-layered model, in which the usual assumptions of hydrostatic pressure, imcompressibility and small density variation are made. The interfaces are assumed as fixed horizontal planes, while the bottom layer has its lower face fit to bottom topography and the top layer has its upper face representing the free surface. The top layer has a time-variable height. The other layers may be intersected by the bottom and have a height which is dependent on the bathymetry. The description of the finite-difference equations from the differential equations is accomplished in two steps: First, the equations for the layer are derived by vertically integrating the variables over the layer thickness, and subsequently, finite difference approximations for the layer equation are developed. Thus, the vertically-integrated momentum, heat, and salt balance equations can be presented for each layer. From the continuity equation, the time derivative of the free surface and the vertical velocity at the interfaces can be derived. The horizontal pressure gradient in each layer is approximated from hydrostatic equation with layer-averaged density, which is tied to salt and heat through the equation of state.

In Leendertse's model (Leendertse and Liu, 1975), the balance of momentum fluxes between the local and convective accelerations, pressure gradient, Coriolis force, lateral diffusion, and interfacial stresses is accounted for within each layer; likewise, the balance of heat fluxes between the time rate, convection, lateral diffusion and cross-layer diffusion is for each layer; so is the salt balance. The same lateral diffusion coefficient is used for both heat and salt. Even postulations are introduced to express the vertical momentum, salt and heat exchange under vertically stable or unstable stratifications; these layer-averaged equations clearly point out the foremost problem of his model. There are many parameters to be determined and an enormous amount of supporting field data is needed.

Leendertse et al. (1973) discuss the numerical finite difference solution scheme in some detail. The explicit leap-frog method is used to avoid the difficulties encountered by ADI. The spatial grid structure is cell-like with u, v and w components at the center of the corresponding normal faces and pressure (p), density (ρ), salinity (S) and temperature (T) at the center of the cell. For programming reasons, the bottom must be approximated in steps of layer thickness, causing some numerical problems at the jumps. But the most troublesome one is the specification of boundary conditions for the seaward boundary of the model, since field measurements do not provide enough data to describe that boundary completely. Numerical experiments involving the simulations of hydrodynamic behavior of both Chesapeake Bay and San Francisco Bay are given

with a graphical representation of velocity, salinity and temperature results.

A specific three-dimensional model has been developed by Sundermann (1974) and applied to the North Sea. In the model, the usual assumption of a hydrostatic pressure and the Boussinesq approximation for the turbulent Reynolds stresses are made. However, no horizontal turbulent exchange of momentum is retained. To fit the vertical velocity profiles of a wind-generated surface current and a compensating countercurrent near the bottom, as observed in nature, it was found necessary to include a bottom boundary layer that can be modeled by having a vertical eddy viscosity dependent on the depth. The spatial discretization is carried out by means of a cubic grid net, while the explicit method of Crank-Nicolson has been used for approximating the vertical diffusion term.

The σ system of coordinates, devised by N. A. Phillips (1957), was used for numerical forecasting. Its advantages are that the kinematic boundary conditions at free-surface and bottom are made simple and a vertical stretching is used to avoid the difficulty of using regular grid net for irregular bathymetry. Briefly, the (x, y, σ, t) system is used to replace (x, y, z, t), and the free surface and bottom are transformed into $\sigma = 0$ and $\sigma = -1$ surfaces. The modified vertical velocity, $\Omega = d\sigma/dt$, is zero at both these surfaces, while the actual vertical velocity is $w = d\eta/dt$ at the free surface and $w = 0$ at the bottom.

Freeman et al. (1972) introduced σ-transformation into their three-dimensional free-surface model for wind-generated circulation in a closed region. Sengupta and Lick (1974) incorporated σ-transformation in their rigid-lid model for wind-driven circulation in lakes. However, the transformation was used only for the advantage of vertical stretching so that a constant vertical grid size, $\Delta\sigma$, can be used throughout the domain. This rigid-lid approximation effectively eliminates surface gravity wave by imposing a zero-actual vertical velocity at the water surface. An additional equation, a Poisson equation for surface pressure which contains the rigid-lid condition, can be derived. Therefore, at each time step the Poisson equation has to be solved by iterative method. However, for large problems, particularly when normal derivative boundary conditions are used, this can be a time consuming part of the calculation procedure. As mentioned, this model is not for tidally-driven coastal flow.

The present free-surface model is similar to that of Freeman et al. in using σ-coordinate system. However, the horizontal turbulent exchange of momentum terms is neglected while the vertical turbulent exchange term is approximated by using the Dufort-Frankel differencing to ease the constraint on numerical stability due to neglect of the horizontal diffusion terms. This model was developed by Carter (1977) for his study on wind-driven flow in Lake Okeechobee. Later, Sengupta et al. (1978) applied it to tidal flow in Biscayne Bay.

GOVERNING EQUATIONS AND BOUNDARY CONDITIONS

Flow of water in estuaries and coastal areas is predominantly hori-

zontal. Vertical velocities do occur and are important, as they characterize the vertical circulation. However, the vertical acceleration is extremely small in comparison with the gravitational acceleration, so that the vertical acceleration is neglected and the vertical equation of motion is then replaced by the hydrostatic assumption. The effect of density variations on the inertial and diffusion terms in the horizontal equations of motion is neglected. Density variation is retained in the lateral pressure gradient terms; that is, the effect of bouyancy is accounted for by allowing density variations in the horizontal pressure gradients which influence the fluid motion through the horizontal momentum equations. Consequently, the continuity equation replaces the mass conservation equation. In the estuaries, the density is influenced by the salinity and temperature; in this model, the density will be taken dependent only on the temperature.

For turbulent closure, the Boussinesq approximation for the turbulent Reynolds stresses is made, and lateral dispersion of momentum is further assumed unimportant when compared to the rest of the terms in the horizontal equations of motion. The vertical eddy viscosity, the vertical and horizontal eddy diffusivity of temperature are assumed to be constants, although the horizontal eddy diffusivity has orders of magnitude larger than the vertical eddy diffusivity, being due to the much larger horizontal characteristic length, L, in comparison with the vertical characteristic length, H.

With these conditions, we can write the set of governing equations expressing the conservation of mass, mementum, and energy in incompressible flow:

$$\frac{\partial u}{\partial t} + \frac{\partial uu}{\partial x} + \frac{\partial uv}{\partial y} + \frac{\partial uw}{\partial z} - fv + \frac{1}{\rho}\frac{\partial p}{\partial x} - A_v\frac{\partial^2 u}{\partial z^2} = 0 \qquad (1)$$

$$\frac{\partial v}{\partial t} + \frac{\partial uv}{\partial x} + \frac{\partial vv}{\partial y} + \frac{\partial vw}{\partial z} + fu + \frac{1}{\rho}\frac{\partial p}{\partial y} - A_v\frac{\partial^2 v}{\partial z^2} = 0 \qquad (2)$$

$$\frac{\partial p}{\partial z} + \rho g = 0 \qquad (3)$$

$$\frac{\partial u}{\partial x} + \frac{\partial v}{\partial y} + \frac{\partial w}{\partial z} = 0 \qquad (4)$$

$$\frac{\partial T}{\partial t} + \frac{\partial uT}{\partial x} + \frac{\partial vT}{\partial y} + \frac{\partial wT}{\partial z} - B_h\left(\frac{\partial^2 T}{\partial x^2} + \frac{\partial^2 T}{\partial y^2}\right) - B_v\frac{\partial^2 T}{\partial z^2} = 0 \qquad (5)$$

$$\rho = \rho(T) \qquad (6)$$

where x, y, z = Cartesian coordinates positive eastward, northward and upward, respectively

u, v, w = Respective components of velocity in x, y, z direction

t = Time

p = Pressure

ρ = Density

T = Temperature

f = Coriolis parameter

g = Gravitational acceleration

A_v = Vertical eddy viscosity

B_h = Horizontal eddy diffusivity

B_v = Vertical eddy diffusivity

The first three equations represent the equations of motion. Equation (4) is the equation of continuity, and Equation (5) represents the energy equation. The equation of state, Equation (6), expresses the relation between the density and the temperature. For a more complete representation of an estuarine ecosystem, an equation expressing the balance of the salts dissolved in the water should be included together with balance equations of dissolved substances that are important to the analysis. All these equations have the same form as Equation (5). If salinity is included then the density should be related to both salinity and temperature.

Boundary conditions for the above equations must be specified:

$$u = v = w = 0 \qquad \text{at } z = -h(x, y) \tag{7}$$

$$\left.\begin{aligned} p &= 0 && (8a)\\ \frac{\partial u}{\partial z} &= \frac{\tau_x}{\rho A_v}, \quad \frac{\partial v}{\partial z} = \frac{\tau_y}{\rho A_v} && (8b)\\ \frac{\partial T}{\partial z} &= \frac{K_s}{\rho C_p B_v}(T_e - T_s) && (8c)\\ \frac{\partial \eta}{\partial t} &+ u\frac{\partial \eta}{\partial x} + v\frac{\partial \eta}{\partial y} - w = 0 && (8d) \end{aligned}\right\} \quad \text{at } z = \eta(x, y, t)$$

where η = Free-surface elevation above mean water level

τ_x, τ_y = Surface wind stresses

C_p = Specific heat at constant pressure

K_s = Surface heat transfer coefficient

T_e = Equilibrium temperature

T_s = Surface water temperature

Also, boundary conditions at closed and open boundaries must be known.

One major difficulty in the treatment of the free-surface model is the fulfillment of kinematic condition at the free surface. The approach used in the model is to follow a vertical stretching transformation suggested by Phillips (1957) and used successively in lake circulation studies by Freeman et al. (1972). Using this σ-transformation, the free surface becomes a fixed, flat surface and the variable depth bottom becomes a fixed, flat bottom of constant depth. Thus, this method allows easy adaptation to various bottom topographies, and a constant vertical grid size can be used throughout the domain.

With respect to the mean water level (MWL), z is $\eta(x, y, t)$ at the free surface and $-h(x, y)$ at the bottom. The σ-transformation of the vertical coordinate for the free-surface model is obtained by introducing

$$\sigma = \frac{z - \eta(x, y, t)}{h(x, y) + \eta(x, y, t)} = \frac{z - \eta}{H(x, y, t)} \tag{9}$$

where $H = h + \eta$ is the total depth measured from local water surface. Figure 2 shows the (x, y, σ) coordinate system. Note that the value of σ decreases monotonically from zero at the free surface to minus unity at the bottom. The modified vertical velocity, Ω, is clearly zero at both free surface and bottom. From Equation (9), the actual vertical velocity, w, is related to Ω by

$$w = (h + \eta)\Omega + (\sigma + 1)\frac{d\eta}{dt} + \sigma\left(u\frac{\partial h}{\partial x} + v\frac{\partial h}{\partial y}\right) \tag{10}$$

Differential transformation relationships are required to convert equations in (x, y, z) to those in $(x, y\ \sigma)$. The first derivatives can be written as

$$\left(\frac{\partial F}{\partial x}\right)_{y,z,t} = \left(\frac{\partial F}{\partial x}\right)_{y,\sigma,t} - \frac{1}{H}\left(\sigma\frac{\partial H}{\partial x} + \frac{\partial \eta}{\partial x}\right)\frac{\partial F}{\partial \sigma} \tag{11a}$$

$$\left(\frac{\partial F}{\partial y}\right)_{x,z,t} = \left(\frac{\partial F}{\partial y}\right)_{x,\sigma,t} - \frac{1}{H}\left(\sigma\frac{\partial H}{\partial y} + \frac{\partial \eta}{\partial y}\right)\frac{\partial F}{\partial \sigma} \tag{11b}$$

$$\left(\frac{\partial F}{\partial z}\right)_{x,y,t} = \frac{1}{H}\frac{\partial F}{\partial \sigma} \tag{11c}$$

where F is any dependent variable and $H = h + \eta$ is the total depth and is independent of σ. The continuity equation can be written as

$$\frac{\partial Hu}{\partial x} + \frac{\partial Hv}{\partial y} + H\frac{\partial \Omega}{\partial \sigma} + \frac{\partial \eta}{\partial t} = 0 \tag{12}$$

By integrating Equation (12) from the bottom to the surface and observing the fact that Ω vanishes at either face, we obtain the first useful form of the continuity equation.

$$\frac{\partial \eta}{\partial t} = -\int_{-1}^{0}\left(\frac{\partial Hu}{\partial x} + \frac{\partial Hv}{\partial y}\right)d\sigma \tag{13}$$

The horizontal momentum equations are

$$\frac{\partial Hu}{\partial t} + \frac{\partial Huu}{\partial x} + \frac{\partial Hvu}{\partial y} + H\frac{\partial \Omega u}{\partial \sigma} + (1+\sigma)\frac{\partial u}{\partial \sigma}\frac{\partial \eta}{\partial t} - fvH$$

$$= -\frac{H}{\rho}\frac{\partial p}{\partial x} - gH\left(\sigma\frac{\partial H}{\partial x} + \frac{\partial \eta}{\partial x}\right) + \frac{A_v}{H}\frac{\partial^2 u}{\partial \sigma^2} \tag{14}$$

$$\frac{\partial Hv}{\partial t} + \frac{\partial Huv}{\partial x} + \frac{\partial Hvv}{\partial y} + H\frac{\partial \Omega v}{\partial \sigma} + (1+\sigma)\frac{\partial v}{\partial \sigma}\frac{\partial \eta}{\partial t} + fuH$$

$$= -\frac{H}{\rho}\frac{\partial p}{\partial y} - gH\left(\sigma\frac{\partial H}{\partial y} + \frac{\partial \eta}{\partial y}\right) + \frac{A_v}{H}\frac{\partial^2 v}{\partial \sigma^2} \tag{15}$$

The energy equation can be written as

$$\frac{\partial HT}{\partial t} + \frac{\partial HuT}{\partial x} + \frac{\partial HvT}{\partial y} + H\frac{\partial \Omega T}{\partial \sigma} + (1+\sigma)\frac{\partial T}{\partial \sigma}\frac{\partial \eta}{\partial t} = B_h H\left(\frac{\partial^2 T}{\partial x^2} + \frac{\partial^2 T}{\partial y^2}\right) + \frac{B_v}{H}\frac{\partial^2 T}{\partial \sigma^2} \tag{16}$$

The coupling of momentum and energy equations may be retained via the density which is assumed to be a function of temperature only. An empirical formula

$$\rho = 1.029431 - 0.000020T - 0.000005T^2 \tag{17}$$

may be used for sea water of salinity 38 parts per thousand. The hydrostatic equation can be integrated to obtain a diagnostic equation for p.

$$p(\sigma) = -gH\int_{\rho_0}^{\sigma} (\sigma)d\sigma \tag{18}$$

The continuity equation, Equation (12), can also be integrated from the free surface to σ to yield the modified vertical velocity Ω at σ plane. Thus, a second useful form of Equation (12) yields

$$\Omega(\sigma) = \frac{\sigma}{H}\frac{\partial \eta}{\partial t} - \frac{1}{H}\int_0^{\sigma} \left(\frac{\partial Hu}{\partial x} + \frac{\partial Hv}{\partial y}\right)d\sigma \tag{19}$$

The actual vertical velocity w is recovered through relationship Equation (10). In solving parabolic-type partial-differential Equations (14)-(16) and differential Equation (13), we choose the initial conditions to be zero elevation from MWL and zero velocities. Given the initial temperature field, the boundary conditions are $u = v = w = 0$ on all solid surfaces, and at $\sigma = 0$, the wind stresses (τ_x, τ_y) are exerted; i.e.

$$\frac{A_v}{\rho H}\frac{\partial u}{\partial \sigma} = \tau_x, \quad \frac{A_v}{\rho H}\frac{\partial v}{\partial \sigma} = \tau_y \text{ at } \sigma = 0 \tag{20a,b}$$

The adiabatic conditions are assumed on all solid surfaces, and at $\sigma = 0$, the heat flux is set proportional to the difference between surface temperature T_s and equilibrium temperature T_e; i.e.

$$\frac{\rho C_p B_v}{H}\frac{\partial T}{\partial \sigma} = K_s(T_e - T_s) \text{ at } \sigma = 0 \tag{21}$$

The specification of velocities and temperatures at the open boundaries where the tide enters the basin is more difficult. In the present study, the tides outside the basin are given, and the difference of surface elevations across the open boundaries is used to determine the normal velocities there. The temperature at the open boundaries is set equal to ambient temperature. The velocities and temperature at the discharge is specified according to plant operation.

UNCOUPLED SYSTEM

The foregoing system may be uncoupled so that the hydrodynamic model for tidal-driven flow is separated from the thermal dispersion model. The former system consists of Equations (13), (14), (15) and (19), while the latter contains Equation (16) only. This decoupling amounts to an

assumption that the density variations due to the temperature rises caused by waste heat dispersion are negligibly small, so that the water is of constant density and the energy equation can be uncoupled from the continuity and momentum equations. The lateral pressure gradient is thus directly related to the gradient of the free surface.

In the present problem of shallow water flow strongly influenced by tide, the thermal dispersion is mainly caused by velocity transport and the buoyancy effect is negligible with comparison to the tidal effect. Numerically, this decoupling has two obvious advantages. Firstly, the time step of the coupled model is the same as that of the hydrodynamic model. This time step is limited by the criterion for computational stability by the explicit method; namely, Δt must satisfy the condition $c\Delta t/\Delta s << 1$, where Δs represents one of the space intervals in the three-dimensional grid and c denotes the maximum characteristic speed. In the free-surface model, c is identified with the wave speed and Δs with horizontal spacing; thus,

$$\Delta t_u \leq \frac{\min(\Delta x, \Delta y)}{\sqrt{2gH_{max}}}$$

However, the stability analysis of linearized energy equation alone yields the thermal time step to be

$$\Delta t_T \leq \frac{2}{\left[\frac{|u|}{\Delta x} + \frac{|v|}{\Delta y} + 2B_h\left(\frac{1}{\Delta x^2} + \frac{1}{\Delta y^2}\right)\right]}$$

where u and v are the maximum particle velocities in x and y direction respectively. For the present problem, these time steps are 50 sec and 400 sec respectively; therefore, in using Δt_u = 15 sec, we can store the hydrodynamic results every 20 steps to match Δt_T = 300 sec used in the detached calculation of temperature field. Secondly, the decoupling allows one to try for flow solution before it is used for temperature calculations, and the appropriate flow solution may be used for many temperature solutions of various initial and boundary conditions of temperature.

The effect of stratification is known to arrest the thermal dispersion. For a shallow basin having an insignificant river discharge in comparison with tidal flow, which is the case of concern, the basin is nearly well-mixed; the density variation is small. Thus, uncoupling is physically sound and numerically beneficial.

COMPUTATIONAL GRID

To represent the equations in finite difference form, a horizontal staggered computing grid system is used. Its plan version, shown in

Figure 4, indicates the arrangement of field variables in the x, y plane. Figure 5 shows a vertical fluid column subdivided into four layers; each has a constant nondimensional thickness, $\Delta\sigma = 0.25$. The u, v and w velocities are shown at their definition point respectively. Having divided the region into cells by a series of grid points which are spaced at distances of Δx, Δy, and $\Delta\sigma$, the time variable is differenced into increment of Δt such that $t = n\Delta t$, where n denotes the current time step.

The water depth, $h_{i,j}$, is specified at full-grid point where both horizontal indices, i and j, are integers; however, since the total depth, $H = h + \eta$, is needed at half-grid point, where both indices i and j have half-integer values, $(i + \frac{1}{2}, j + \frac{1}{2})$, the specified water depth at full-grid points is averaged. The following notations are used to indicate water depth at the u-, v- and η-points.

$$h^u_{i,j} = \tfrac{1}{2}(h_{i,j} + h_{i,j+1}); \quad h^v_{i,j} = \tfrac{1}{2}(h_{i,j} + h_{i+1,j}) \tag{22a,b}$$

$$h^\eta_{i,j} = \tfrac{1}{4}(h_{i,j} + h_{i+1,j} + h_{i,j+1} + h_{i+1,j+1}) \tag{23}$$

A notation for η at full-grid point is needed for calculating the nonlinear inertia terms of the momentum equations:

$$E_{i,j} = \tfrac{1}{4}(\eta^n_{i,j} + \eta^n_{i-1,j} + \eta^n_{i-1,j-1} + \eta^n_{i,j-1}) \tag{24}$$

where η^n indicates the present-time surface elevation above the mean water level. With Equations (22) to (24) and the calculated water level, $\eta^n_{i,j}$, at present time step, the present total water depths at u-, v- and η-points are respectively given by the following expressions.

$$U_{i,j} = h^u_{i,j} + \tfrac{1}{2}(\eta^n_{i-1,j} + \eta^n_{i,j}) \tag{25}$$

$$V_{i,j} = h^v_{i,j} + \tfrac{1}{2}(\eta^n_{i,j-1} + \eta^n_{i,j}) \tag{26}$$

$$H_{i,j} = h^\eta_{i,j} + \eta^n_{i,j} \tag{27}$$

In the momentum equations, values of u and v are required at half-grid points where values of these variables are not defined and thus, not stored. In these cases, values are obtained by linear interpolation between the values stored for that variable at the two neighboring points.

Therefore, the following average notations are adopted.

$$u^x_{i,j} = \tfrac{1}{2}(u^n_{i+1,j} + u^n_{i,j}) \tag{28}$$

$$v^y_{i,j} = \tfrac{1}{2}(v^n_{i,j} + v^n_{i,j+1}) \tag{29}$$

$$u^y_{i,j} = \tfrac{1}{2}(u^n_{i,j} + u^n_{i,j-1}) \tag{30}$$

$$v^x_{i,j} = \tfrac{1}{2}(v^n_{i,j} + v^n_{i-1,j}) \tag{31}$$

It is clear that notations (28) and (29) give velocities at half-grid point while notations (30) and (31) give velocities at full-grid point. No superscript n is needed for these notations. These and other variables are shown in Figure 6, where u-, v- and η-points are marked.

FINITE DIFFERENCE EQUATIONS

In the equations presented here, the space subscripts are i, j, k and are all integers, unless otherwise noted. The superscript n refers to the time level; n is present time, at which the predictive equations, (13) through (16), are used to advance the fields of u, v, η and T to new time level n + 1. In this study, first derivatives with respect to time are always represented by central time difference, i.e., for any variable F,

$$\left(\frac{\partial F}{\partial t}\right)^n_{i,j,k} = \frac{F^{n+1}_{i,j,k} - F^{n-1}_{i,j,k}}{2\Delta t} + 0(\Delta t^2) \tag{32}$$

where $0(\Delta t^2)$ refers to the order of truncation error associated with this differencing. The central time scheme is thus of second order accuracy, since the neglected terms are terms multiplied by (Δt^2) or a higher order of Δt. This indicates that the finite difference approximation can be made to approach the differential by taking sufficiently small Δt.

The second derivatives with respect to σ in Equations (14) to (16) are written in the DuFort-Frankel format, i.e.

$$\left(\frac{\partial^2 F}{\partial \sigma^2}\right)^n_{i,j,k} = \frac{F^n_{i,j,k-1} - F^{n+1}_{i,j,k} - F^{n-1}_{i,j,k} + F^n_{i,j,k+1}}{(\Delta \sigma)^2} \tag{33}$$

This expression for second order σ-derivatives when used with the central

time difference is known to avoid the inherent instability caused by using the common form of second order difference; i.e.

$$\left(\frac{\partial^2 F}{\partial \sigma^2}\right)^n_{i,j,k} = \frac{F^n_{i,j,k-1} - 2F^n_{i,j,k} + F^n_{i,j,k+1}}{(\Delta\sigma)^2}$$

The continuity equation, (13), is the predictive equation for surface elevation η, and thus applies at η-point. For convenience, we introduce, at level k of (i,j)-column, a variable

$$F^n_k = \frac{U_{i+1,j}u_{i+1,j,k} - U_{i,j}u_{i,j,k}}{\Delta x} + \frac{V_{i,j+1}v_{i,j+1,k} - V_{i,j}v_{i,j,k}}{\Delta y}$$

where the superscript n on the right-hand-side variables has been dropped. Then the finite difference form of the continuity equation can be written as

$$\frac{\eta^{n+1}_{i,j} - \eta^{n-1}_{i,j}}{2\Delta t} = \int_1^0 F^n_k d\sigma$$

Using Simpson's rule, the above equation gives

$$\eta^{n+1}_{i,j} = \eta^{n-1}_{i,j} + (2\Delta t)\frac{\Delta\sigma}{3}[F_1 + 4F_2 + 2F_3 + 4F_4 + F_5] \qquad (34)$$

It is to be noted that $F_5 = 0$ since both u and v vanish at the solid bottom.

Another form of continuity equation, (19), can be used to calculate the modified vertical velocity Ω at each level of the column. That is

$$\Omega_{i,j,k} = \frac{-(k-1)\Delta\sigma}{H_{i,j}} \frac{\eta^{n+1}_{i,j} - \eta^{n-1}_{i,j}}{2\Delta t}$$

$$+ \frac{\Delta\sigma}{H_{i,j}}[\tfrac{1}{2}F_1 + F_2 + \ldots + \tfrac{1}{2}F_k] \qquad (35)$$

where the trapezoidal formula has been used and $H_{i,j}$ is from Equation (27); i.e.

$$H_{i,j} = H^n_{i,j} = h^n_{i,j} + \eta^n_{i,j}$$

In the computation, always the present time Ω only is needed; therefore, no superscript n is required for Ω and, thus, one array is needed to store Ω. On the other hand, three arrays are necessary to store η at the past (n-1), present (n) and advance (n+1) stages.

The actual vertical velocity itself, w, is not needed in the calculation. However, when it is desired, it can be obtained from Equation (10), which is rewritten here in finite difference form.

$$
\begin{aligned}
w_{i,j,k} = H_{i,j}\,\Omega_{i,j,k} - (k-1)\Delta\sigma\Bigg[&\frac{\eta_{i,j}^{n+1} - \eta_{i,j}^{n-1}}{2\Delta t} \\
&+ u^{x}_{i,j,k}\,\frac{h^{\eta}_{i+1,j} + \eta_{i+1,j} - h^{\eta}_{i-1,j} - \eta_{i-1,j}}{2\Delta x} \\
&+ v^{y}_{i,j,k}\,\frac{h^{\eta}_{i,j+1} + \eta_{i,j+1} - h^{\eta}_{i,j-1} - \eta_{i,j-1}}{2\Delta y}\Bigg] \\
&+ \frac{\eta_{i,j}^{n+1} - \eta_{i,j}^{n-1}}{2\Delta t} + u^{x}_{i,j,k}\,\frac{\eta_{i+1,j} - \eta_{i-1,j}}{2\Delta x} \\
&+ v^{y}_{i,j,k}\,\frac{\eta_{i,j+1} - \eta_{i,j-1}}{2\Delta y}
\end{aligned}
\tag{36}
$$

The predictive equations for velocities are given by Equation (14) and Equation (15); in finite difference form, these equations are

$$
\begin{aligned}
&\frac{U_{i,j}^{n+1}u_{i,j,k}^{n+1} - U_{i,j}^{n-1}u_{i,j,k}^{n-1}}{2\Delta t} = fU_{i,j}\,\frac{v_{i,j,k} + v_{i-1,j,k} + v_{i-1,j+1,k} + v_{i,j+1,k}}{4} \\
&-gU_{i,j}\,\frac{\eta_{i,j} - \eta_{i-1,j}}{\Delta x} + \frac{A_v}{U_{i,j}}\,\frac{u_{i,j,k-1} - u_{i,j,k}^{n+1} - u_{i,j,k}^{n-1} + u_{i,j,k+1}}{(\Delta\sigma)^2} - X_{i,j,k}
\end{aligned}
\tag{37}
$$

$$
\begin{aligned}
&\frac{V_{i,j}^{n+1}v_{i,j,k}^{n+1} - V_{i,j}^{n-1}v_{i,j,k}^{n-1}}{2\Delta t} = -fV_{i,j}\,\frac{u_{i,j,k} + u_{i,j-1,k} + u_{i+1,j-1,k} + u_{i+1,j,k}}{4} \\
&-gV_{i,j}\,\frac{\eta_{i,j} - \eta_{i,j-1}}{\Delta y} + \frac{A_v}{V_{i,j}}\,\frac{v_{i,j,k-1} - v_{i,j,k}^{n+1} - v_{i,j,k}^{n-1} + v_{i,j,k+1}}{(\Delta\sigma)^2} - Y_{i,j,k}
\end{aligned}
\tag{38}
$$

where, unless otherwise noted, all the superscripts are n and thus are dropped for convenience. The nonlinear inertia terms $X_{i,j,k}$ and $Y_{i,j,k}$ are

$$X_{i,j,k} = \frac{H_{i,j}u^x_{i,j,k}u^x_{i,j,k} - H_{i-1,j}u^x_{i-1,j,k}u^x_{i-1,j,k}}{\Delta x}$$

$$+ \frac{(h_{i,j+1} + E_{i,j+1})u^y_{i,j+1}v^x_{i,j+1} - (h_{i,j} + E_{i,j})u^y_{i,j}v^x_{i,j}}{\Delta y}$$

$$+ U_{i,j}\frac{u_{i,j,k-1}(\Omega_{i,j,k-1} + \Omega_{i-1,j,k-1}) - u_{i,j,k+1}(\Omega_{i,j,k+1} + \Omega_{i-1,j,k+1})}{4\Delta\sigma}$$

$$+ [1-(k-1)\Delta\sigma]\frac{u_{i,j,k-1} - u_{i,j,k+1}}{2\Delta\sigma}\frac{\eta^{n+1}_{i,j} + \eta^{n+1}_{i-1,j} - \eta^{n-1}_{i,j} - \eta^{n-1}_{i-1,j}}{4\Delta t} \qquad (39a)$$

$$Y_{i,j,k} = \frac{H_{i,j}v^y_{i,j,k}v^y_{i,j,k} - H_{i,j-1}v^y_{i,j-1,k}v^y_{i,j-1,k}}{\Delta y}$$

$$+ \frac{(h_{i+1,j} + E_{i+1,j})u^y_{i+1,j,k}v^x_{i+1,j,k} - (h_{i,j} + E_{i,j})u^y_{i+1,j,k}v^x_{i+1,j,k}}{\Delta x}$$

$$+ V_{i,j}\frac{v_{i,j,k-1}(\Omega_{i,j,k-1} + \Omega_{i,j-1,k-1}) - v_{i,j,k+1}(\Omega_{i,j,k+1} + \Omega_{i,j-1,k+1})}{4\Delta\sigma}$$

$$+ [1-(k-1)\Delta\sigma]\frac{v_{i,j,k-1} - v_{i,j,k+1}}{2\Delta\sigma}\frac{\eta^{n+1}_{i,j} + \eta^{n+1}_{i,j-1} - \eta^{n-1}_{i,j} - \eta^{n-1}_{i,j-1}}{4\Delta t} \qquad (39b)$$

Unless otherwise noted, all the superscripts are n and thus dropped, since the inertia terms are calculated at present time level n. In Equations (39a,b), η^{n+1} and Ω are presently obtained variables; since at each time level η and Ω are calculated first by Equations (34) and (35) respectively, u and v are followed by Equations (37) and (38).

When the calculations for velocities are to be performed using the predicative equations, (37) and (38), the variables $u^{n+1}_{i,j,k}$ and $v^{n+1}_{i,j,k}$ which appeared respectively on the right-hand-side of Equations (37) and (38) should be rearranged, so that a form for velocities similar to Equation (34) appears. In this form, all quantities on the right-hand-side are obtained based on specified h, calculated u and v at present and previous time levels, newly computed Ω and η at three time levels. All the variables

and notations that appeared in Equations (37) through (39) have been defined and are shown in Figure 4. However, in Figure 4, the common superscript n and subscript k have been omitted for brevity. Figure 4 also shows clearly the horizontal extent of variables involved in the calculation of η, u and v in the cross-hatched region, namely $\eta_{i,j}$, $u_{i,j,k}$ and $v_{i,j,k}$ (for k = 1 to 4).

Similar to the treatment of the momentum equations, the energy equation, Equation (16), can be written in finite difference form as

$$\frac{H_{i,j}^{n+1}T_{i,j,k}^{n+1} - H_{i,j}^{n-1}T_{i,j,k}^{n-1}}{2\Delta t} =$$

$$B_h H_{i,j}\left[\frac{T_{i+1,j,k}^{n} - 2T_{i,j,k}^{n} + T_{i-1,j,k}^{n}}{(\Delta x)^2} + \frac{T_{i,j+1,k}^{n} - 2T_{i,j,k}^{n} + T_{i,j-1,k}^{n}}{(\Delta y)^2}\right]$$

$$+ \frac{B_v}{H_{i,j}} \frac{T_{i,j,k-1}^{n} - T_{i,j,k}^{n+1} - T_{i,j,k}^{n-1} + T_{i,j,k+1}^{n}}{(\Delta\sigma)^2} - R_{i,j,k} \qquad (40)$$

where the nonlinear term, $R_{i,j,k}$, is given by

$$R_{i,j,k} = \frac{1}{4\Delta x}\left[U_{j+1,j}(u_{i+1,j,k} + u_{i+1,j,k+1})(T_{i+1,j,k} + T_{i,j,k})\right.$$

$$\left. - U_{i,j}(u_{i,j,k} + u_{i,j,k+1})(T_{i,j,k} + T_{i-1,j,k})\right]$$

$$+ \frac{1}{4\Delta y}\left[V_{i,j+1}(v_{i,j+1,k} + v_{i,j+1,k+1})(T_{i,j+1,k} + T_{i,j,k})\right.$$

$$\left. - V_{i,j}(v_{i,j,k} + v_{i,j,k+1})(T_{i,j,k} + T_{i,j-1,k})\right]$$

$$+ \frac{H_{i,j}}{2\Delta\sigma}\left[\Omega_{i,j,k}(T_{i,j,k} + T_{i,j,k-1}) - \Omega_{i,j,k+1}(T_{i,j,k} + T_{i,j,k+1})\right]$$

$$+ \left[1-(k-\tfrac{1}{2})\Delta\sigma\right]\cdot\frac{T_{i,j,k-1} - T_{i,j,k+1}}{2\Delta\sigma}\cdot\frac{\eta_{i,j}^{n+1} - \eta_{i,j}^{n-1}}{2\Delta t} \qquad (41)$$

Likewise, unless indicated, all the superscripts are n and thus dropped

for clearity. Equation (40), similar to Equations (37) and (38), can lead to a predictive equation for $T^{n+1}_{i,j,k}$.

In the model, since the density is considered as a constant, the equation of state, Equations (17), is of no use, and the system is uncoupled. With that, the temperature field can be solved separately provided that all results from the hydrodynamic model are available. That is, the spatial and temporal variation of temperature is solved after the spatial and temporal variation of velocity fields is known. Alternatively, Equation (40) can predict T^{n+1} after obtaining η^{n+1}, Ω, u^{n+1} and v^{n+1} at each time cycle. The former involves two separated programs while the latter is a coupled program only. In coding the model above, both possibilities are taken into account by using flag statements (see Users Manual for Free-Surface Model, 1980).

SOLUTION PROCEDURES

Clearly, Equations (37) and (38) are for u and v at interior points; that is, they are not on the boundaries. Figure 4 implies why these formulae are not for the boundary points. Therefore, Figure 2 indicates that the normal velocity along the boundaries must be either specified or calculated by some other means. For solid lateral boundaries parallel to x- or y-axis, the normal velocities are specified to be zero all the time. At the river mouth and discharge outlet, the normal components are given by the known flowrate and the average water depth. At the seaward boundary, the imposing tide is specified along a parallel line at half-grid size away from the boundary. The difference of water elevations at half-grid points across the open boundary is used to calculate the normal velocity there.

At the bottom, the no-slip condition requires that u = v = 0 at all times; hence, there is no need for doing Equations (37) and (38) at K = 5. At the free surface or k = 1, the wind-produced shear stresses are prescribed as a function of space and time, and can be written as

$$\left(\frac{\partial u}{\partial \sigma}\right)_{\sigma=0} = \frac{\rho U_{i,j}}{A_v}\,\tau_x(x, y, t)$$

$$\left(\frac{\partial v}{\partial \sigma}\right)_{\sigma=0} = \frac{\rho V_{i,j}}{A_v}\,\tau_y(x, y, t)$$

These conditions demand a modification of predictive formula for u^{n+1} and v^{n+1} at k = 1. That is, the DuFort-Frankel format for second derivative, Equation (33), is replaced by (indices i and j are omitted and values of k are indicated)

$$\left(\frac{\partial^2 u}{\partial \sigma^2}\right)^n_{k=1} = \frac{2}{(\Delta\sigma)^2}\left[u_2^n - \tfrac{1}{2}u_1^{n+1} - \tfrac{1}{2}u_1^{n-1} + \frac{\rho U_{i,j}\tau_x \Delta\sigma}{A_v}\right]$$

and a similar one for v-momentum equation. In this scheme, the free-surface wind drag has been incorporated to drive the current through the u^{n+1} and v^{n+1} at the free surface.

The boundary conditions on vertical velocity w are the kinetic condition

$$w = \frac{d\eta}{dt} \qquad \text{at } \sigma = 0$$

and the rigid bottom condition

$$w = 0 \qquad \text{at } \sigma = -1$$

These conditions expressed in terms of modified vertical velocity Ω are

$$\Omega = 0 \qquad \text{at } \sigma = 0 \text{ or } k = 1$$

$$\Omega = 0 \qquad \text{at } \sigma = -1 \text{ or } k = 5$$

As stated earlier, these conditions have been incorporated into the first integral form of the continuity equation; namely, the predictive equation for surface elevation, Equation (13) or Equation (14) with $F_5 = 0$. Consequently, the finite difference formular for Ω, Equation (35), is for k = 2, 3 and 4, while $\Omega_{k=1}$ and $\Omega_{k=5}$ are set to zero at all times.

The boundary conditions of energy equation are adiabatic on solid boundaries and known temperature or zero normal derivative of temperature on open boundaries. It can be seen that if one neglects the lateral thermal diffusion terms, which are small in comparison with convection terms anyway, then no adiabatic condition is needed on the solid lateral wall; this is due to zero normal velocities on the solid lateral wall. However, condition is still needed on the open boundaries. At the bottom, the heat flux is zero; while at the surface, the heat flux is proportional to $(T_s - T_e)$. These conditions are required when Equation (40) is used to calculate T^{n+1} at k = 1 and k = 4 respectively.

As in most other hydrodynamic models for transient problems, the computation routine works step-by-step in time. This means that the computation proceeds through a sequence of time steps, each advancing the entire flow configuration through a small, but finite, increment of time, Δt. The results of the present and the last steps act as a basis for the calculation to proceed to the next one, whereby the initial conditions can develop, within the limitations imposed by the boundary conditions, into the subsequent flow configurations. That is, provided that the values of dependent variables are known initially, the values at subsequent times are obtained by using the explicit scheme. The leap-frog finite difference formulae, Equations (34), (36), (37) and (40), predict surface elevation, η, and two horizontal velocities, u and v, and water temperature, T, at time level n+1. The vertical velocity w does not appear in these equations and thus, is left out until needed for picturing

the flow configuration. Each time cycle itself contains the following recursive processes.

1. The countinuity equation in the form of Equation (34) is used for η^{n+1} through the mass conservation of the fluid column at (i,j). At the same time, the modified vertical velocity Ω^{n+1} is also calculated at k = 2, 3 and 4, since it is also based on the continuity equation but in a different form; namely, Equation (35).

2. The nonlinear inertia terms that appear in the horizontal momentum equations, (37) and (38), are considered as driving terms; that is, they are calculated from formulae (39a,b) by using known results at the present time (n). This calculation usually takes a significant portion of the total computing time; thus, it is advised to drop this calculation whenever justified. For general tidal flows, the inertia effect is negligibly small in comparison with the Coriolis force. Therefore, if the Rossby Number, which is the ratio of inertial force to Coriolis force, is very close to zero, the calculation of X and Y terms can be skipped entirely.

3. The horizontal momentum equations, Equations (37) and (38), are used to calculate u^{n+1} and v^{n+1}. Here, the specified boundary conditions, such as prescribed normal velocities, surface wind stresses and specified tide, come into play.

4. The nonlinear terms, R, in the energy equation, Equation (40), is calculated by formula Equation (41). Unlike the nonlinear terms, X and Y of the momentum equations, R is to be included and calculated under normal circumstances.

5. Temperature at advance step, T^{n+1}, is calculated by Equation (40), and the adiabatic condition, known discharge temperature, given ambient temperature and surface heat transfer rate play a part in determining the temperature field.

STABILITY

The leap-frog (explicit) method has a limit on the size of the time step. Exceeding this limit makes the computation unstable. According to Platzman (1963), the maximum time step for an inviscid linear system, i.e. the system with viscous and nonlinear inertia effects neglected, the maximum allowable time step is

$$\Delta t_{max} = \left[\left(\frac{f}{2}\right)^2 + \frac{2gH_{max}}{(\Delta x)^2} \right]^{\frac{1}{2}}$$

where H_{max} = maximum depth in the problem. If the Coriolis effect is also neglected, then

$$\Delta t_{max} = \frac{\Delta x}{\sqrt{2gH_{max}}}$$

The leap-frog method with the DuFort-Frankel scheme for vertical diffusion terms has been adopted in the present model. As pointed out by Forsythe and Wasow (1960), this format is unconditionally stable for a pure diffusion model, a system in which the viscous diffusion is the only mechanism responsible for transport. Although, the present hydrothermal model is considerably more complex than a pure diffusion model, the use of the DuFort-Frankel format is an important consideration for a shallow water system because the vertical diffusion criterion tends to become relatively more restrictive as the vertical dimension becomes smaller.

SECTION 5

APPLICATIONS TO ANCLOTE ANCHORAGE

INTRODUCTION

The present model has been successfully applied in thermal dispersion studies at the Anclote Anchorage site. The site, located on the west central coast of Florida near the town of Tarpon Springs, is a shallow channel between the mainland and Anclote Key which separates the channel from the Gulf of Mexico, as shown in Figure 1. Anclote Anchorage is of interest since it is the receiving water body for the Anclote Power Plant cooling water discharge. The channel is relatively shallow with depths ranging from 0.3 to 3.6 m. Shallow regions of less than 0.6 meter comprise about 35% of the Anclote Anchorage area, which is approximately 5 km in length and 6 km in average width. The principal driving mechanism for current circulation is tidal flux at the north and south entrances of the channel. The tide is predominantly semidiurnal with a mean range of two feet. Earlier measurements of temperature and salinity indicated the currents flow in and out through both entrances. However, the water exchange appears to be stronger in the south than in the north, or the currents generally flow in the north direction during flood tide and flow in the south direction during ebb tide.

The Anclote Power Plant operated by the Florida Power Corporation has two 515 MW, oil-fired, electrical generating units. Cooling water is drawn from the Anclote River through a man-made channel. The six pumps delivering a total of 1,990,000 gpm (125.6 m^3/sec) are designed to raise the water temperature of 2.8°C above the ambient water temperature. The heated water is discharged back into the Anclote basin through the discharge channel with dredged submarine extension. The designed total flowrate is approximately 53 times the long-term average flowrate of the Anclote River. At present, only Unit 1 is operative, while Unit 2 is awaiting permission. The present flowrate, therefore, is 995,000 gpm (62.7 m^3/sec).

The model as applied to the Anclote Anchorage shows its capacity for considering the effects of geometry and bathymetry, spatio-temporal variation of the free surface, various boundary conditions, including tides of different phase and range, surface heat transfer based on equilibrium temperature concept, and changing meteorological conditions. In addition, turbulence has been considered by using the eddy transport approximations.

CHOICE OF DOMAIN AND GRID SYSTEM

In this study, the Anclote Anchorage is designed to contain the area of water bounded by the Anclote Keys and sand barriers on the west, mainland on the east, and two imaginary E-W lines drawn from the northern tip of the barriers and the south end of Anclote Key to the mainland. These two imaginary boundaries are considered to be so far that the thermal plume will not reach them even at low tidal stage. Its location and schematization are shown in Figure 7. This water is open to tides from the Gulf of Mexico at both ends. The Anclote River, where the intake of cooling water is located, is also included since the recirculation of discharge flow is of concern to the power company.

The adopted horizontal grid layout and its index are also shown in Figure 7. The grid work is allowed to orient away from north-south, east-west system, but in general, the y-axis of the grid system aligns with south-north. Thus, the subscript i increases eastwardly while j increases northwardly. The z-axis is chosen upward from mean water surface while the subscript k increases downward from the water surface.

The selection of the grid size is governed by several constraints. If the grid size is too large, the approximation of the channel in the system will be inaccurate, and at certain size, the computation will become meaningless. However, decreasing the grid size will lead to a considerable increase in the computer time since the computations must then be made on more points. In addition, the time step will decrease because the dispersive properties of the computational method are related to the ratio of the time step to the spatial grid size. After some numerical experiments, the model on a 16 x 14 x 5 grid with grid size $\Delta x = \Delta y = 416.75$ m and $\Delta \sigma = 0.25$ is considered a good compromise between the resolution desired for the region near the discharge and the limitation of the computer (UNIVAC 1108) at the University of Miami. Also, care has been taken to have the intake and outlet at grid points. The velocities at these grid points are specified such that the flowrate and direction can be easily represented.

SUMMARY OF DATA

Field measurements of current velocities and water temperature have been made for model calibration as well as verification purposes for the hydrothermal prediction. Two field trips were carried out in the summer and winter respectively. The procedures and data results will be discussed briefly below.

June 1978 Data Acquisition

On June 19 and 20, a team was sent out to the field for measurement of current velocity and temperature. In coordination, the infrared (IR) scanner data was obtained by flights over the channel. The current measurement and temperature readings were obtained at 9 points; 4

points were located at the north end, four others at the south end, and one in the middle of the channel, as shown in Figure 8. At each point, the measurements were done at different depths, namely the water surface and some depths below the water surface.

The in-situ measurements were carried out by personnel on three boats. The Barnes PRT-5 Radiometer was used to measure the surface temperature, and a thermister (#9) with floating mechanism was used to measure the temperature of the water surface. Temperature profiles are measured by lowering another thermister (#4) into the water in increments of 2 to 3 feet. Current velocities are measured with a Bendix Model No. 665 w/readout current meter which reads the magnitude and direction of the current. Figures 9 through 12 show the current velocities at 4 tidal stages, which give a picture of the current patterns in the channel, expecially at the boundaries. One may notice that the current is stronger at the south boundary than at the north boundary. Both boundaries can exchange water with the Gulf of Mexico.

The flights were made at 609.6 meter or 2000 feet altitude. The black body of IR scanning window was set at different ranges for each flight set. For the first flight, the black body range was 74° to 98°F, the second was 75° to 99°F, the third was 78° to 102°F and the fourth was 80° to 104°F. All have a full black body range of 24°F; it provides a satisfactory resolution of 4°F for each of the six colors between white and black. A finer resolution was also obtained which reduced the color band to 0.74°C (1.33°F) temperature spread. At 2000 feet altitude, the scanning width is 941.8 meters or 3090 feet. With this scanning width, the whole stretch of the channel was covered by ten east-west flights as labeled in Figure 13.

The in-situ measurement of water surface temperature at the time when the airborne IR data was undertaken provides a calibration of IR temperature. Figures 14-17 show the measured temperature at their points at four tidal stages of this mission. Since the channel is quite shallow and only the surface temperature is of primary concern in this study, only the surface temperature is presented.

January 1979 Data Acquisition

Field measurements by boat and by IR scanning were schedualed on January 30 and 31. On previous experience, the current measurement and temperature reading were carried at different points from the previous mission. Figure 18 shows the location of all points where the data were collected by three boats. The route for boat #1 was along points 4, 3, 2, 1 and 5, and for boat #2, the route was along points 8, 7, 6, 10, and 9. Meanwhile, boat #3 was working on the region near the coast between outlet and intake. The water temperature and current velocity were measured by the same instruments used in the previous data acquisition. The measurements were taken at the surface and successive depths of 3 ft (1 m) intervals. The flights were coordinated at the same

time as for IR scanning, while the boats were collecting the data. These ten flight lines, shown in Figure 13, were made at 609.6 meters or 2000 feet altitude. The black body of IR scanning range was set at 44-80°F so each of the six color bands between white and black would represent a 6°F interval.

On January 30, the weather permitted both morning and afternoon data collection. However, on January 31, the conditions was so bad that the mission had to be postponed to February 1 afternoon. Figures 19 through 21 show the current velocities at three tidal stages; namely, flood tide, ebb tide and high tide respectively. Figures 22 through 24 show the surface temperature distribution at corresponding stages. To further show the measured temperature fields, isotherms were interpolated from these in-situ data and presented in Figure 25 through 27 corresponding to each tidal stage respectively.

In these two data acquisitions, although a plan of synchronized measurements of current at tide changes was carried out in order to provide current data at slack, flood and ebb, the effort was not so successful due to technical difficulties in obtaining reading and other unexpected circumstances. Therefore, the current data could only be of use as reference.

CALCULATION OF INPUTS

The important input parameters and some specification of boundary conditions, such as intake and discharge velocities, discharge temperature, tidal condition, river flow, surface heat transfer, and wind stress, will be presented in this section.

1. Time step, DT

   In order to determine the time step, DT, the stability criterion has to be followed:

$$DT < \frac{Dx}{\sqrt{2gH_{max}}} = \frac{41760}{\sqrt{2 \times 980 \times 360}} = 50 \text{ sec}$$

   About 1/3 of this value is reasonably safe to use.

   Here, we use DT = 15 sec.

2. Vertical eddy viscosity, A_v

   The vertical eddy viscosity is estimated by means of the formula

$$A_v = CH^{4/3}$$

   where H is the local depth and C is an empirical constant. This type of formula for horizontal turbulent diffusion was originally

suggested by Richardson (1926). Since that time, the 4/3 power has been substantiated by a considerable amount of empirical evidence and theoretical analysis. The so-called constant C may vary with the intensity of the turbulence and is not well established. In this study, H is used as maximum depth and C is 0.002, so that we have

$$A_v = .002x(360)^{4/3} = 6 \text{ cm}^2/\text{sec}$$

For shallow, well-mixed tidal water, about three times the calculated value was found suitable. Here, we use $A_v = 20 \text{ cm}^2/\text{sec}$.

3. Horizontal eddy diffusivity, B_h

The horizontal eddy diffusivity is calculated by the same formula as mentioned above. However, the maximum depth is replaced by the maximum length of the domain, which is 6 km in this study. So we have

$$B_h = .002x(600,000)^{4/3} = 100,000 \text{ cm}^2/\text{sec}$$

4. Vertical eddy diffusivity, B_v

In this study, the turbulent Prandtl Number is assumed as 1. Thus, the vertical eddy diffusivity is equal to the vertical eddy viscosity or $B_v = A_v = 20 \text{ cm}^2/\text{sec}$.

5. Surface heat transfer coefficient, K_s

The procedures for K_s calculation are as follows:

a. $T_d = T_a - (14.55 + 0.114T_a)(1-f) - [(2.5 + 0.007T_a)(1-f)]^3$

where T_d = dewpoint temperature, °F

T_a = air temperature, °F

f = relative humidity in fraction of unit

b. $\beta = 0.255 - 0.0085T_{ave} + 0.000204T_{ave}^2$

where $T_{ave} = (T_s + T_d)/2$, and β is an intermediate step

T_s = ambient surface temperature, °F

c. $f(u) = 70 + 0.7u^2$

where u = wind speed, mph

d. $K_s = 15.7 + (\beta + 0.26)f(u)$

where K_s is the surface heat transfer coefficient in BTU/ft² day.

The values of T_a, f, u, T_s needed for this calculation are read from the climatological data.

6. Wind drag coefficient, C_d

The wind stresses on the free surface are introduced into the model as

$$\frac{A_v}{\rho H}\frac{\partial u}{\partial \sigma}\Big|_{\sigma=0} = \tau_x \qquad \frac{A_v}{\rho H}\frac{\partial v}{\partial \sigma}\Big|_{\sigma=0} = \tau_y$$

The subscripts x and y indicate the shear stress acting in the x and y direction respectively. The relation of these stresses to the wind speed at a certain height is very difficult to determine theoretically and its value is usually based on semi-empirical formulae. The well known form of the relationship between shear stress τ and wind speed U (usually measured at a height of ten meters) is

$$\tau = \rho_a C_d U^2$$

where ρ_a is the air density and C_d is a dimensionless drag coefficient. In this study, the drag coefficient formulae obtained by Wu (1969) is adopted, and its value was given by

$$C_d = 0.00125\ U^2 \quad \text{for} \quad U < 1 \text{ m/sec}$$

$$= 0.0005\sqrt{U} \quad \text{for} \quad 1 \leq U < 15 \text{ m/sec}$$

$$= 0.0026 \quad \text{for} \quad U \geq 15 \text{ m/sec}$$

7. Intake and discharge velocities

The intake and discharge velocities are calculated according to the discharge flowrate from power plant data, the grid size and the average depth at the intake and discharge outlet. The procedures are shown as follows:

a. Flowrate = 955,000 gpm (from power plant physical data)
= 62.8 m^3/sec
= 62.8 x 10^6 cm^3/sec

b. Both intake and discharge channels are at 45° from N, therefore,

31.4 x 10^6 cm^3/sec is crossing the Δx and Δy at the point of intake and discharge.

c. The average depth at intake and discharge outlet is approximately 4' or 122 cm, and the width is $\Delta x = \Delta y$ = 41760 cm; so the cross-sectional area is 41760 x 122 cm^2.

d. The average velocities:

$$U_{ave} = V_{ave} = \frac{31.4 \times 10^6}{41760 \times 122} = 6.163 \text{ cm/sec}$$

e. The velocity profiles are assumed as shown.

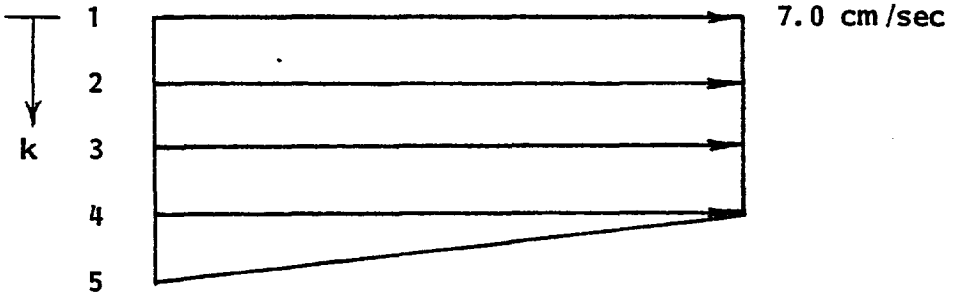

f. To allow for channel storage during tide change we assume the intake and discharge velocities to be sinusoidal, i.e.

Intake: $V3(14, 4, k) = 7 - 3 \times \cos[\frac{2\pi}{12.5} (EST - 7.625)]$

$U3(15, 3, k) = V3(14, 4, k)$ for $k = 1, 2, 3, 4$

Discharge: $V3(14, 8, k) = 7 - 3 \times \cos[\frac{2\pi}{12.5} (EST - 7.5)]$

$U3(15, 8, k) = -V3(14, 8, k)$ for $k = 1, 2, 3, 4$

where 7.625 and 7.5 are taken to be the values of the phase shift which takes into account the time to travel from the south end of Anclote Key to the concerned point.

8. Tidal condition on June 19, 1978

Simulated diurnal tide is shown in Figure 28, where

a. Period = 12.5 hr

b. Stage = short term average sea level - MSL = 48 cm

c. Amplitude = ½ short term average tide range = 65 cm

d. Time shift = 7.125 hr
i.e. at 7.125 am, June 19, 1978, the tide at the south end of Anclote Key was zero.

e. W - E lapse = 0.014 hr/DX

Wave propagation speed $C = \sqrt{2gh} = \sqrt{2 \times 980 \times 360} = 850$ cm/sec
(H = 360 cm is the maximum depth of the Anchorage.)

The time needed to travel one grid distance is

$$\frac{DX}{C} = \frac{41760}{850} = 50 \text{ sec} = 0.014 \text{ hr}$$

We use 0.014 hr per DX for phase shift in W - E direction and the imposing tide at the south entrance is

$$\eta_s = 48 + 65 \sin[\frac{2\pi}{12.5} (EST - 7.125 - 0.014(I - 1)]$$

I = grid no. in W - E direction.

f. S - N lapse = 0.15 hr

Distance from south entrance to north entrance is about 543000 cm. Time for wave to travel this distance is $\frac{543000}{850} = 0.18$ hr. We take 0.15 hr as phase difference between the south and the north boundaries; there, the imposing tide at the north entrance is

$$\eta_n = 48 + 65 \sin[\frac{2\pi}{12.5} (EST - 7.125 - 0.15 - 0.014(I - 1)]$$

9. Tidal condition on January 30, 1979

Simulated diurnal tide is shown in Figure 29. The calculation procedures are of the same as summer tidal conditions.

a. Period = 12.0 hr

b. Stage = 36.6 cm

c. Amplitude = ½ short-term average tide range = 42.7 cm

d. Time shift = 10 hr
i.e. at 10 am, January 30, 1979, the tide at the south end of Anclote Key was zero.

e. W - E lapse = 0.015 hr/DX

This value is slightly higher than the summer case since the maximum water depth in the winter is less than the maximum water depth in the summer. The imposing tide at the south entrance is

$$\eta_s = 36.6 + 42.7 \sin[\frac{2\pi}{12} (EST - 10 - 0.015(I - 1)]$$

f. S - N lapse = 0.2 hr/DX

This is the time for wave to travel from south entrance to north entrance. So the imposing tide at the north entrance is

$$\eta_n = 36.6 + 42.7 \sin[\frac{2\pi}{12} (EST - 10 - 0.2 - 0.015(I - 1)]$$

10. Anclote River flowrate and temperature

a. The distance traveled from South Anclote Key to Tarpon Springs is 20 DX. We estimate a time lapse of 0.5 hr to account for the retardation due to buffering effect of river storage and Anclote River's natural outflow.

b. The average current is estimated to be 20 cm/sec, therefore, we take

$$U3(16, 1, k) = 20 \cos[\frac{2\pi}{12.5} (EST - 7.625)]$$

$$V3(15, 1, k) = -20 \cos[\frac{2\pi}{12.5} (EST - 7.625)]$$

for k = 1, 2, 3, 4

c. The surface elevation at Tarpon Springs is to be calculated.

d. To be in accordance with given velocities at Tarpon Springs, the temperature there is also assigned and its value has a 24 hr period instead of 12.5 hr. This temperature on June 19, 1978 is

$$T3(15, 1, k) = 26.9 + 0.5 \sin[\frac{2\pi}{24} (EST - 12)]$$

while on January 30, 1979 the temperature was assumed as

$$T3(15, 1, k) = 11.9 + 0.5 \sin[\frac{2\pi}{24} (EST - 12)]$$

where the 12 hr shift is to make the peak temperature occur at 1800. Thus, the water in and out at Tarpon Springs has a temperature ranging from 26.4 (before dawn) to 27.4 (late afternoon) in the summer and ranging from 11.4 (before dawn) to 12.4 (late afternoon) in the winter.

11. Discharge temperature

On June 19-20, 1978, the recorded discharge temperature at daytime was in the range of 29.3 - 30.3°C, while on January 30-February 1, 1979, the temperature range was 16.4 - 15.2°C. To account for the further drop of discharge temperature due to cooler ambient temperature at nighttime, we assumed a sinusoidal variation of discharge temperature with diurnal period.

a. Discharge temperature is estimated for June 1978

$$T3(14, 8, k) = 29.4 + 0.4 \sin[\frac{2\pi}{24} (EST - 12)]$$

Therefore, the highest discharge temperature of 30.3°C happens at 6 pm and the lowest 29.3°C at 6 am.

b. Discharge temperature is estimated for January 1979

$$T3(14,\ 8,\ k) = 15.8 + 0.6 \sin[\frac{2\pi}{24}\ (EST - 12)]$$

The highest discharge temperature is 16.4°C at 6 pm and the lowest discharge temperature is 15.2°C at 6 am.

12. The Gulf temperature

The Gulf water outside the Anclote Anchorage as well as the atmosphere is sink to the heat disposal from the power plant; therefore, the boundary conditions on temperature at the north and south entrance are not considered as adiabatic as in normal case of far-field thermal pollution problem. Instead, we specify the outside-Anchorage ambient temperatures. Again, they are 24 hr periodic and their values should be in accordance with the measured temperature in the same neighborhood. Here in compliance with measured data, we use

$$T_{ab} = 27.0 + 0.2 \sin[\frac{2\pi}{24}\ (EST - 12)]$$

for the summer simulation during June 19-20 1978 and use

$$T_{ab} = 11.8 + 0.4 \sin[\frac{2\pi}{24}\ (EST - 12)]$$

for the winter simulation during January 30-February 1, 1979.

RESULTS

Due to the fact that the archival data for Anclote site is inadequate, the following inputs are used for the computer runs: data from NOAA tide table, solar radiation, wind and the power plant operating conditions. Tables 1 and 2 show the operating conditions of Anclote Power Plant during June 19-20, 1978 and January 30-February 1, 1979 respectively. The isotherms obtained from the IR data from each flight are interpolated by hand from mosaic digicolor films and then plotted by the computer. These isotherm plots are presented in this section for easy comparison with the predicted isotherms. The average deviation of the calculated temperatures from IR temperatures is also indicated. This deviation is calculated by simply averaging the temperature differences between the measured and calculated temperatures at each point of the domain. The average deviation is given by

$$\delta^2 = \sum_{i,j} [TB(i,\ j,\ 1) - TIR(i,\ j)]^2 / \sum_{i,j} (i,\ j)$$

where TB is the calculated temperature, TIR is the IR temperature and $\sum_{i,j}(i,\ j)$ is the number of surface half-grid points in the domain.

The TIR and TB isotherms are then compared to assess the accuracy of the model in predicting the dispersion of the waste heat. It is recog-

nized that the principal factors affecting the flow pattern and the shape of the thermal plume are the tide driving through the north and south boundaries, wind effects on the water surface, bottom topography, heat transfer through the air-water interface, and the intensity of eddy viscosity and diffusivity. The effects of each of these factors on the flow pattern have been discussed in detail by Lee et al. (1978a, b). These effects are important in understanding the numerical behavior of the model, and play a leading role in proving the capabilities of the model. In this report, however, only the results of the verification runs are presented. The results of the summer and winter verifications are discussed in the next two sections.

Summer Results

The figures from the summer simulation show the hydrothermal dispersion of waste heat under the conditions of June 19-20, 1978, as described in the previous section. The simulation run started at 0400 EST, June 18, with initial conditions of zero velocity field, equilibrium water level and constant ambient temperature (so-called "cool start"). The tide and heated discharge are then imposed. After 20 hours of "warm up," the thermal plume can be seen to develop. Experience indicates that the initial condition is not important, as its effects die out in the first one or two hours. However, it is convenient to begin a simulation through a "cool start."

Figure 30 shows the surface flow pattern at 1030 EST, June 20, which corresponds to the high tide at south Anclote Key. The current velocity is relatively small and the mainstream flows in the north direction. A recirculation can be seen to occur as a result of the flow of water from the Anchorage into the Anclote River. The net effect is the flow of part of the discharge into the river entrance where the intake structure is located.

Figure 31 shows the resultant velocity at high tide. The result of the velocity components, u and w, is plotted on the vertical cross sections at J = 4, 8 and 12. It is believed that the currents at these sections are most affected by the plan-form configuration, bathymetry and other features such as the river mouth, discharge and tidal boundary etc. The u-w velocity profiles show clearly the effects of bottom friction in retarding the flow. Figure 32 shows the v-w resultant velocity on the vertical cross sections at I = 4, 8 and 12. In these two figures, the vertical velocity component w has been exaggerated to make the vertical circulation of the current detectible. One may notice that, since the velocity vector at the top level ($\sigma = 0$) is plotted right on the water surface, joining the tails of these velocity vectors would show the free-surface profile.

Figure 33 shows the isotherms plotted from the IR data. The computer-plotted points were obtained through visual interpolation from the mosaic IR image, as discussed earlier. Due to the difficulties of visual

interpolations and large grid size, the computer-plotted isotherms unavoidably differ somehow from the real isotherms in the digicolor film. This figure shows that the heated water is recirculated back to the intake through the Anclote River. This will cause an increase in the input temperature of the condenser cooling water, thus reducing the efficiency of the power plant.

Figure 32 shows the computed isotherms at the same tidal stage. Comparing this figure with Figure 33, the good agreement of these temperature fields can be easily seen. The average deviation of the simulated temperature from IR temperature is only 0.359°C.

Figures 30 through 34 form the first set of results of the summer simulation. This set of plotted results, which includes the surface velocity, u-w velocity, v-w velocity, IR temperature and the calculated temperature, coincides with the high tide at south Anclote Keys. Figures 35 through 39 is the second set of results of the same simulation run, at 1430 EST, June 20, or at a time corresponding to maximum ebb tide at south Anclote Keys. Therefore, this set shows the current and temperature fields of the Anchorage four hours after the first set of results was taken. It is also seen that the Anclote River empties into the Anclote basin while the basin drains northward and southward. There are strong ebb flows occurring at both the north and south end of the Anclote Keys barriers. The dividing line lies along the j = 10 grid line. On the northern side of this line, the water flows north, while on the southern side, it flows south. At this ridge line, the water has minimal transverse motion. The location of this line varies with time as the tides from both ends are not in phase. In reality, most of the flow in the Anclote Anchorage comes primarily from the south end; therefore, the ridge line is observed to exist at a region close to the northern end of the Anchorage. Also, this line is observed to move southward during ebb tide and northward during flood tide. The flow pattern corresponds with the observed flowfield at a similar tidal stage.

Figure 36 shows a strong u-velocity component at the river mouth, while Figure 37 shows a strong v-velocity component near the south boundary. Figures 38 and 39 are two corresponding isotherm plots at this tidal stage. It can be seen that the thermal plume moves according to the stage of the tidal cycles, as would be expected. The 27.50°C isotherm from the simulated results covers a larger area than that of the IR plot. Generally speaking, the simulated results are in good agreement with the IR data.

Figures 40 through 45 is the third set of results of the simulation run, but at 1730 EST, June 20, which corresponds to low tide at the south Anclote Keys. The current field is seen to be generally quite small except at Anclote River region. The river is still undergoing its outflowing process and continues to empty its tidal storage into the basin, while the open sea flows into the Anchorage through both open boundaries. It has to be mentioned here that the lower part of the 27.50°C isotherm from the IR data is not very visible in the IR digicolor film. As a result,

the contour shown in Figure 43 is estimated by extrapolation from the IR data. The calculated isotherm at this temperature, as shown in Figure 44, has a peculiar shape at the same region. This may be due to the fact that this region, north of the dredged ship channel leading to Tarpon Springs, is relatively shallow and becomes especially so during low tidal stage. The sum effect is that the heat transport, due to convection, becomes small. This shallow region can be easily seen from Figure 42 along the I = 8 cross section at a location about J = 4, 5 and 6. If this isotherm is ignored, then the remaining isotherms, shown in Figures 43 and 44, have the same sort of tongue-shape profiles, showing some degrees of good agreement.

Figures 45 through 49 is the last set of results of the summer simulation. The time is 2030 EST at the same day and corresponds to flood tide at the south end of the Anchorage. The incoming tide from the south end drives northward into Anclote basin. The dividing line discussed earlier, does not appear, as the northbound tidal current changes course into the northeast direction. Both Figures 48 and 49 show that the thermal plume has been pushed back, and the isotherms become more compact. These features could be explained by considering that the changing tide retards the convective transport of the thermal plume. The 27.50 and 28.25°C isotherms in Figure 49 are seen to be pushed toward the northeast direction rather than being pushed toward the east coast, as shown by the corresponding IR isotherms, Figure 48. This could be because the north and south tidal conditions are no longer consistent with the real tidal conditions after such a long time of simulation (64.5 hours). At this stage, it seems that the northern tide could induce a stronger current to push the plume toward the southeast direction. If correct tidal data had been provided, the results might have improved.

Winter Results

The winter simulation run started at 2200 EST, January 29, 1979. The meteorological data and input conditions are as discussed in the previous section. Here, we present only two sets of results corresponding to the successive flood tidal and maximum ebb tidal stages at the Anchorage on January 30, 1979. These tidal stages were recorded during the first and second data acquisition missions which took place on January 30, 1979, at about 1100 EST and 1600 EST respectively. It should be pointed out that, due to sudden change in weather condition, the second and third missions were about 48 hours apart. In between these missions, the sea had become very rough under very stormy conditions. The effect of the stormy weather can be clearly seen by comparing the two IR temperature fields, Figures 58 and 60; the former was taken at about 1600 EST, January 30, while the latter was taken at about 1600 EST, Feburary 1. There is therefore a 48 hour time lag. Figure 58 shows the thermal plume at ebb tide of a typical winter day. This is a great contrast to Figure 60 which shows the plume during high tide but after the influence of the stormy weather. It is to be noted that the isotherms shown in Figure 60 are not of the same values as those shown in Figure 58. In fact, there was a 4°C drop in temperature, and a 2.3°C drop in

the discharged water temperature. Particularly, the wind condition had gone through a very substantial change during this 48 hour time gap. This wind speed, shown in Figure 60, was still 50% stronger than that shown in Figure 58. Therefore, it was no surprise to find that the thermal plume, shown in Figure 60, was so compact and shrunken. The windy condition and the relatively low ambient temperature were the apparent causes of this much dwarfed plume. Observing the compactness of the neighboring isotherms and judging the resolution power of the present grid system, one is tempted to suspect the ability of modeling under this kind of extremely severe meteorological condition. Experience shows that it is difficult to obtain such a compact thermal plume through simulations of such adverse natural conditions. Considering the roughness of the grid system, this is actually not a surprise. Therefore, for the winter simulation only two sets of results, namely, 1100 EST and 1600 EST on January 30, are presented.

Figures 50 through 54 is the first set of results of 1100 EST, January 30, 1979, which corresponds to the flood tidal stage at south Anclote Key. Figure 50 shows the surface-flow pattern from calculated results. The incoming tide from the south entrance drives directly into the Anclote River. There is a dividing line across the Anchorage at this tidal stage. This ridge line is located along the J = 9 grid line, at which the incoming tides from both north and south meet. This can also be seen from the in-situ measurement, as shown in Figure 19. The discharge at the outlet is pushed head-on by this flow. As a result, the thermal plume is squeezed by this flow. The isotherm plots in Figures 53 and 54 show this effect very clearly. Although Figures 53 and 54 show similar tendencies, the calculated isotherms seem not to be in good agreement with the IR isotherms; particularly so for the 15.40°C isotherms. However, the calculated plume areas are close to those obtained from the IR data. Both temperature fields show the dispersion of the thermal plume along the shore. The recirculation of heated water is clearly indicated in both figures, showing that a recirculation actually occurs at this tidal stage under the meteorological influence.

Figures 55 through 59 show the second set of results of the winter simulation runs. This set of plotted results shows the current and temperature fields at 1600 EST, January 30, 1979, during ebb tidal conditions at the Anchorage. Figure 55 shows a strong current driving from northeast to southwest along the channel. No ridge line is observable, and the discharged water is not entrained by this main current; in fact, most of the discharged water flows directly through the river mouth into the intake of the power plant. Thus, serious recirculation happens at this time; this is also shown in Figure 58 of the IR isotherms and in Figure 59 of the calculated isotherms. The calculated current pattern shown in Figure 55 is in good agreement with that of the in-situ measurements shown in Figure 20. A similar agreement can be seen between the calculated thermal plume shown in Figure 59 with that of the IR data shown in Figure 58. It can also be seen that all the calculated isotherms cover a slightly larger area than the corresponding IR isotherms; this difference is shown to be insignificant by a low deviation of 0.65°C above the IR measured temperature.

REFERENCES

Carter, C. V. The Hydrothermal Characteristics of Shallow Lakes. Ph.D. Dissertation, University of Miami, Florida, 1977.

Dunn, W. E., Policastro, A. J. and R. A. Paddock. Surface Thermal Plumes: Evaluation of Mathematical Models for the Near and Complete Field. Part One and Two, Energy and Environmental Systems Division, Great Lakes Project, Argonne National Laboratory, May 1975.

Forsythe, G. E. and W. R. Wasow. Finite-Difference Method for Partial Differential Equations. J. Wiley and Sons, 1960.

Freeman, N. G., Hale, A. M. and M. B. Danard. A Modified Sigma Equations Approach to the Numerical Modeling of Great Lakes Hydrodynamics. J. Geophysical Research, 77(6), 1050-1060, 1972.

Hinewood, J. B. and I. G. Wallis. Classification of Models of Tidal Waters. J. Hyd. Div., ASCE, Vol. 101, No. HY10, 1975.

Leendertse, J. J. Aspects of a Computational Model for Long-Period Water-Wave Propagation. RM-5924-Pr, The Rand Corp., 1967.

Leendertse, J. J., Alexander, R. C. and S. K. Liu. A Three-Dimensional Model for Estuaries and Coastal Seas: Volume I, Principles of Computation. R-1417-OWRR, The Rand Corp., December 1973.

Leendertse, J. J. and S. K. Liu. Modeling of Three-Dimensional Flows in Estuaries. Proc. 2nd Annual Symposium of the Waterways, Harbors and Coastal Engineering Division of ASCE, September 1975 or Symposium on Modeling Techniques - 75.

Lee, S. S. and S. Sengupta. Three-Dimensional Thermal Pollution Models. NASA CR-154624, 1978(a).
Volume I - Review of Mathematical Formulations
Volume II - Rigid-Lid Models
Volume III - Free-Surface Models

Lee, S. S. and S. Sengupta. Demonstration of Three-Dimensional Thermal Pollution Models at Anclote Rivers, Florida, and Lake Keowee, South Carolina. NASA Project, Mid-Term Report, Department of Mechanical Engineering, University of Miami, Florida, December 1978(b).

REFERENCES

Lee, S. S., Sengupta, S., Tuann, S. Y., and C. R. Lee. User's Manual for Three-Dimensional Free-Surface Model, NAS10-9410. Final Report, August 1980.

Patridge, P. W. and C. A. Brebbia. Quadratic Finite Elements in Shallow Water Problems. Proc. ASCE, Vol. 102, No. HY9, September, 1976.

Phillips, N. A. A Coordinate System Having Some Special Advantages for Numerical Forecasting. J. Meteorology. 14:184-185, 1957.

Platzman, G. W. A Numerical Computation of the Surge of 26 June 1954 on Lake Michigan. Geophysics. 6:407-438, 1958.

Platzman, G. W. The Dynamic Prediction of Wind Tides on Lake Erie. American Meteoroligical Society, Vol. 4, No. 26, September 1963.

Reid, R. O. and B. R. Bodine. Numerical Model for Storm Surges in Galveston Bay. Proc. ASCE, Vol. 94, No. WW1, February 1968.

Richardson, L. F. Atmospheric Diffusion Shown on A Distance-Neighbor Graph. Proc. Roy. Soc., 110:709, 1926.

Sengupta, S. and W. J. Lick. A Numerical Model for Wind-Driven Circulation and Temperature Fields in Lakes and Ponds. FTAS/TR-74-98, Case Western Reserve University, 1974(a).

Sengupta, S., Veziroglu, T. N., Lee, S. S. and N. L. Weinberg. The Application of Remote Sensing to Detecting Thermal Pollution. NAS 10-8470, Mid-Term Report, May 1975.

Sengupta, S. A Three-Dimensional Model for Closed Basins. ASME Paper 76-WA-HT 21, 1976.

Sengupta, S., Lee, S. S. and H. P. Miller. Three-Dimensional Numerical Investigations of Tide and Wind-Induced Transport Processes in Biscayne Bay. SEA Grant Technical Bulletin No. 39, University of Miami, 1978.

Sundermann, J. A Three-Dimensional Model of a Homogeneous Estuary. Proc. 14th Coastal Engineering Conference, Vol. III, June 1974.

Waldrop, W. and R. C. Farmer. Three-Dimensional Flow and Sediment Transport at River Mouths. Coastal Studies Institute, Louisiana State University, Baton Rouge, Technical Report No. 150, September 1973.

REFERENCES

Waldrop, W. and R. C. Farmer. Three-Dimensional Computation of Buoyant Plumes. J. Geophysical Research, Vol. 79, No. 9, 1974(a).

Waldrop, W. and R. C. Farmer. Thermal Plumes for Industrial Cooling Water. Proceedings of the 1974 Heat Transfer and Fluid Mechanical Institute, Davis, L. R. and R. E. Wilson (ed.), Stanford, California, Stanford University Press, June 1974(b).

Wang, J. D. Real-Time Flow in Unstratified Shallow Water. Proc. ASCE, Vol. 104, No. WW1, February 1978.

Wu, J. Wind Stress and Surface Roughness at Air-Sea Interface. J. Geophysical Research. 74(2):444-455, 1969.

TABLE 1 CLIMATIC DATA FOR SUMMER RUN AT ANCLOTE ANCHORAGE

Date	EST	(1) T_{air}(°C)	(2) Humidity	(3) Wind Speed	(4) Wind Direction	(5) Solar Radiation	(6) T_{surf}
6/18	04	23.3	.90	357.6	50.	0.0	26.4
	05	23.3	.90	268.2	50.	0.0	26.4
	06	23.3	.90	312.9	50.	0.0	26.5
	07	23.3	.90	312.9	50.	0.05	26.5
	08	25.0	.84	312.9	50.	0.40	26.7
	09	26.7	.77	447.0	70.	0.75	26.8
	10	28.3	.70	536.4	80.	1.05	26.9
	11	30.0	.65	536.4	80.	1.40	27.0
	12	31.1	.60	536.4	70.	1.60	27.0
	13	32.2	.56	536.4	90.	1.70	27.1
	14	31.6	.57	491.7	80.	1.60	27.1
	15	31.1	.58	536.4	80.	1.50	27.2
	16	30.6	.59	581.1	90.	1.30	27.2
	17	30.0	.61	581.1	80.	1.10	27.2
	18	29.4	.64	625.8	80.	0.70	27.1
	19	28.8	.67	581.1	80.	0.30	27.0
	20	28.3	.70	447.0	80.	0.05	26.9
	21	27.2	.73	402.3	80.	0.0	26.9
	22	26.1	.77	312.9	80.	0.0	26.8
	23	25.0	.75	402.3	80.	0.0	26.8
	24	23.9	.74	312.9	80.	0.0	26.8
6/19	01	22.2	.73	223.5	80.	0.0	26.8
	02	21.7	.76	223.5	60.	0.0	26.8
	03	21.1	.80	312.9	40.	0.0	26.8

TABLE 1 (Continued)

Date	EST	(1) T_{air} (°C)	(2) Humidity	(3) Wind Speed	(4) Wind Direction	(5) Solar Radiation	(6) T_{surf}
6/19	04	21.1	.84	312.9	50.	0.0	26.8
	05	21.7	.82	312.9	50.	0.0	26.9
	06	22.2	.80	312.9	70.	0.0	26.9
	07	22.8	.79	312.9	70.	0.10	27.0
	08	23.9	.73	357.6	70.	0.25	27.0
	09	25.0	.67	402.3	80.	0.40	27.0
	10	26.7	.60	447.0	80.	0.60	27.0
	11	27.8	.56	491.7	90.	1.25	27.0
	12	29.4	.53	536.4	80.	1.25	27.0
	13	30.6	.50	447.0	80.	0.60	27.0
	14	30.0	.53	312.9	90.	0.80	26.9
	15	29.4	.57	268.2	80.	1.20	26.9
	16	28.8	.61	447.0	350.	0.70	26.9
	17	28.3	.65	536.4	350.	0.50	26.9
	18	27.2	.69	581.1	360.	0.15	26.9
	19	26.1	.74	581.1	350.	0.15	26.8
	20	25.6	.76	357.6	60.	0.05	26.8
	21	25.0	.78	402.3	120.	0.0	26.7
	22	25.0	.79	357.6	110.	0.0	26.7
	23	25.0	.79	312.9	110.	0.0	26.6
	24	24.4	.79	357.6	110.	0.0	26.5

TABLE 1 (Continued)

Date	EST	(1) T_{air} (°C)	(2) Humidity	(3) Wind Speed	(4) Wind Direction	(5) Solar Radiation	(6) T_{surf}
6/20	01	24.4	.79	312.9	100.	0.0	26.4
	02	23.9	.80	268.2	100.	0.0	26.5
	03	24.4	.81	357.6	110.	0.0	26.6
	04	25.0	.82	357.6	110.	0.0	26.6
	05	25.0	.82	402.3	110.	0.0	26.7
	06	25.0	.82	357.6	110.	0.0	26.7
	07	25.0	.82	357.6	90.	0.05	26.7
	08	26.1	.78	357.6	90.	0.20	26.8
	09	27.2	.74	491.7	110.	0.60	26.8
	10	28.8	.70	581.1	110.	0.30	27.0
	11	28.9	.66	447.0	110.	0.40	27.0
	12	28.4	.62	268.2	110.	0.40	27.0
	13	30.0	.59	357.6	90.	0.60	27.0
	14	30.6	.58	402.3	90.	0.50	27.1
	15	30.6	.57	402.3	110.	0.55	27.0
	16	30.0	.57	268.2	100.	0.40	27.1
	17	30.0	.56	402.3	100.	0.30	27.2
	18	29.4	.55	312.9	110.	0.20	27.1
	19	28.8	.53	223.5	90.	0.15	27.0
	20	28.0	.50	223.5	90.	0.05	27.0

TABLE 2 CLIMATIC DATA FOR WINTER RUN AT ANCLOTE ANCHORAGE

Date	EST	(1) T_{air} (°C)	(2) Humidity	(3) Wind Speed	(4) Wind Direction	(5) Solar Radiation	(6) T_{surf}
1/29	22	8.8	.98	350	320	0.0	11.8
	23	8.8	.93	350	320	0.0	11.8
	24	8.8	.89	350	320	0.0	11.8
1/30	1	8.3	.86	350	330	0.0	11.7
	2	7.7	.87	350	340	0.0	11.7
	3	7.2	.88	325	350	0.0	11.7
	4	6.7	.89	300	360	0.0	11.7
	5	6.1	.89	280	10	0.0	11.7
	6	5.5	.89	270	20	0.0	11.7
	7	5.0	.89	250	40	0.0	11.7
	8	6.7	.75	280	60	0.05	11.7
	9	8.3	.63	310	80	0.25	11.8
	10	10.0	.54	350	100	0.45	11.9
	11	11.6	.50	375	140	0.75	12.0
	12	13.8	.47	400	180	0.95	12.1
	13	15.5	.43	400	220	1.15	12.2
	14	17.2	.39	400	220	1.30	12.4
	15	18.3	.35	375	220	1.15	12.2
	16	19.4	.31	350	210	1.00	12.1
	17	18.8	.38	310	200	0.80	12.1
	18	18.3	.45	280	170	0.40	12.0
	19	17.2	.52	250	140	0.10	12.0
	20	16.1	.59	230	190	0.0	11.9

TABLE 2 (Continued)

Date	EST	(1) $T_{air}(^{o}C)$	(2) Humidity	(3) Wind Speed	(4) Wind Direction	(5) Solar Radiation	(6) T_{surf}
	21	15.5	.66	210	250	0.0	11.9
	22	15.0	.72	200	310	0.0	11.8
	23	15.0	.70	210	340	0.0	11.8
	24	15.0	.68	230	10	0.0	11.8
1/31	1	14.4	.66	250	40	0.0	11.7
	2	14.4	.66	250	50	0.0	11.7
	3	13.8	.65	270	60	0.0	11.7
	4	13.3	.65	290	70	0.0	11.7
	5	12.7	.77	320	90	0.0	11.7
	6	12.2	.89	360	110	0.0	11.7
	7	11.6	1.00	400	140	0.0	11.8
1/31	8	12.7	.97	420	180	0.05	11.8
	9	14.4	.95	500	220	0.15	11.8
	10	16.1	.93	600	250	0.25	11.9
	11	17.2	.86	700	280	0.35	12.0
	12	16.6	.79	800	310	0.45	12.1
	13	16.1	.72	800	330	0.55	12.2
	14	15.0	.74	850	330	0.50	12.1
	15	13.8	.76	900	330	0.50	11.9
	16	12.7	.77	900	330	0.40	11.7
	17	11.6	.77	700	330	0.30	11.5
	18	10.5	.77	600	330	0.15	11.3
	19	9.4	.77	600	330	0.05	11.0

TABLE 2 (Continued)

Date	EST	(1) T_{air}(°C)	(2) Humidity	(3) Wind Speed	(4) Wind Direction	(5) Solar Radiation	(6) T_{surf}
	20	8.8	.79	600	330	0.0	10.7
	21	8.3	.81	600	330	0.0	10.4
	22	8.3	.83	550	340	0.0	10.0
	23	7.7	.80	500	340	0.0	10.0
	24	7.7	.77	500	340	0.0	10.0
2/1	1	7.2	.74	500	340	0.0	10.0
	2	6.7	.74	550	340	0.0	10.0
	3	6.1	.73	550	350	0.0	9.9
	4	5.5	.73	550	350	0.0	9.9
	5	4.4	.73	500	350	0.0	9.8
	6	3.8	.73	500	360	0.0	9.8
	7	3.3	.73	500	360	0.0	9.7
	8	3.8	.68	550	360	0.05	9.8
	9	5.0	.58	600	360	0.15	9.9
	10	6.1	.51	650	360	0.25	10.0
	11	7.2	.45	650	350	0.40	10.1
	12	8.3	.39	650	350	0.55	10.2
	13	9.4	.33	600	350	0.70	10.2
	14	10.0	.30	600	340	0.85	10.1
	15	10.5	.32	600	340	0.80	10.1
	16	11.1	.34	600	330	0.70	10.0
	17	10.0	.40	600	330	0.55	10.0
	18	8.3	.46	600	330	0.40	10.0

Figure 1. Anclote Anchorage location in the state of Florida

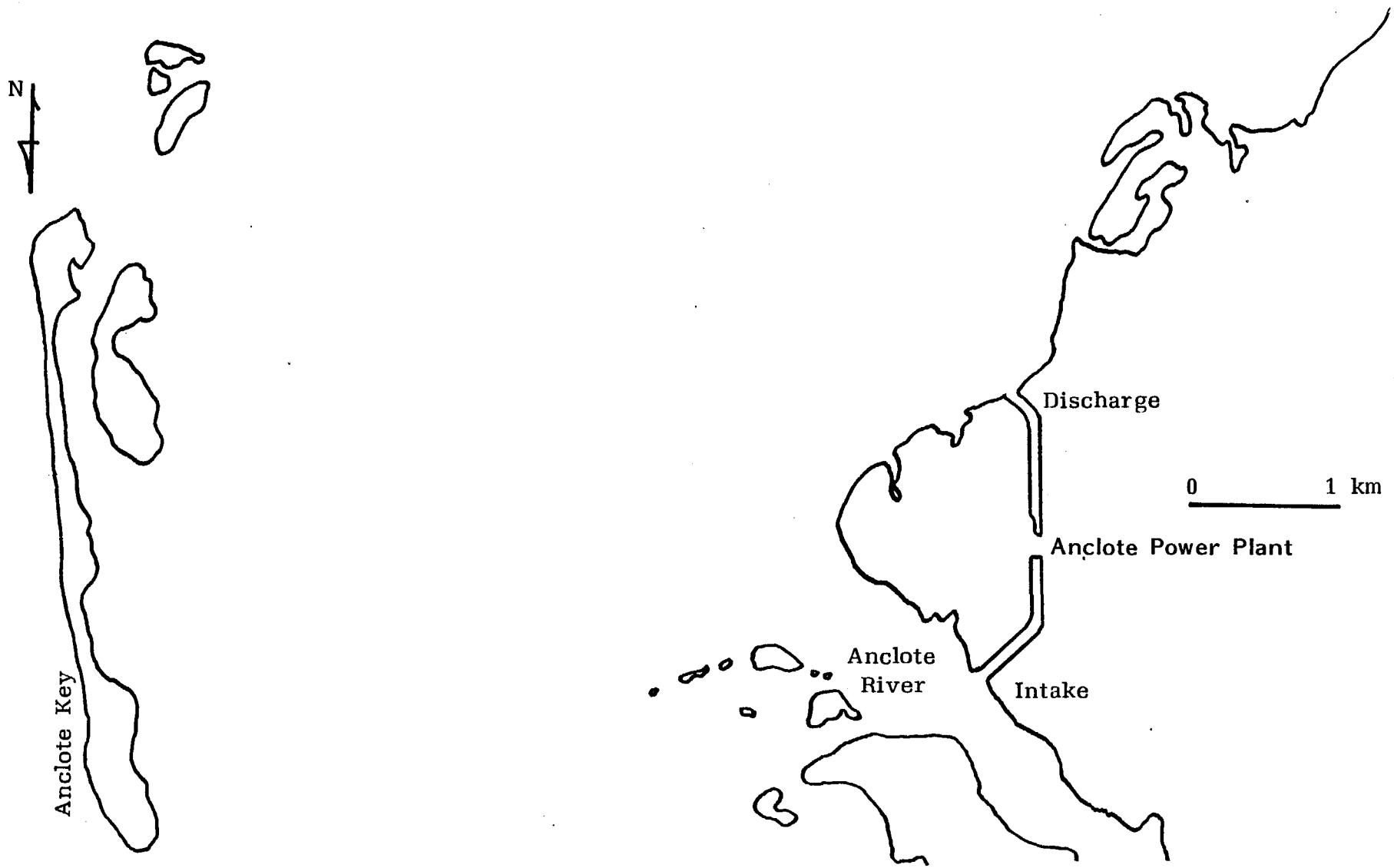

Figure 2. Map of Anclote Anchorage

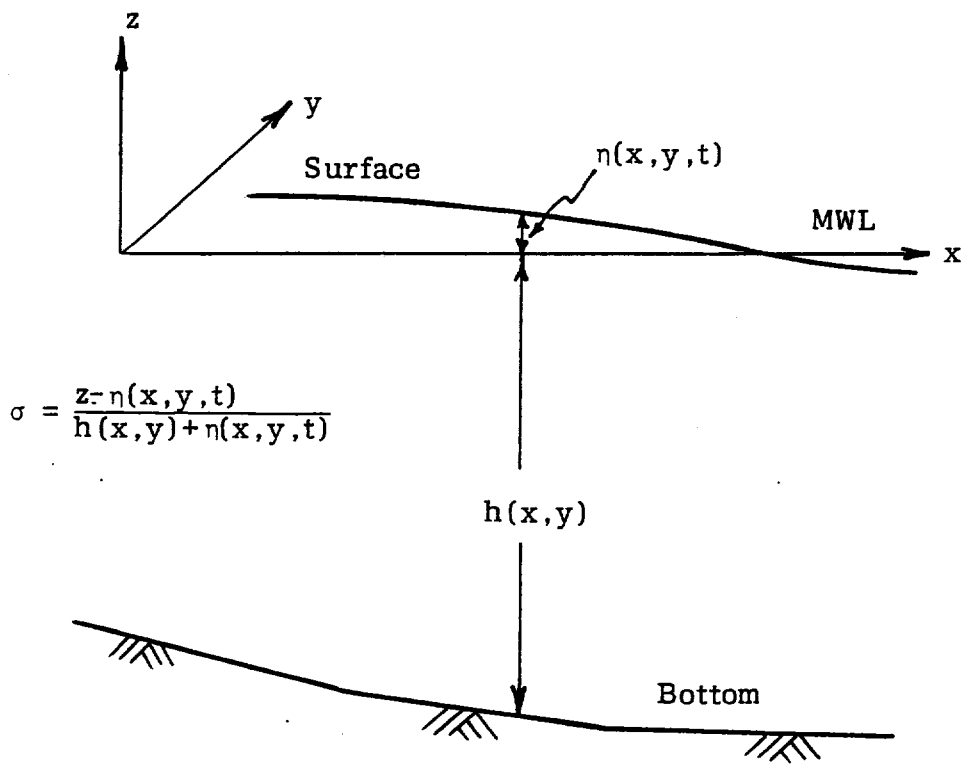

Figure 3. Definition sketch of σ-coordinate

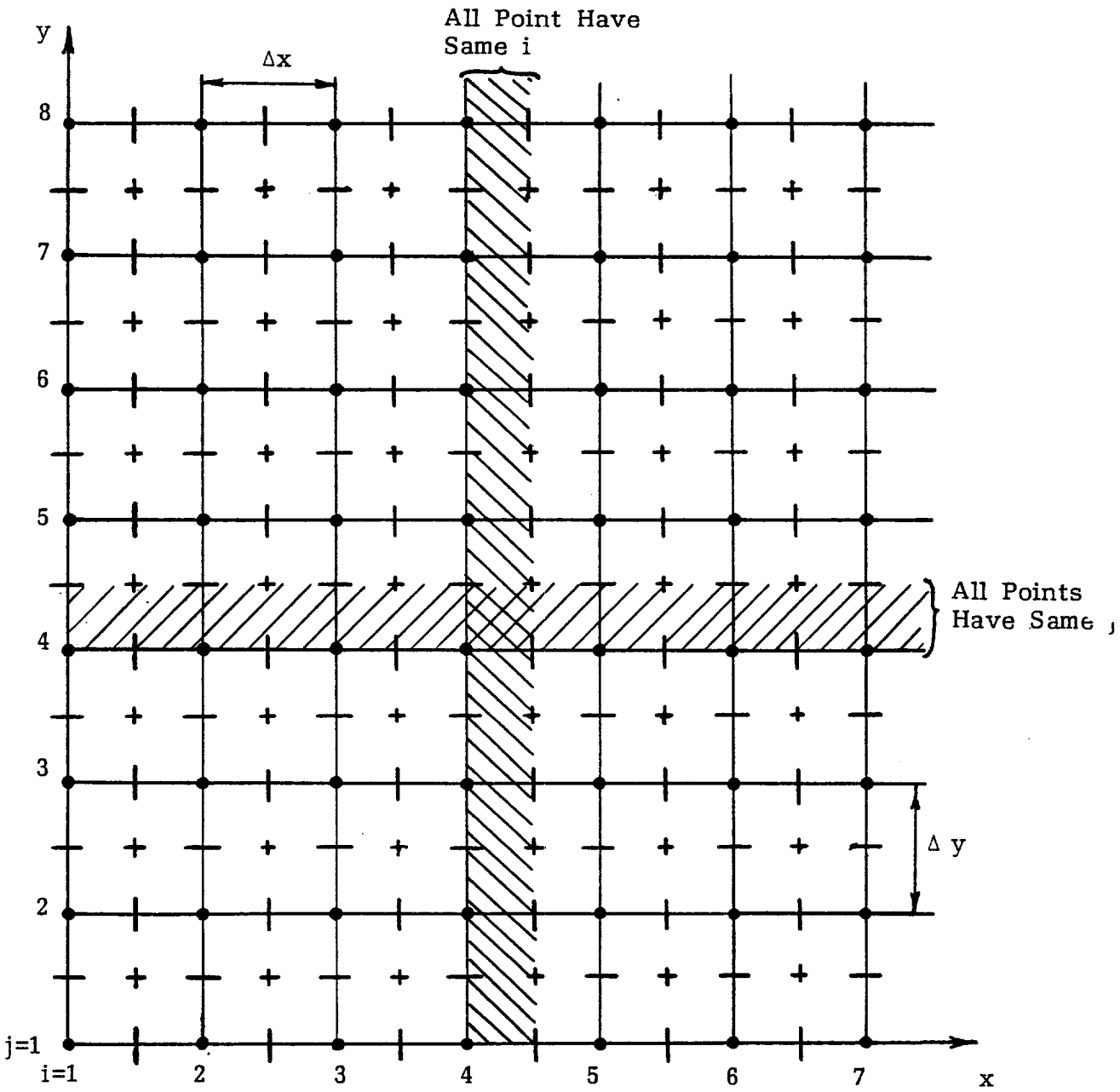

Figure 4. Grid arrangement in the horizontal projection
• (full-grid) depth (h) point; — u velocity point;
| v velocity point; + (half-grid) w, Ω, p, T, ρ and η point

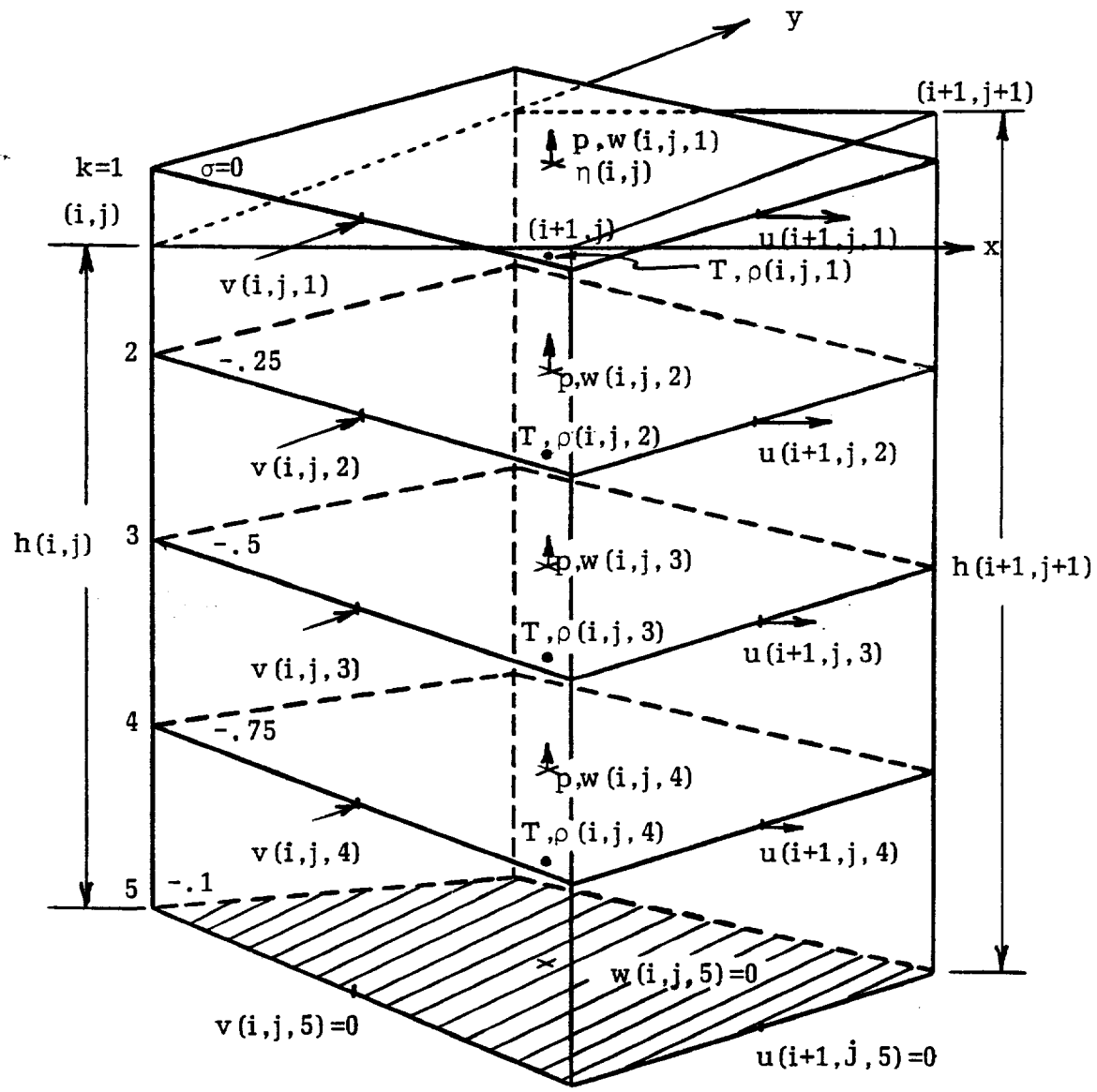

Figure 5. Four cells in a vertical column with velocities shown at definition point, and scalar variables at the center of cell (•)

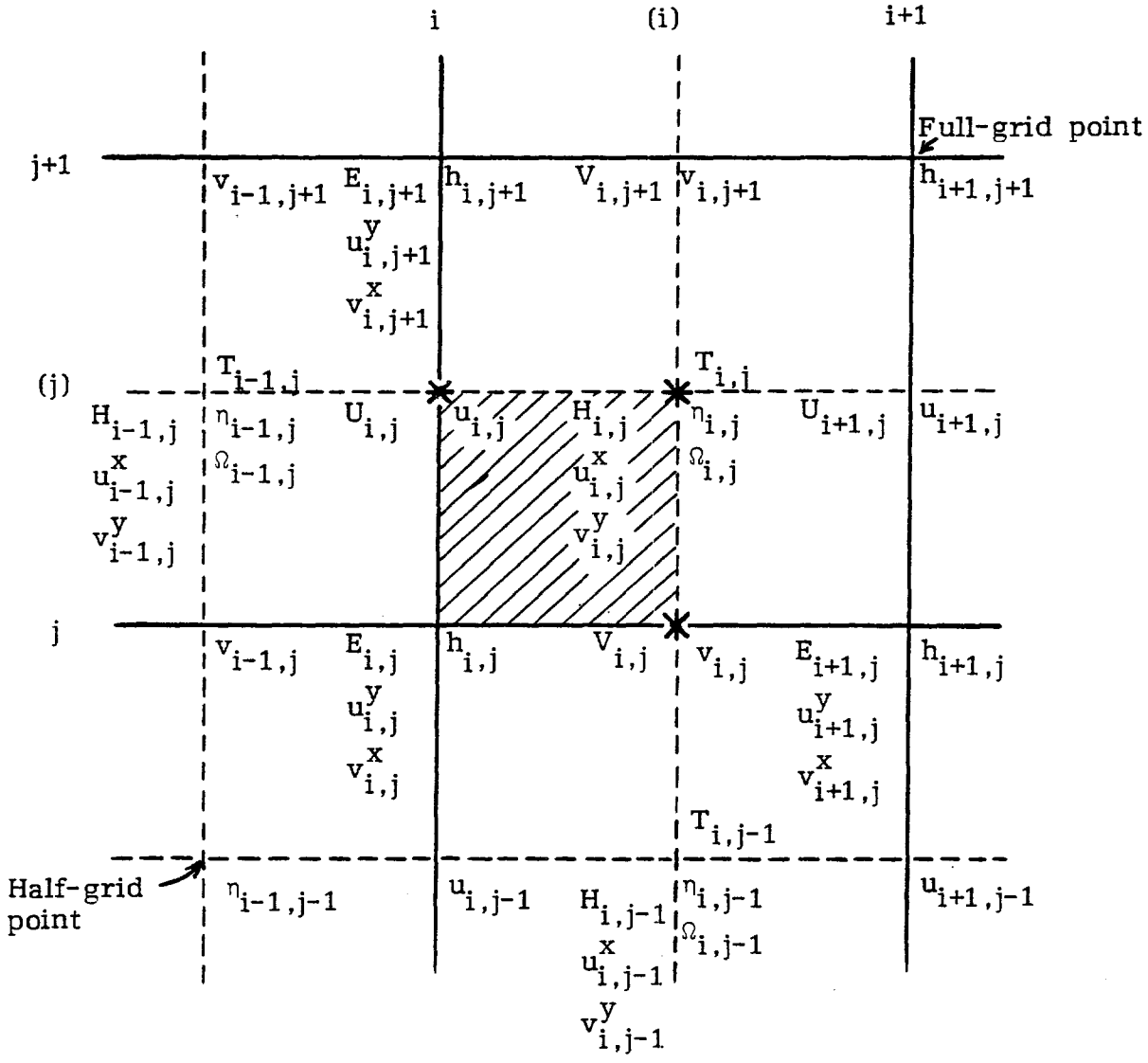

Figure 6. Notations (left) and variables (right) used in calculation of T (✱), η (✱), u (✱) and v (✱) within (i,j)-block (cross-hatched)

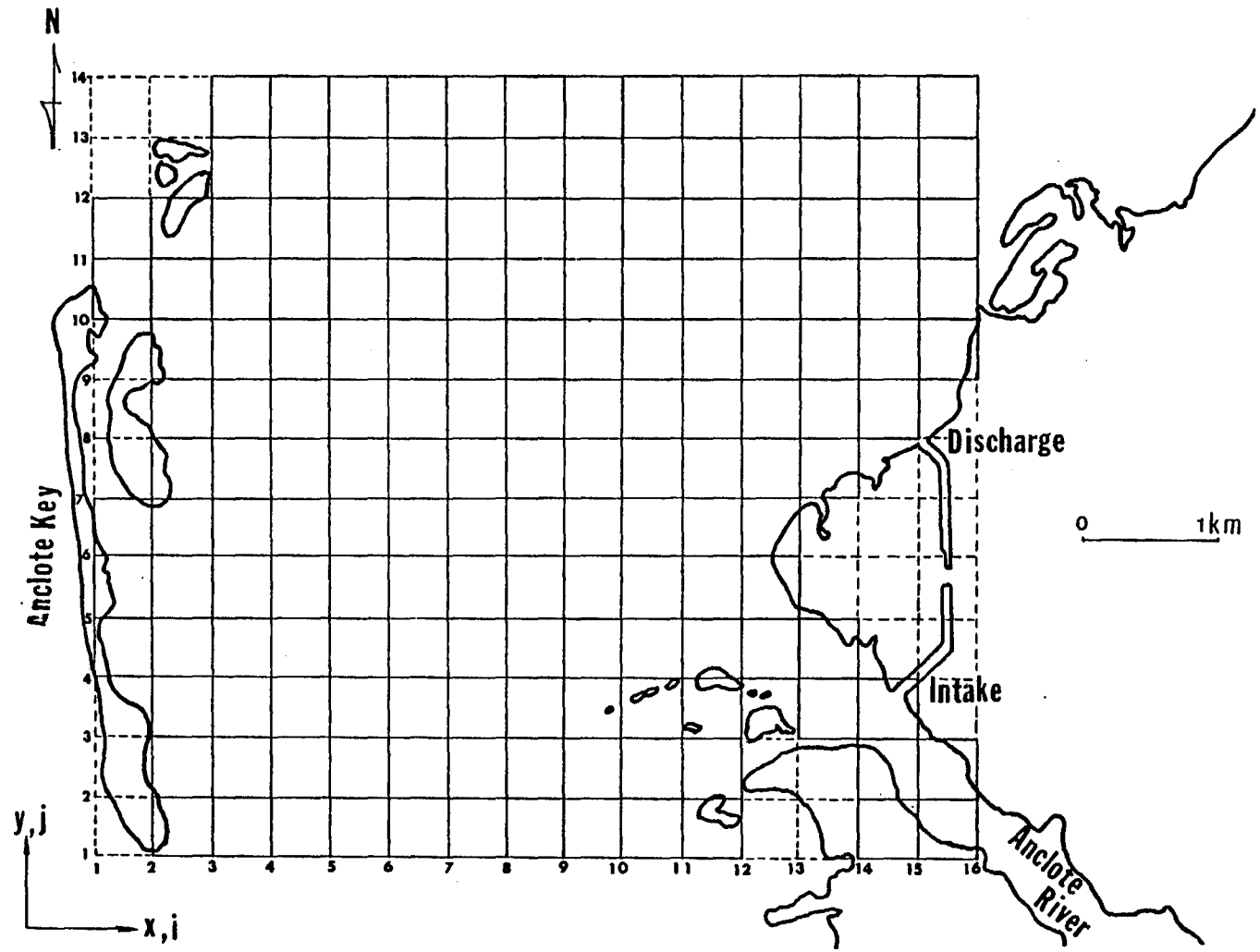

Figure 7. Grid work for the Anclote Anchorage

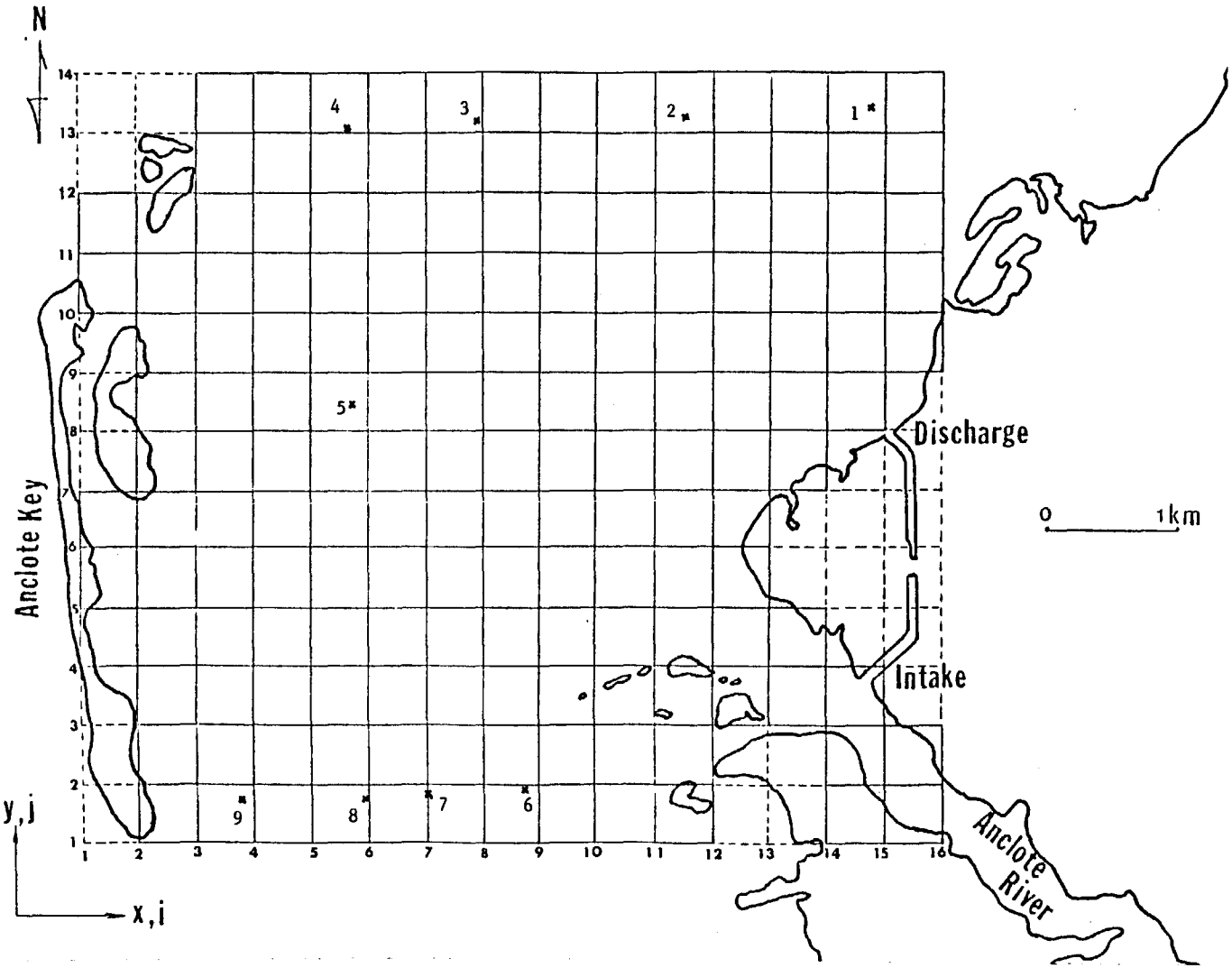

Figure 8. Location of stations for in-situ measurement, June 1978

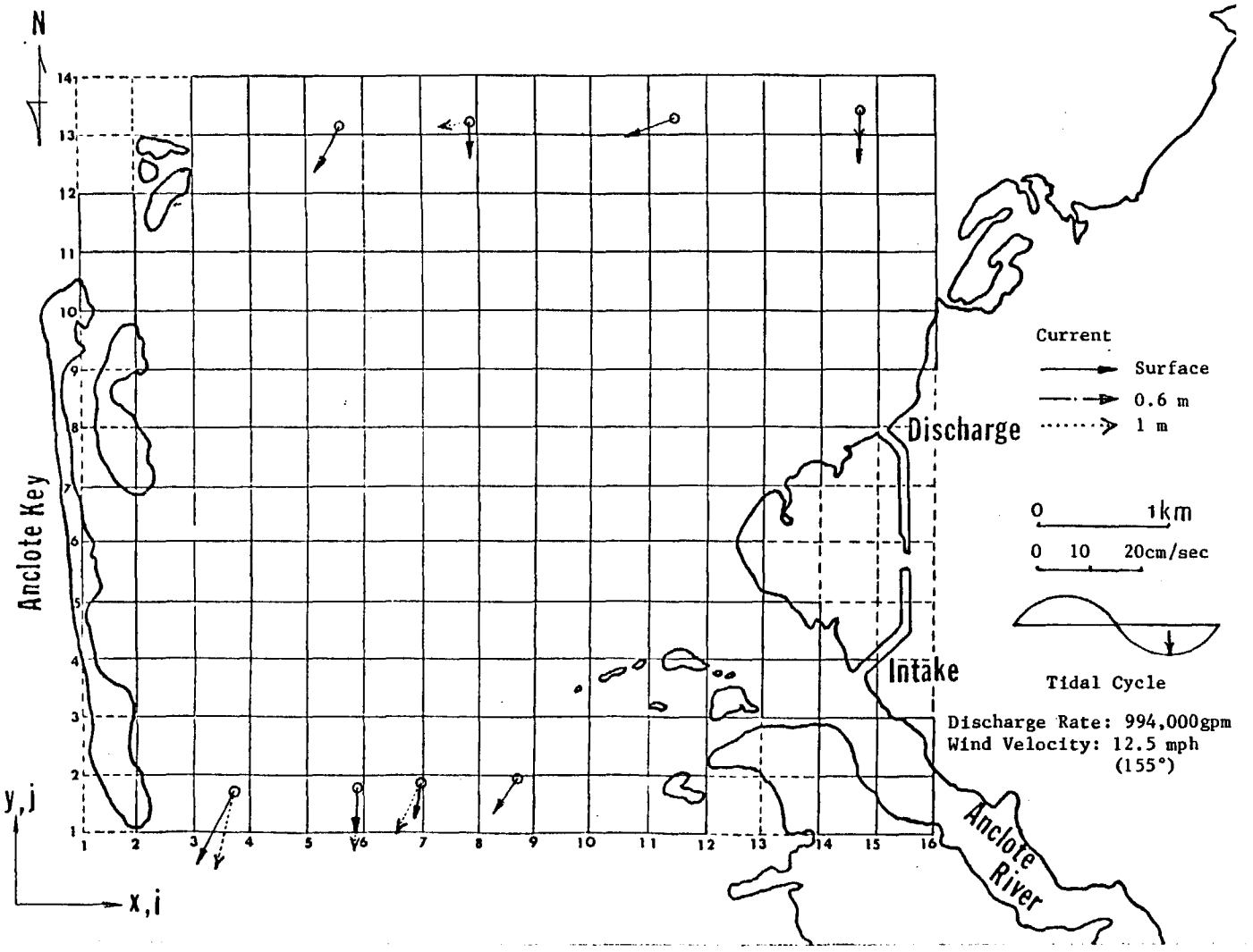

Figure 9. Velocity from in-situ measurement at 1710-1903, June 19, 1978

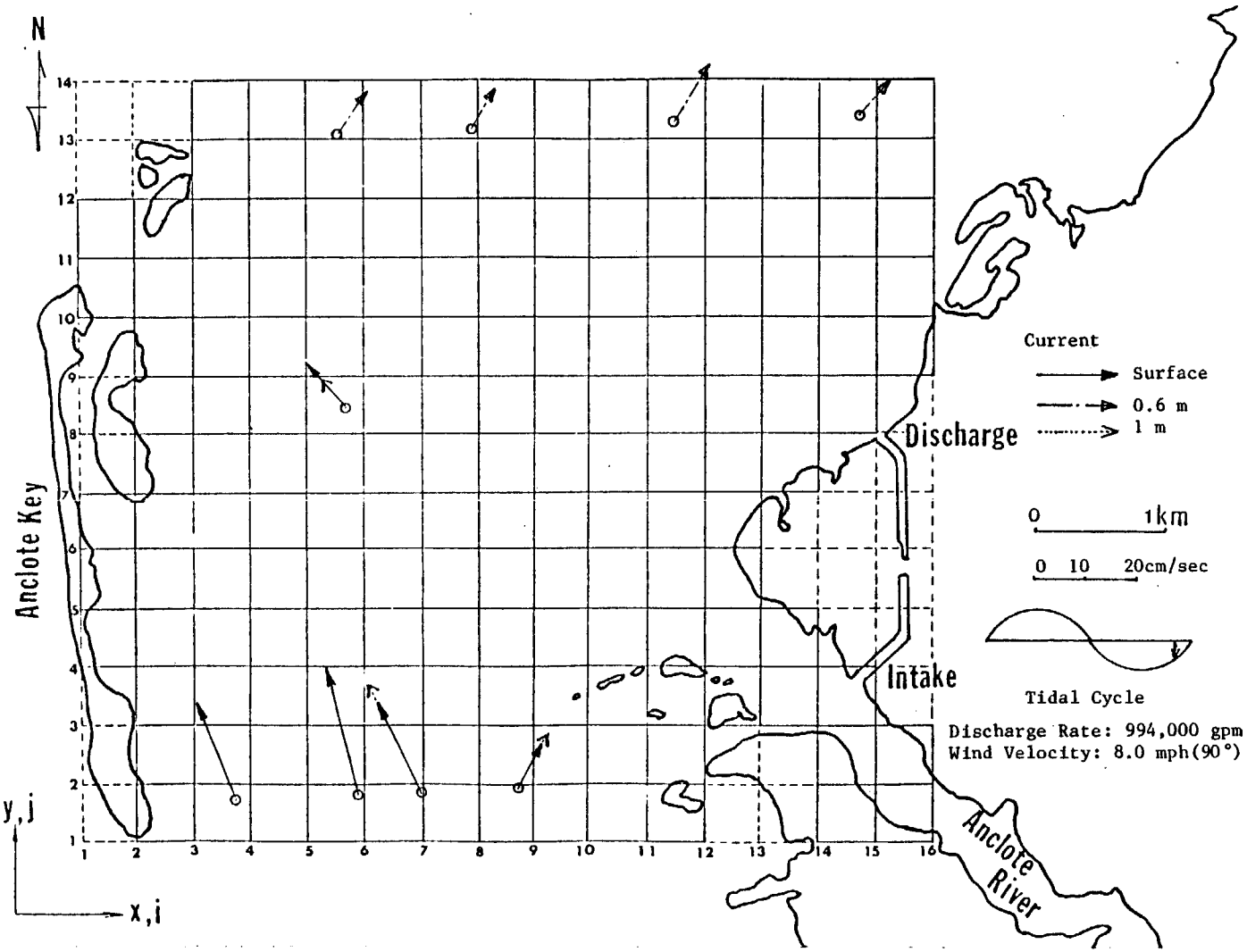

Figure 10. Velocity from in-situ measurement at 0648-0812, June 20, 1978

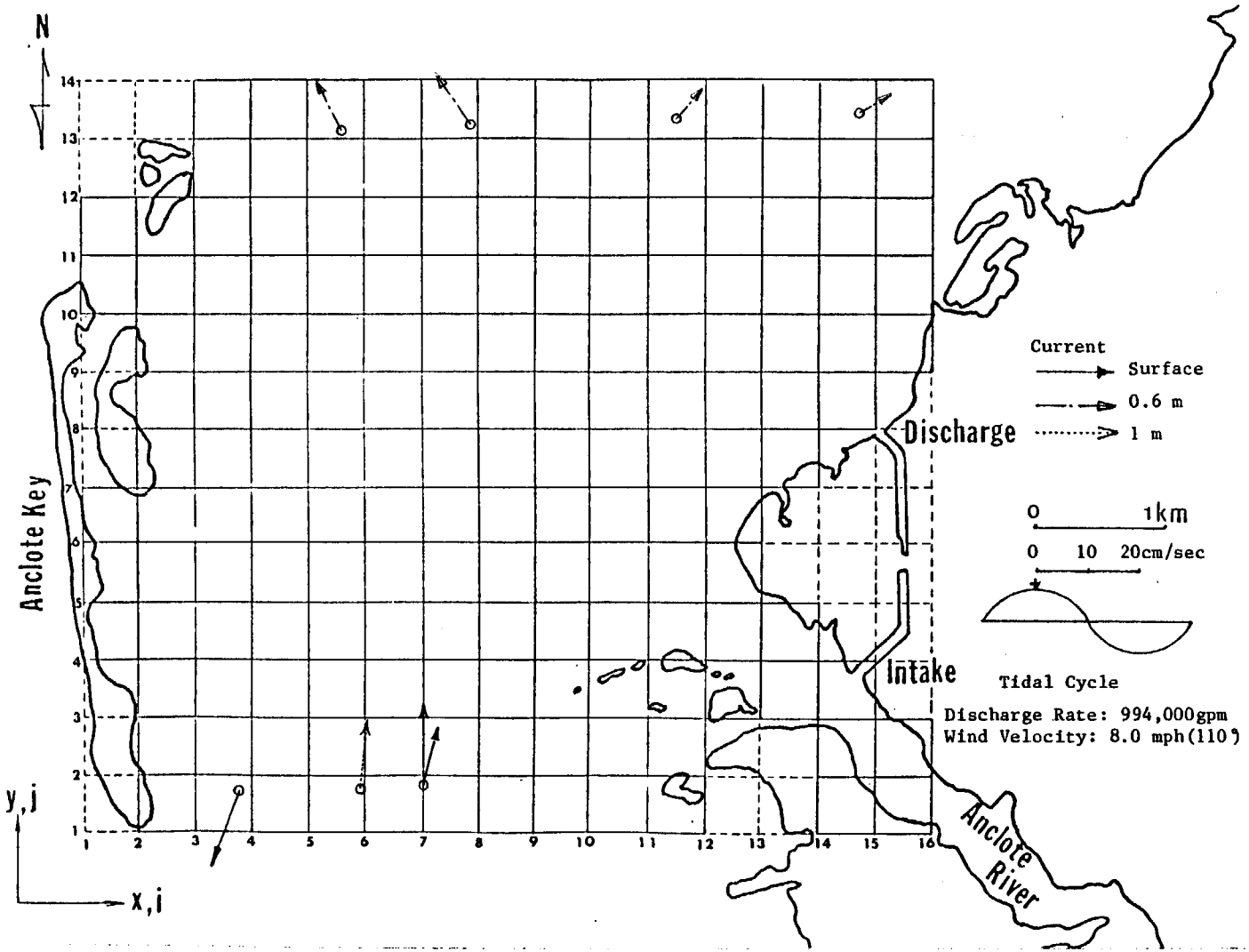

Figure 11. Velocity from in-situ measurement at 1125-1245, June 20, 1978

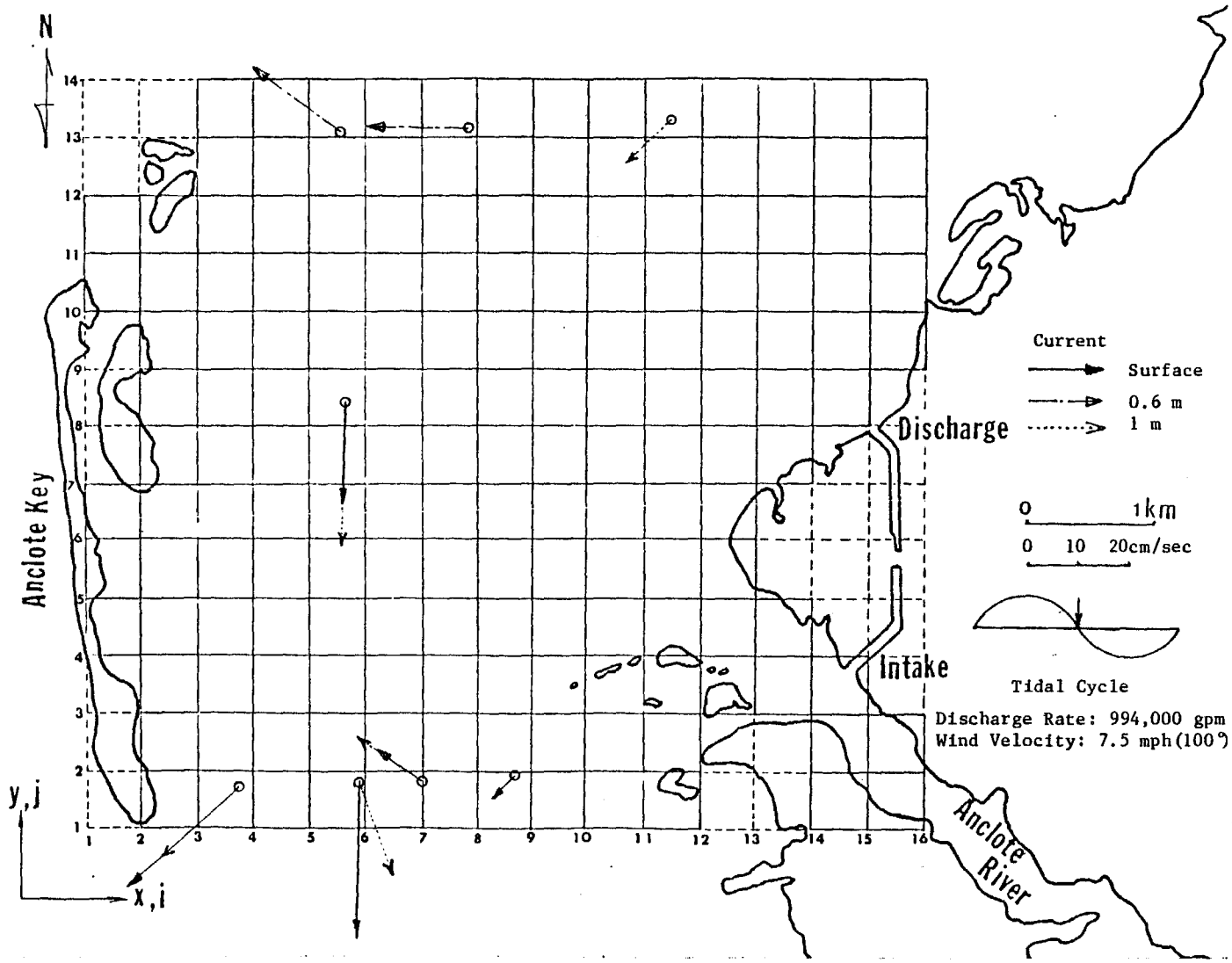

Figure 12. Velocity from in-situ measurement at 1450-1605, June 20, 1978

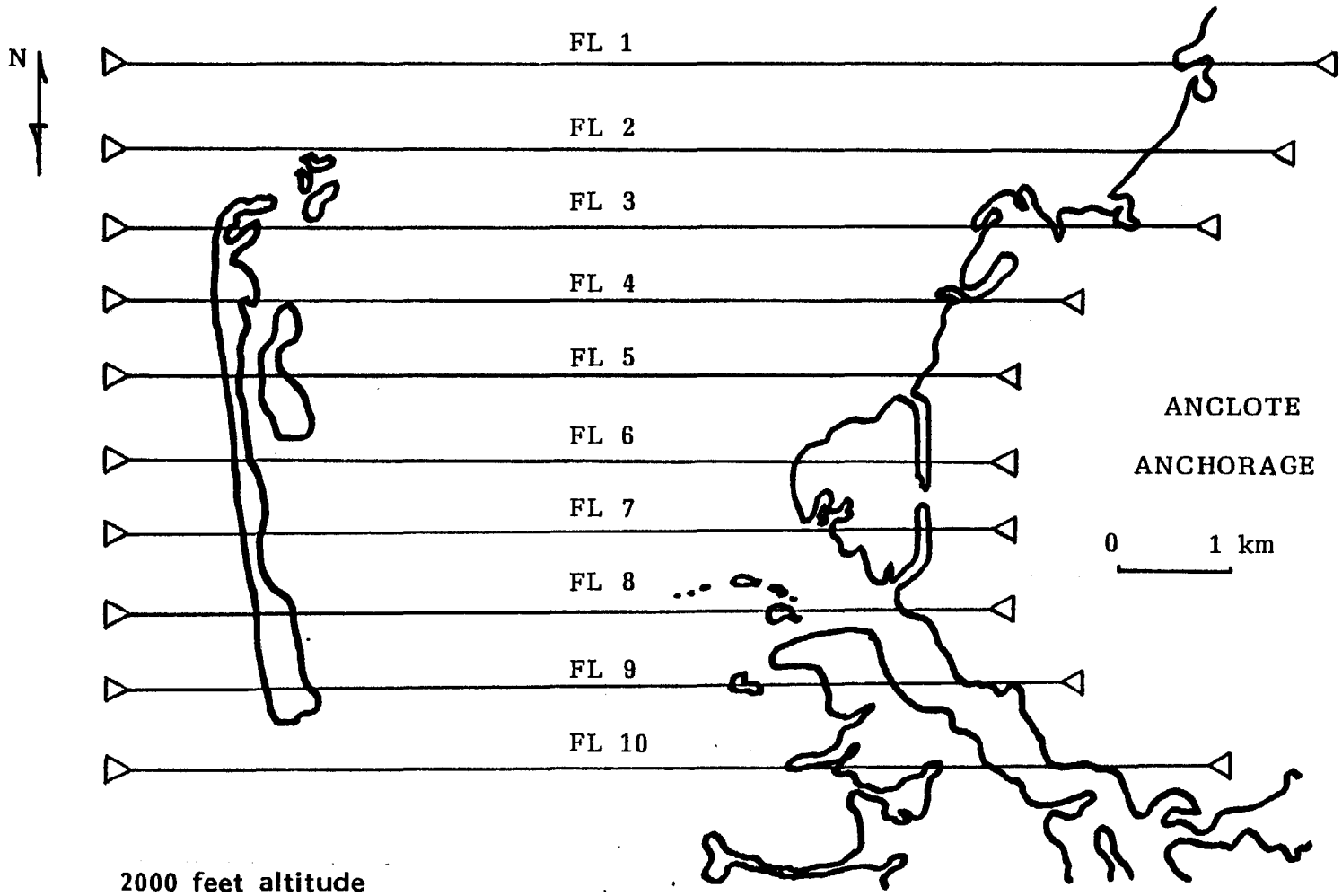

Figure 13. Daytime flight lines on June 19 and 20, 1978

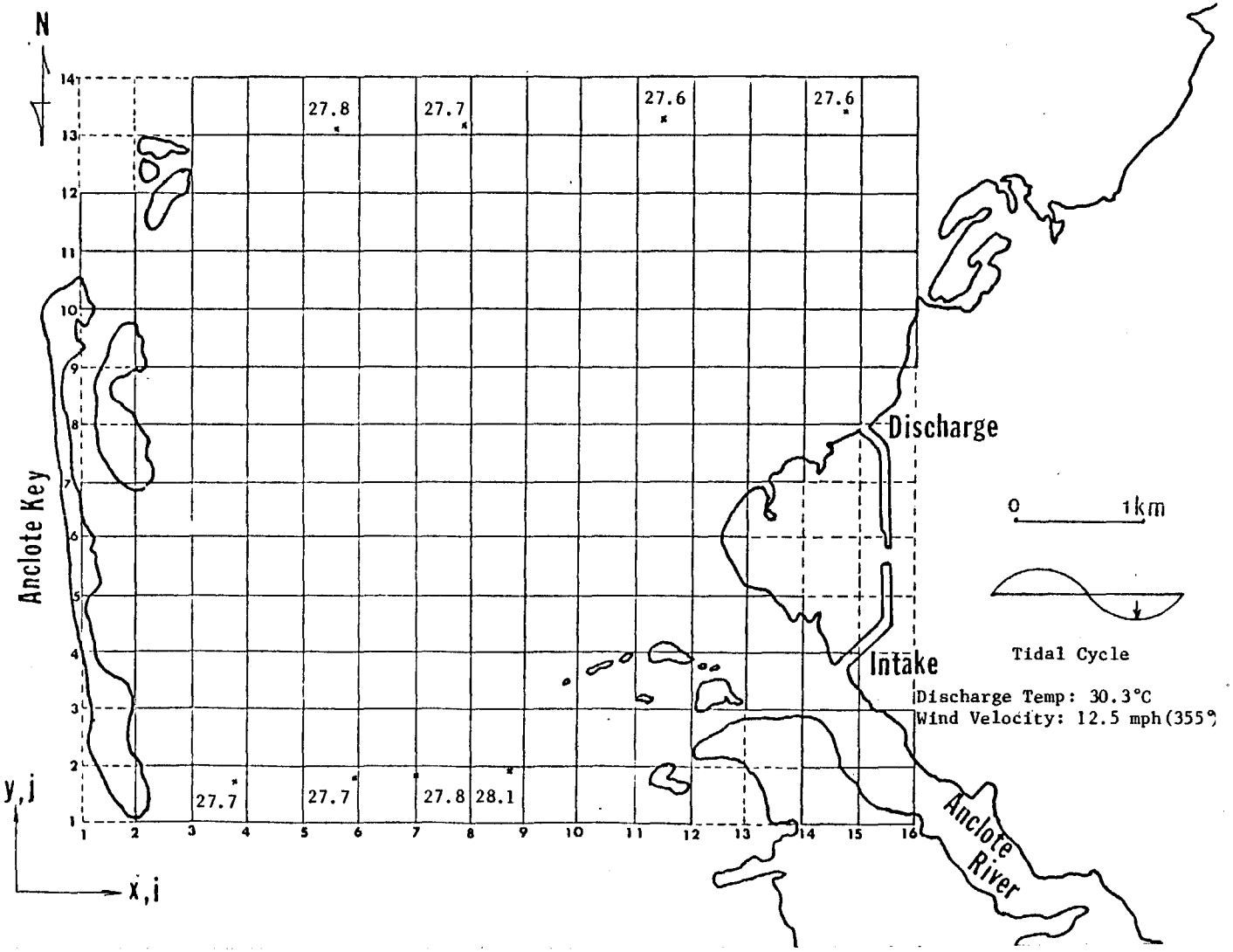

Figure 14. Surface temperature in degree C from in-situ measurement at 1710-1903, June 19, 1978

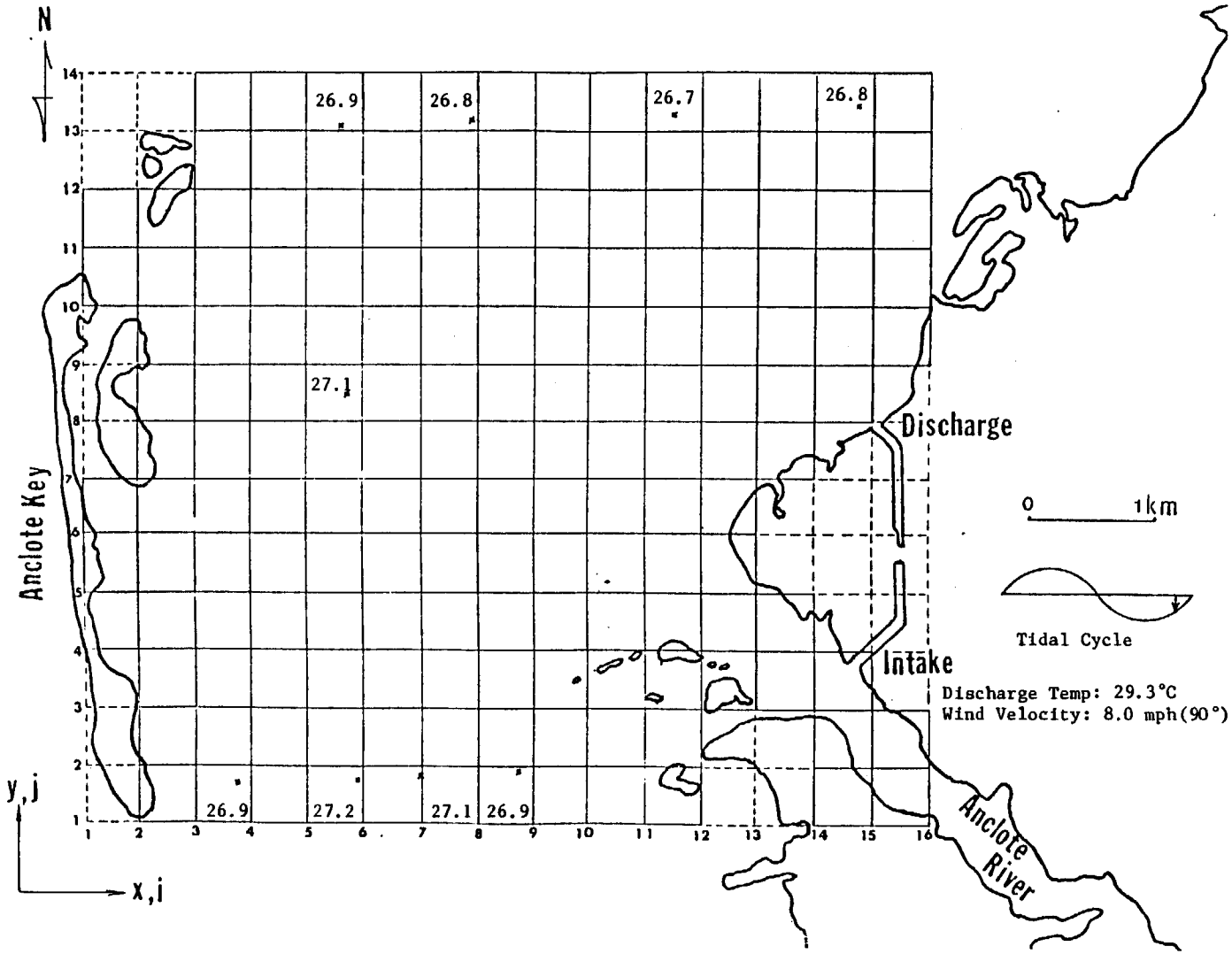

Figure 15. Surface temperature in degree C from in-situ measurement at 0648-0812, June 20, 1978

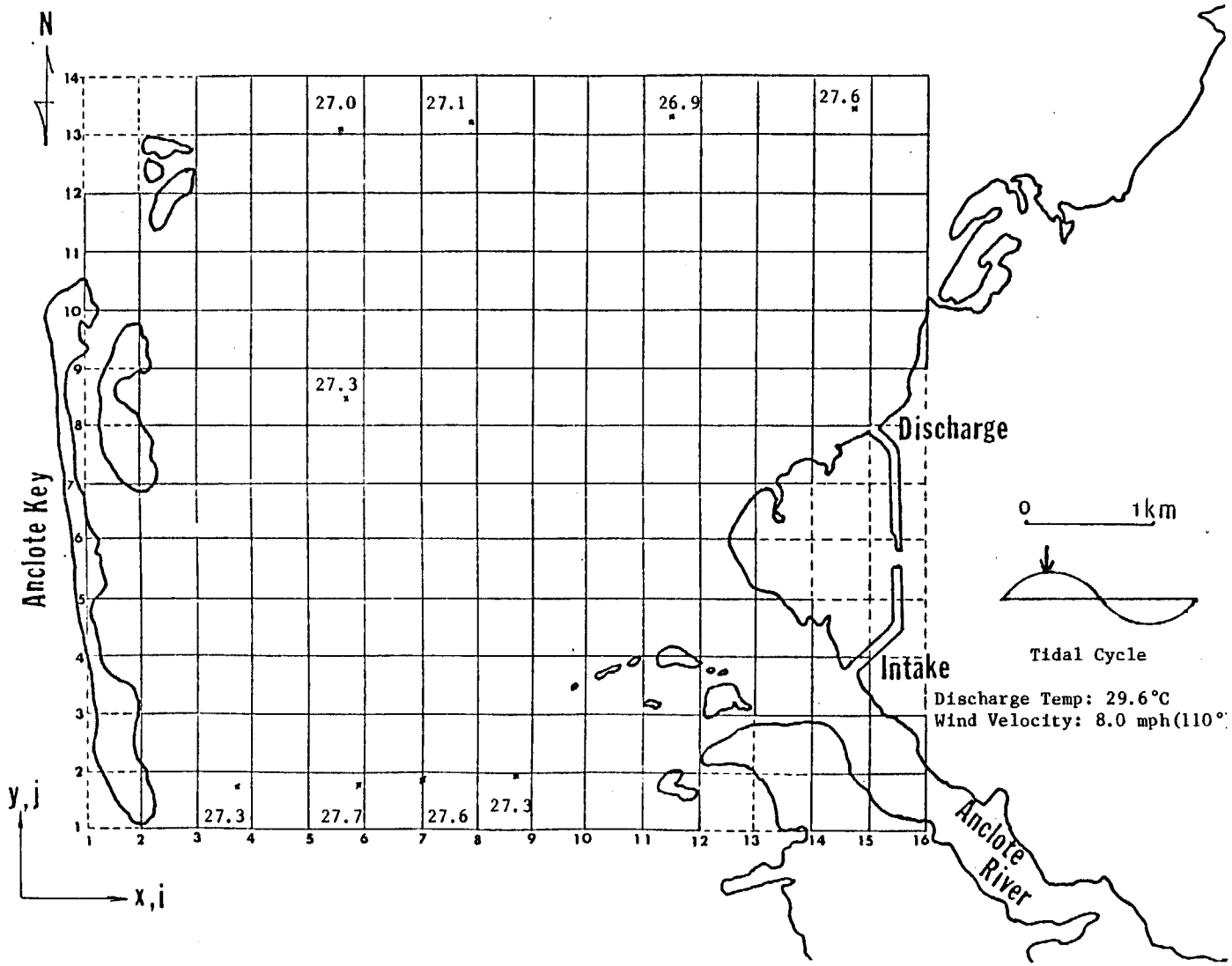

Figure 16. Surface temperature in degree C from in-situ measurement at 1125-1245, June 20, 1978

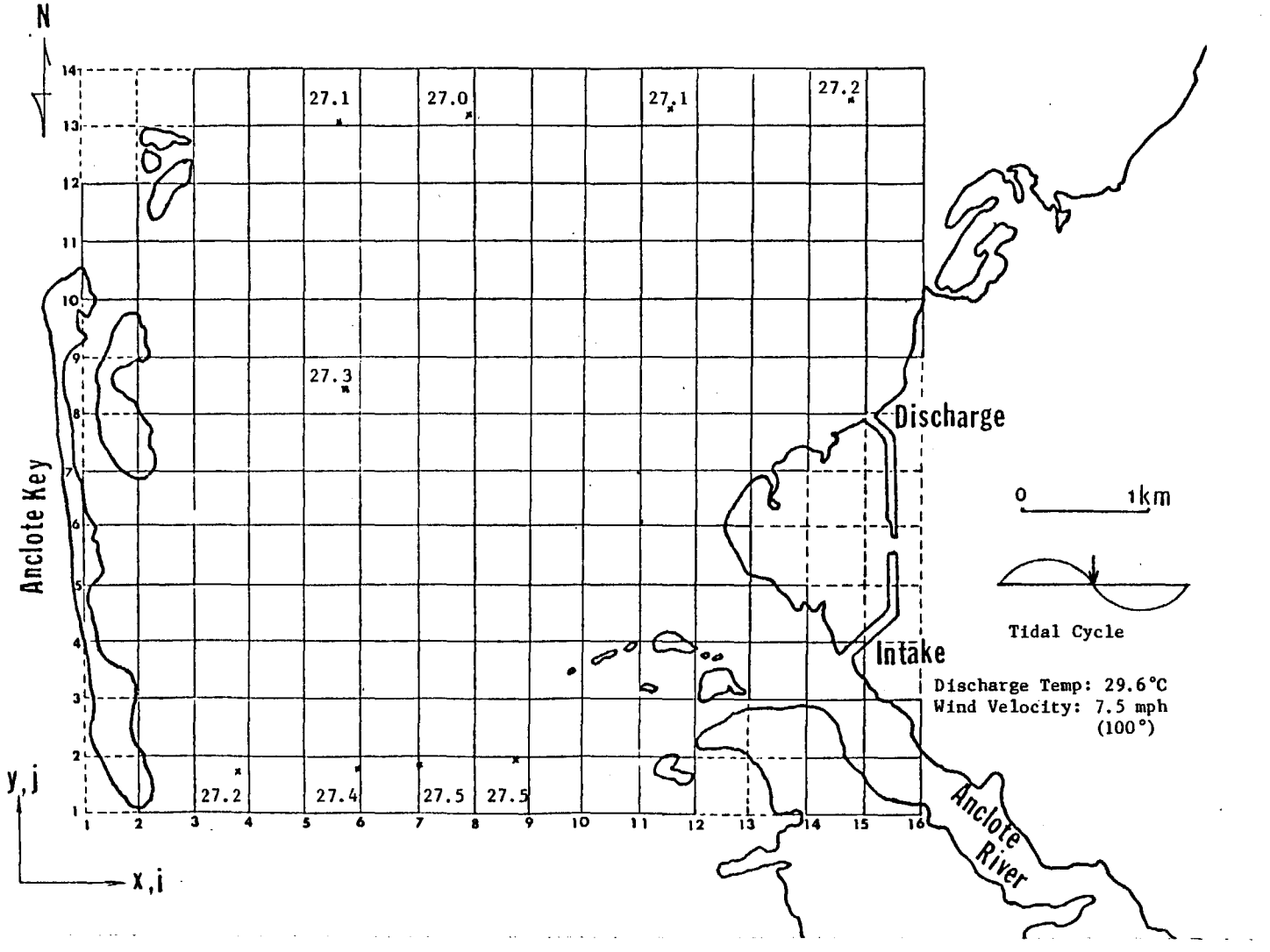

Figure 17. Surface temperature in degree C from in-situ measurement at 1450-1605, June 20, 1978

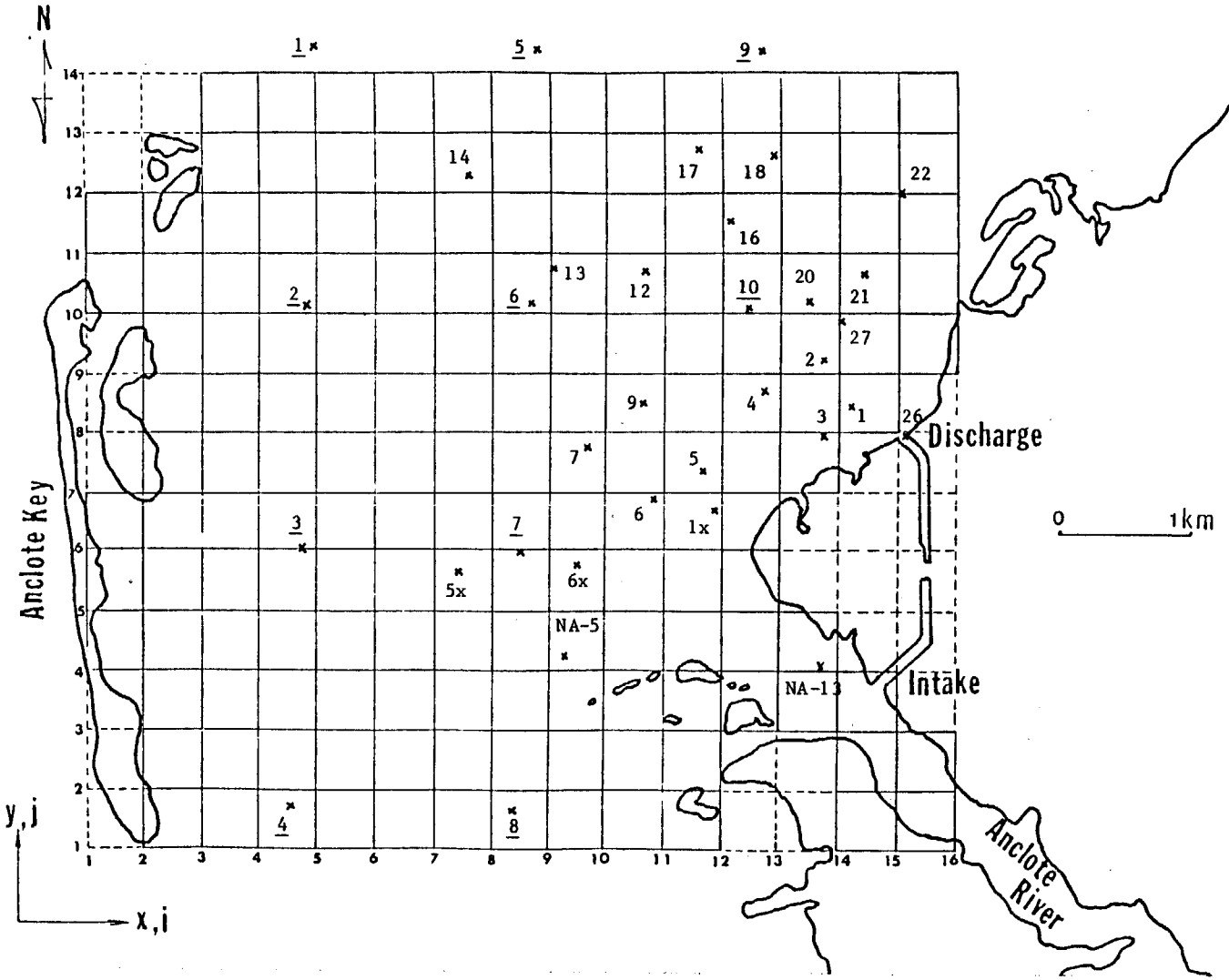

Figure 18. Location of stations for in-situ measurement, January 1979

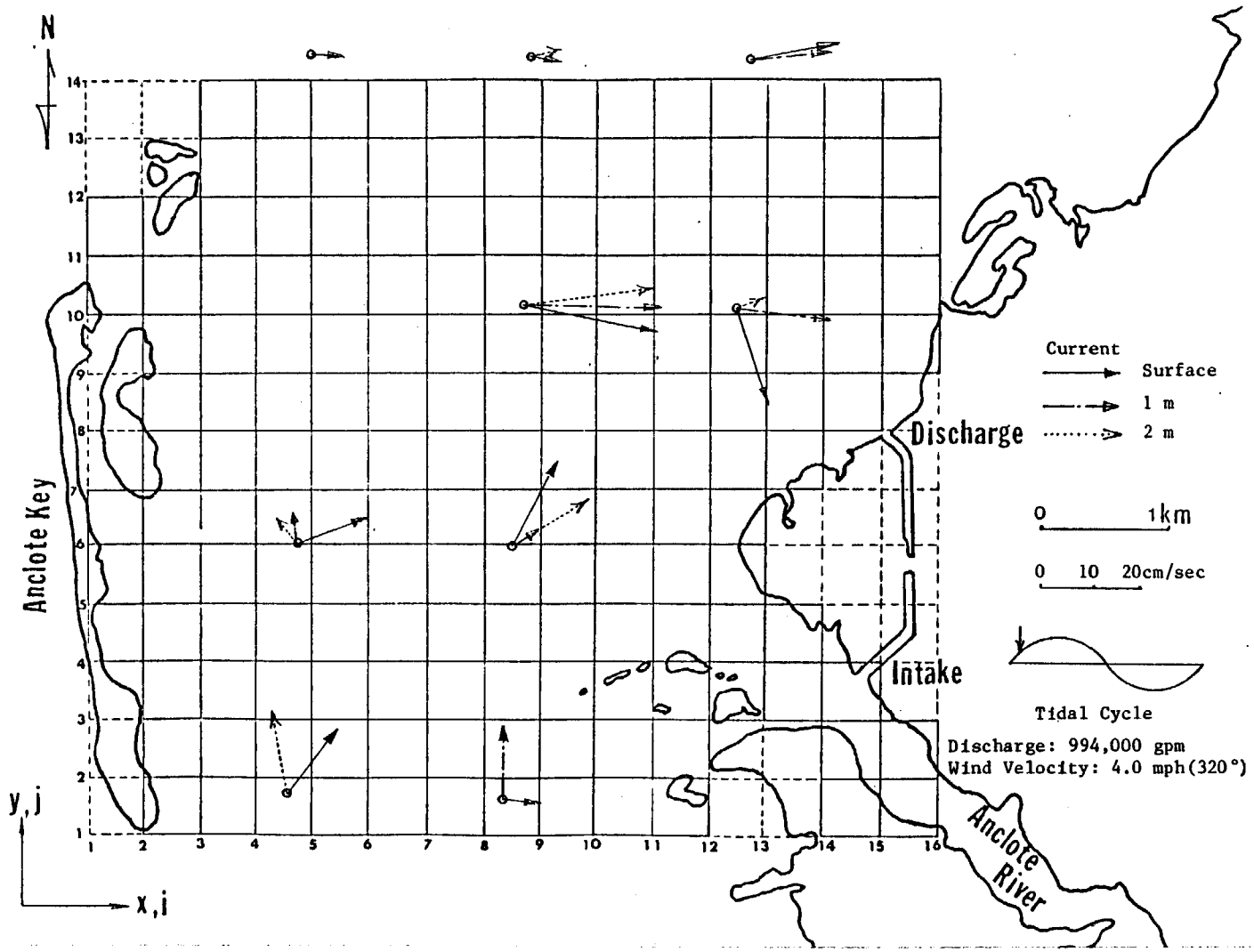

Figure 19. Velocity from in-situ measurement at 1020-1340, January 30, 1979

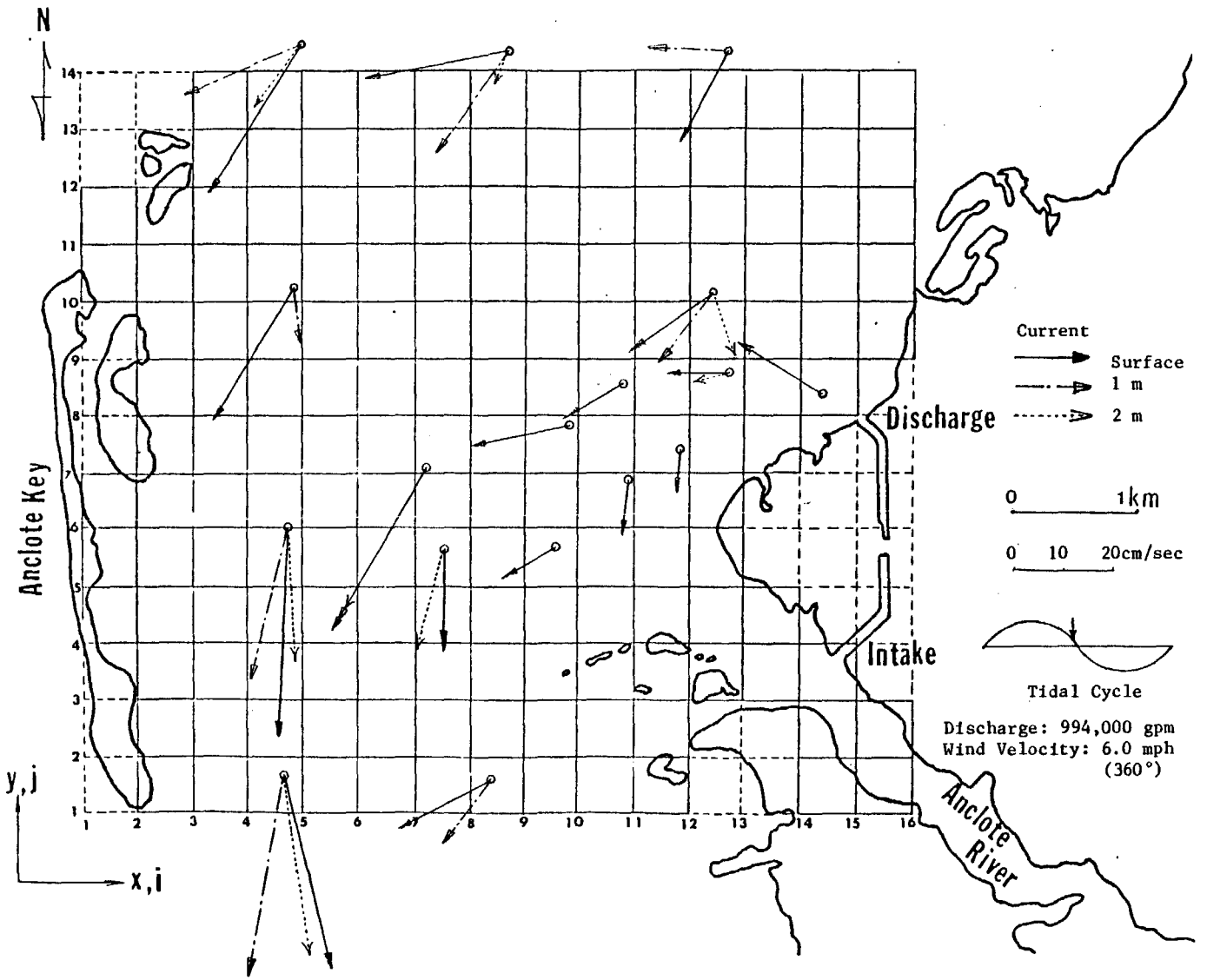

Figure 20. Velocity from in-situ measurement at 1440-1800, January 30, 1979

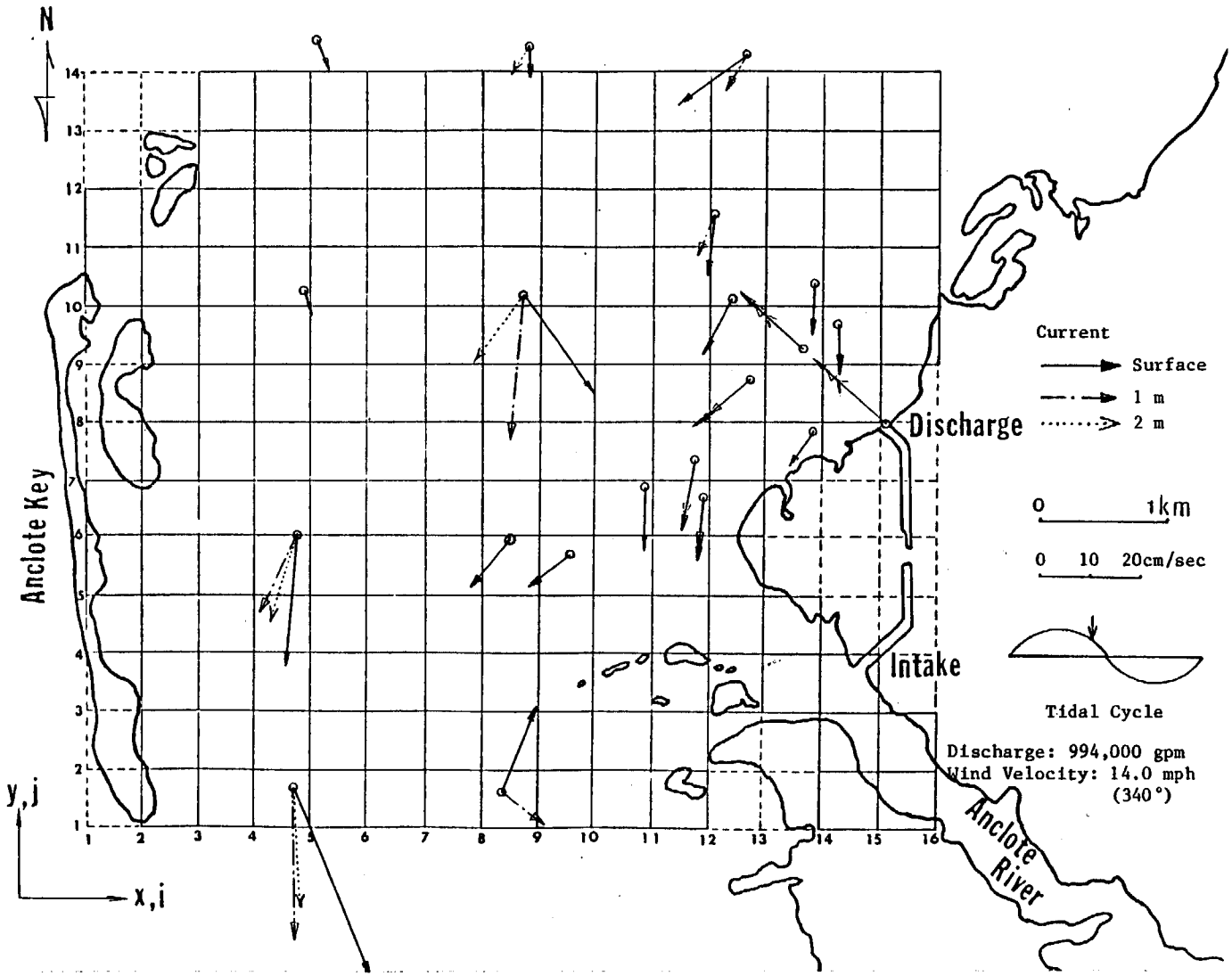

Figure 21. Velocity from in-situ measurement at 1430-1640, February 1, 1979

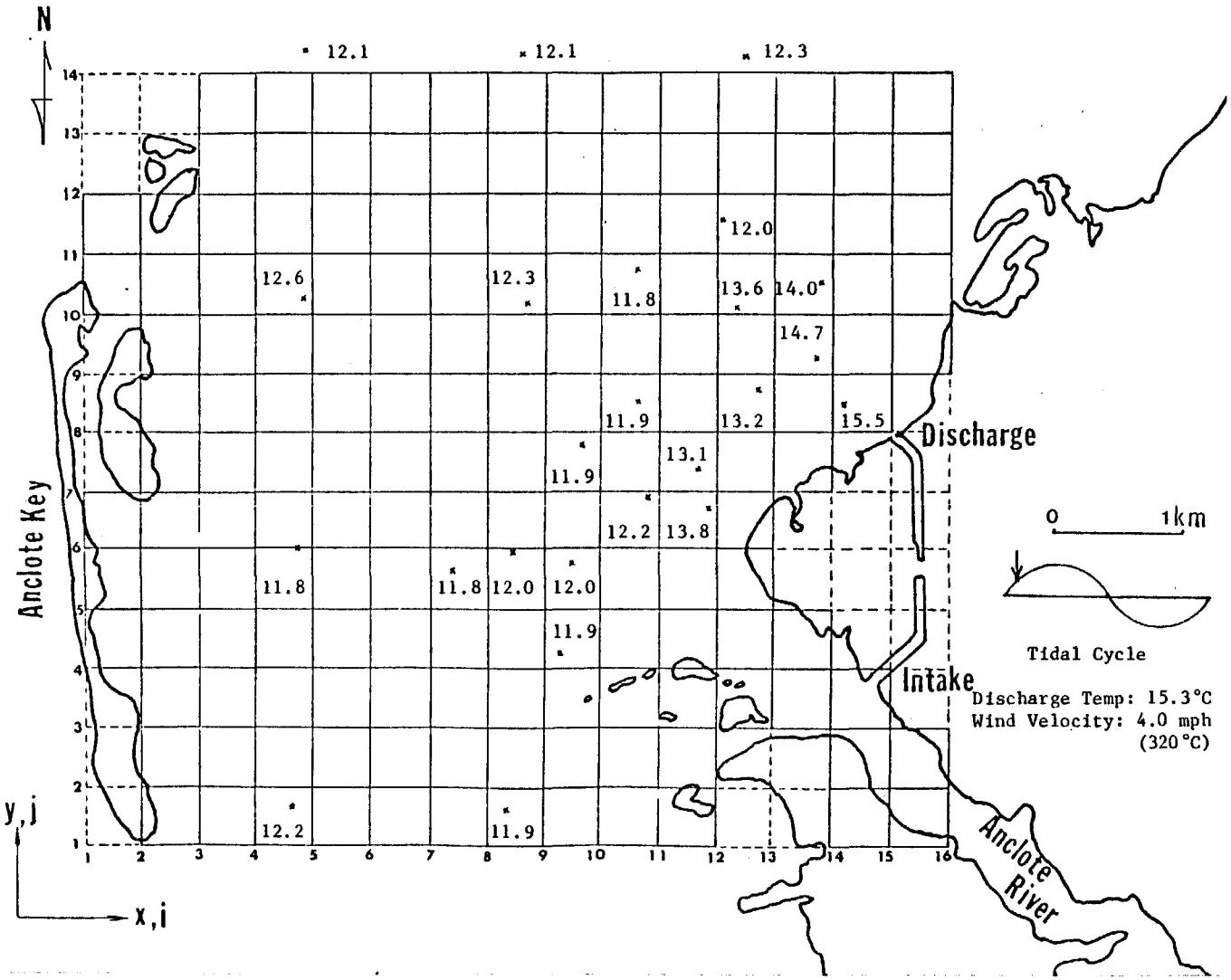

Figure 22. Surface temperature in degree C from in-situ measurement at 1020-1340, January 30, 1979

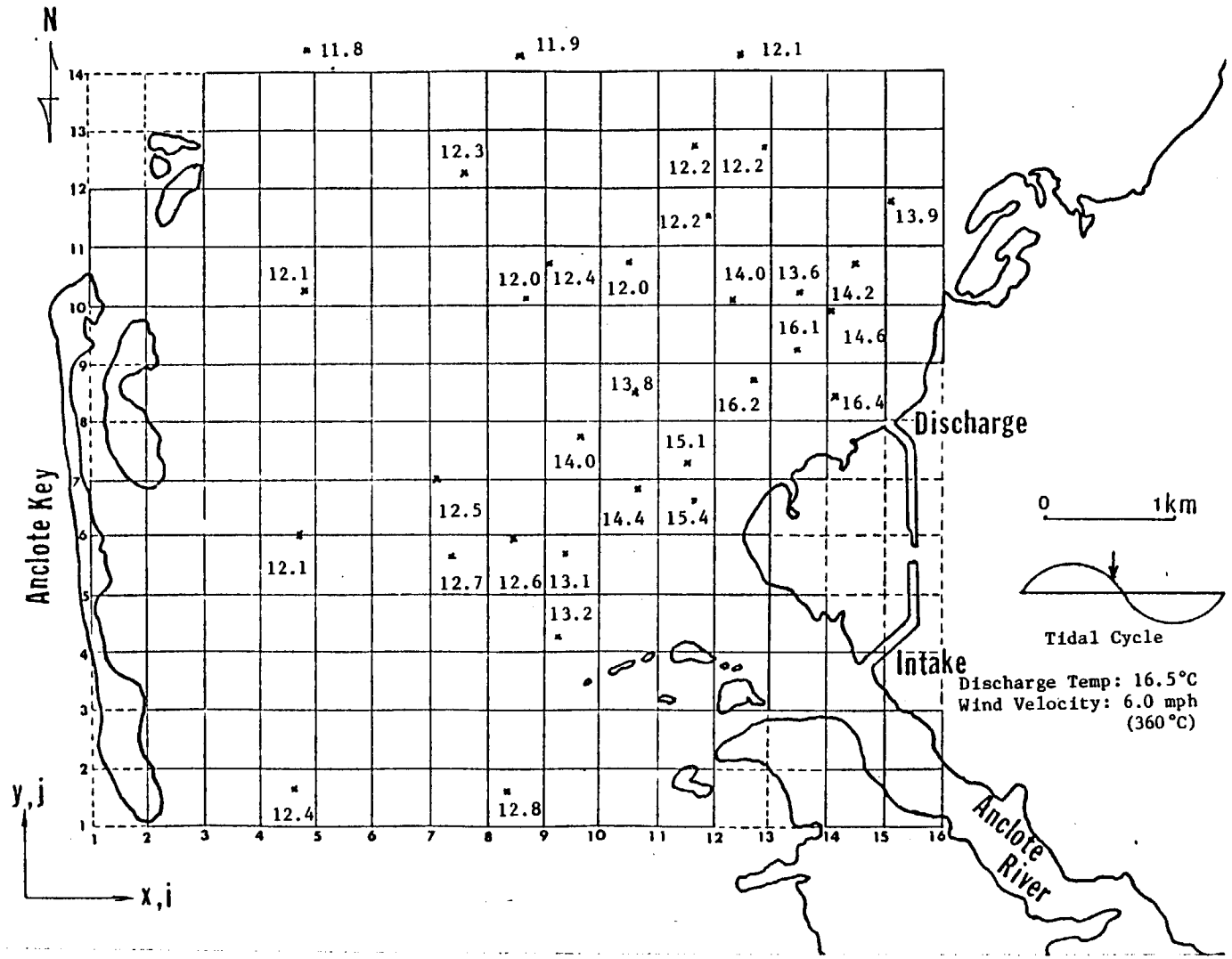

Figure 23. Surface temperature in degree C from in-situ measurement at 1440-1800, January 30, 1979

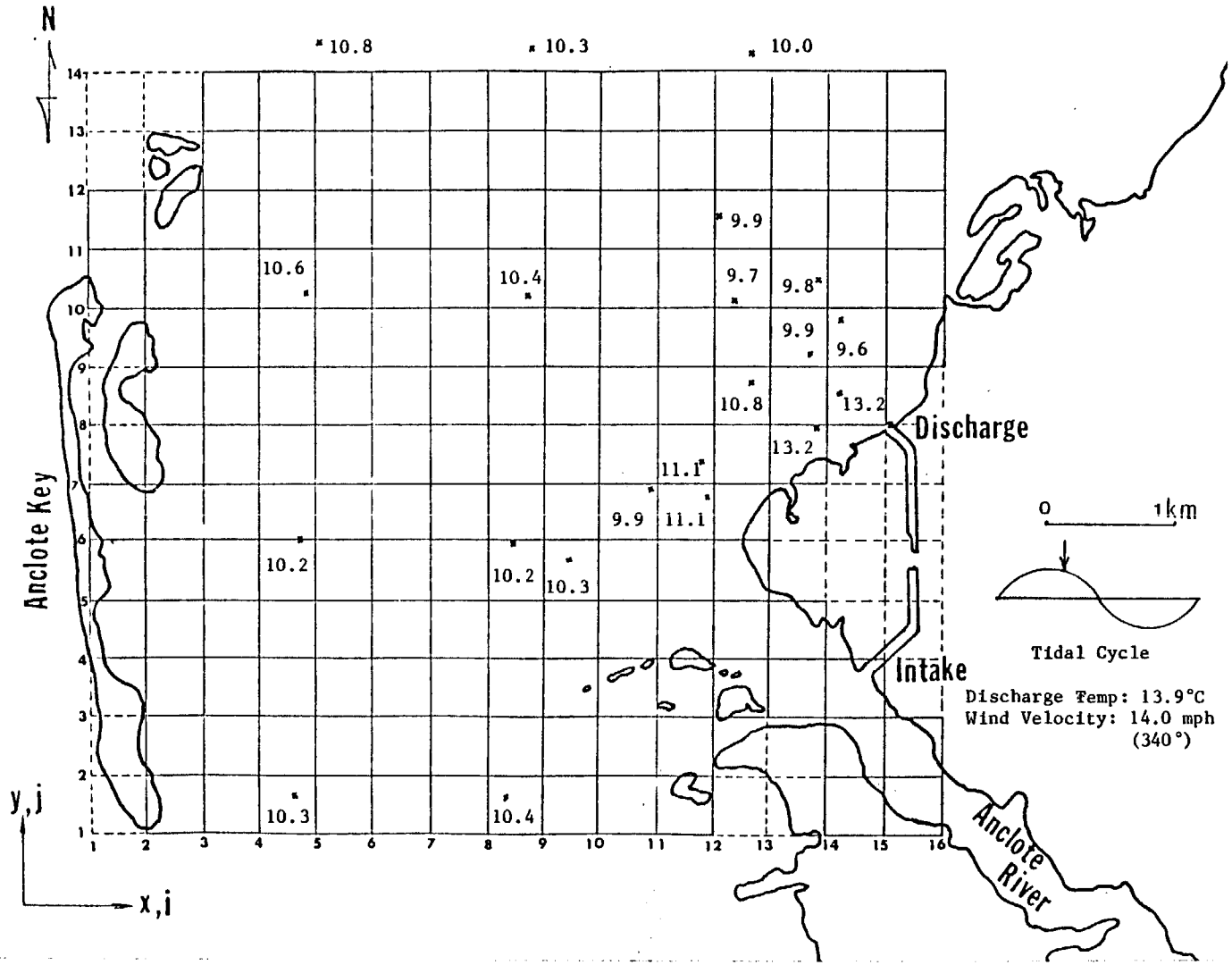

Figure 24. Surface temperature in degree C from in-situ measurement at 1430-1640, February 1, 1979

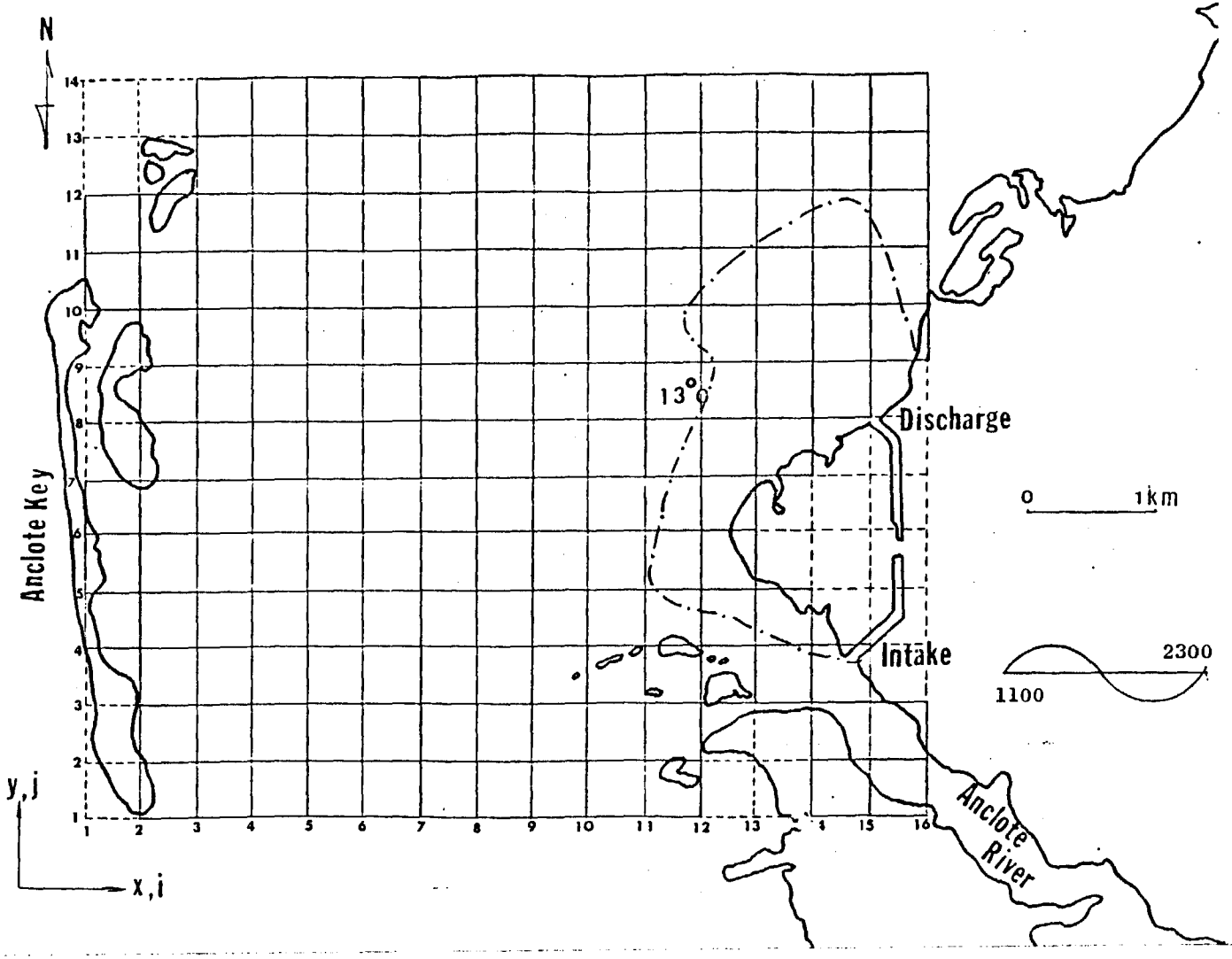

Figure 25. Surface temperature from in-situ measurement at 1020-1340, January 30, 1979

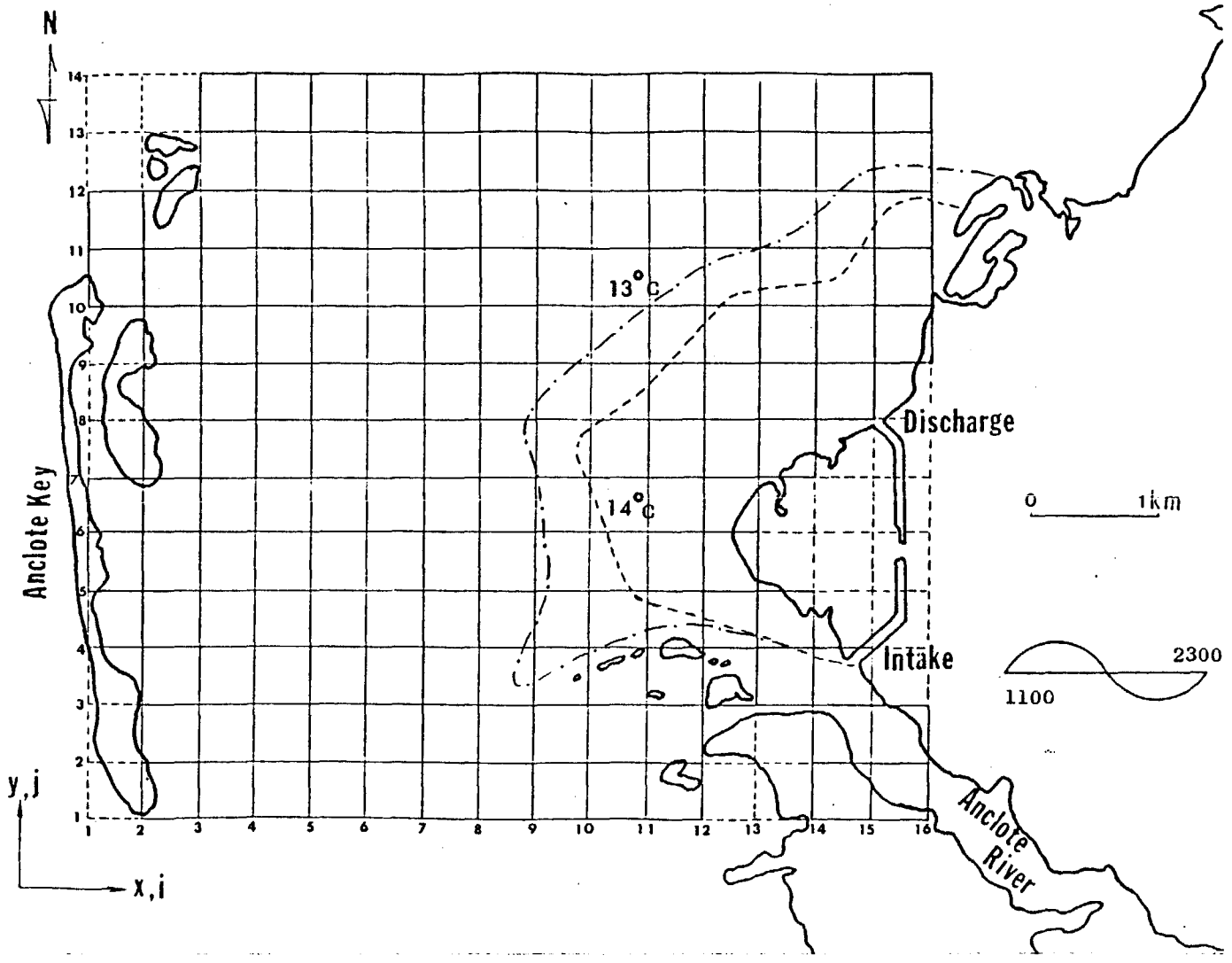

Figure 26. Surface temperature from in-situ measurement at 1440-1800, January 30, 1979

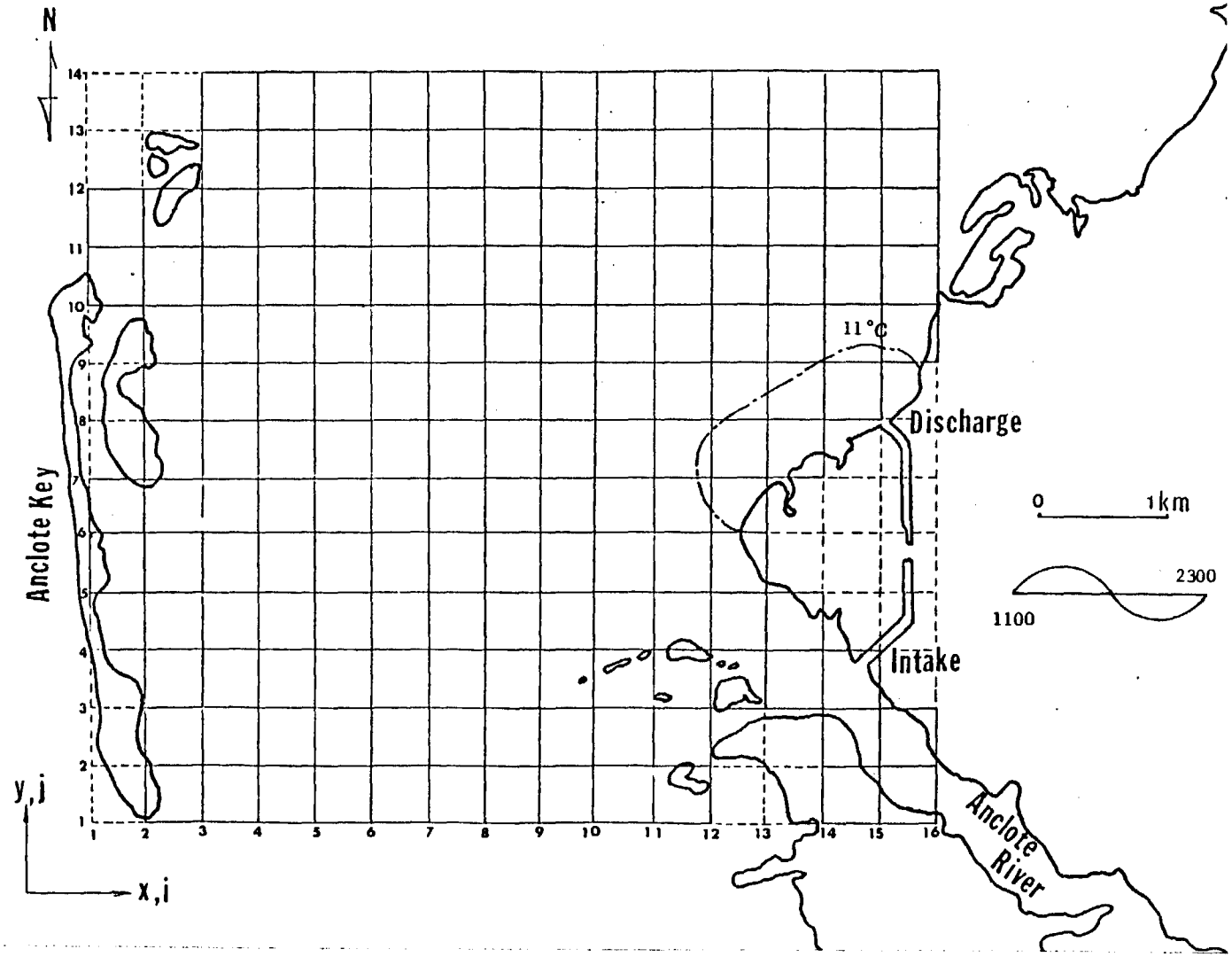

Figure 27. Surface temperature from in-situ measurement at 1430-1640, February 1, 1979

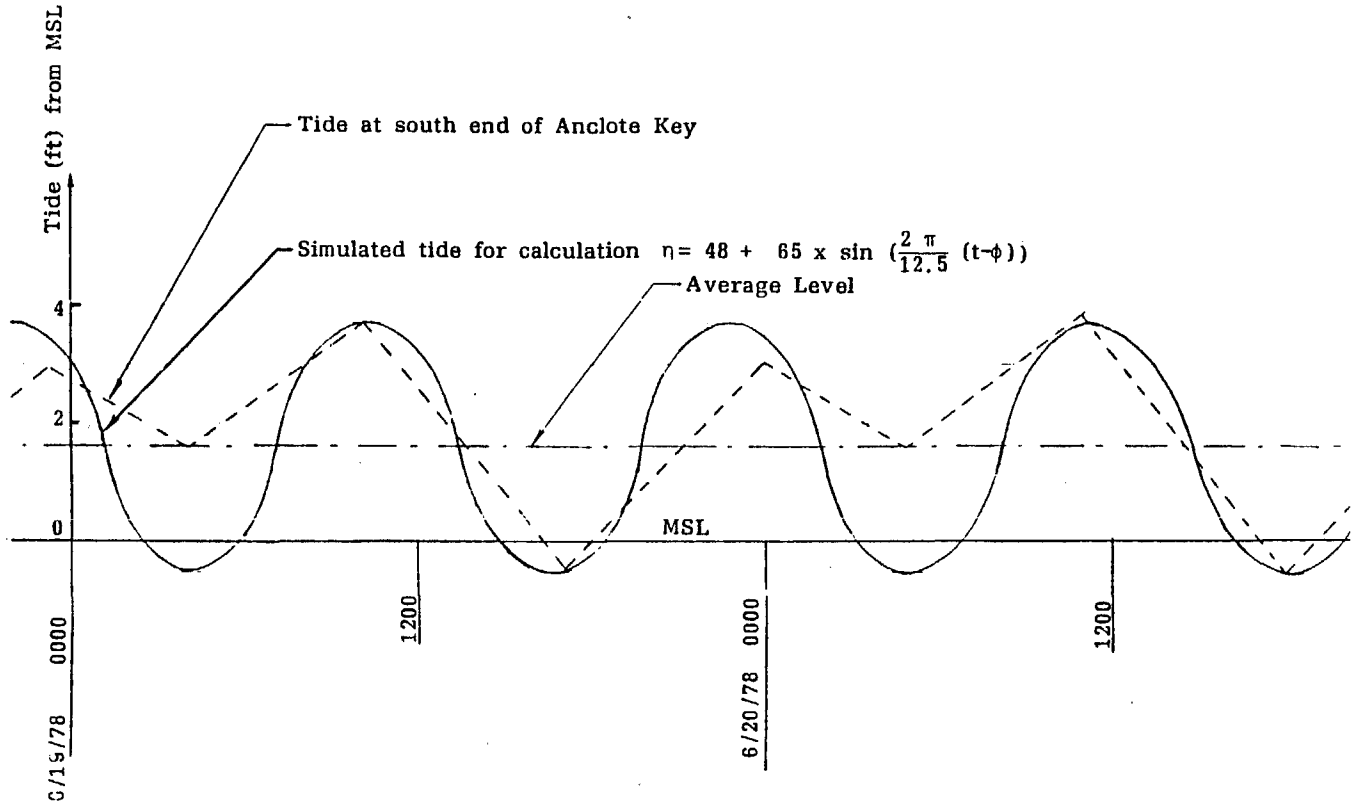

Figure 28. Semidiurnal tide for June 19-20, 1978 at south end of Anclote Key

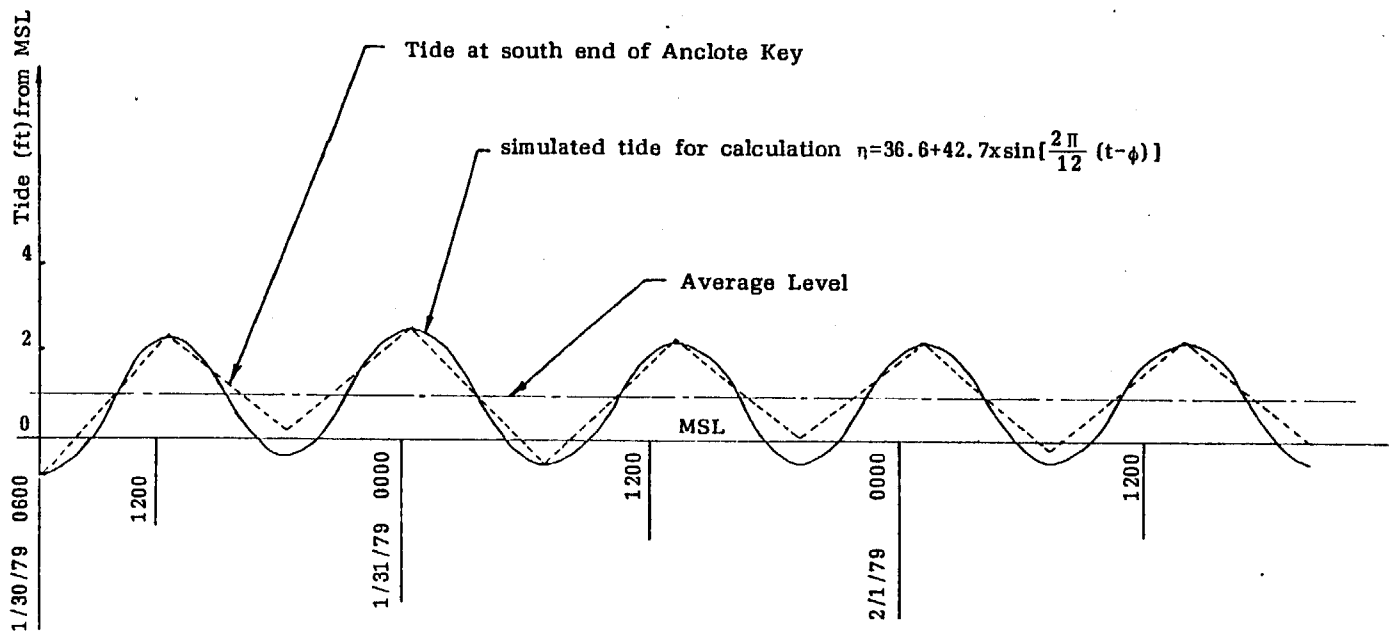

Figure 29. Semidiurnal tide for January 30–February 1, 1980 at south end of Anclote Key

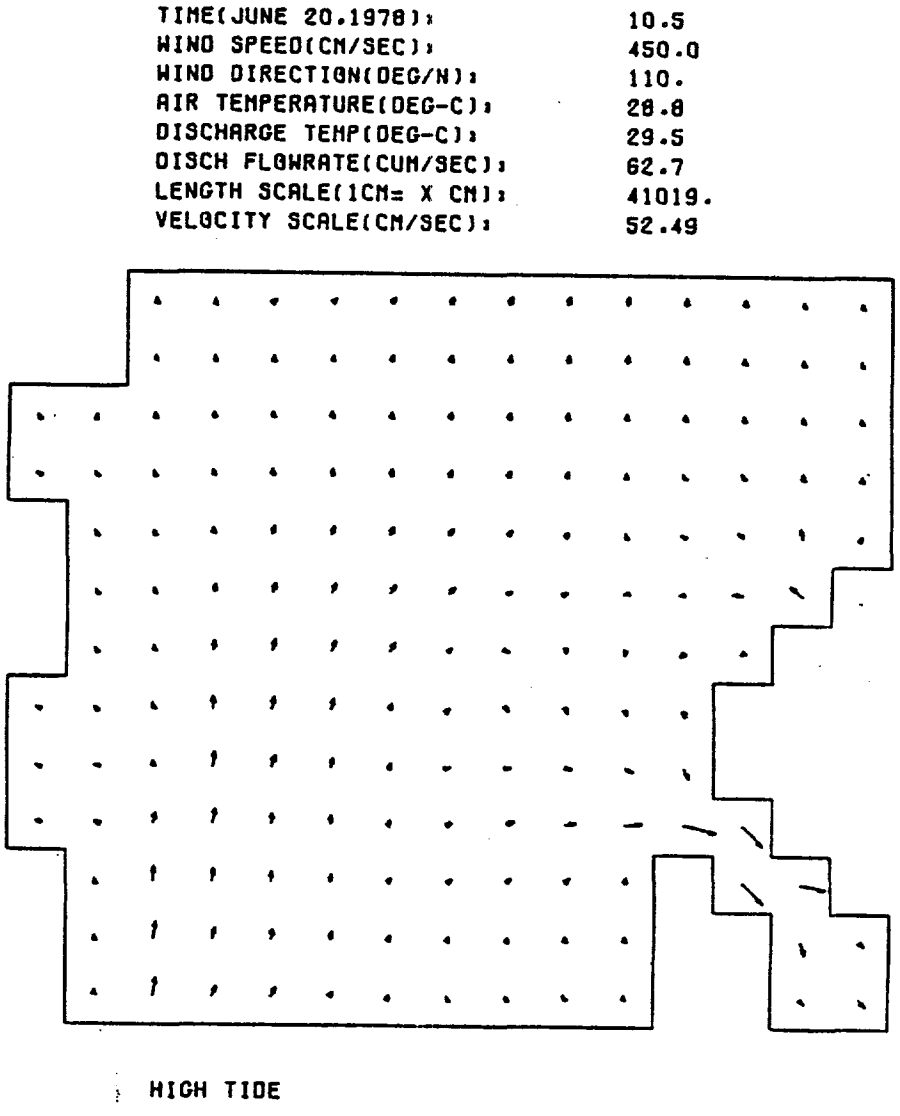

Figure 30. Surface velocity, Anclote Anchorage by modeling

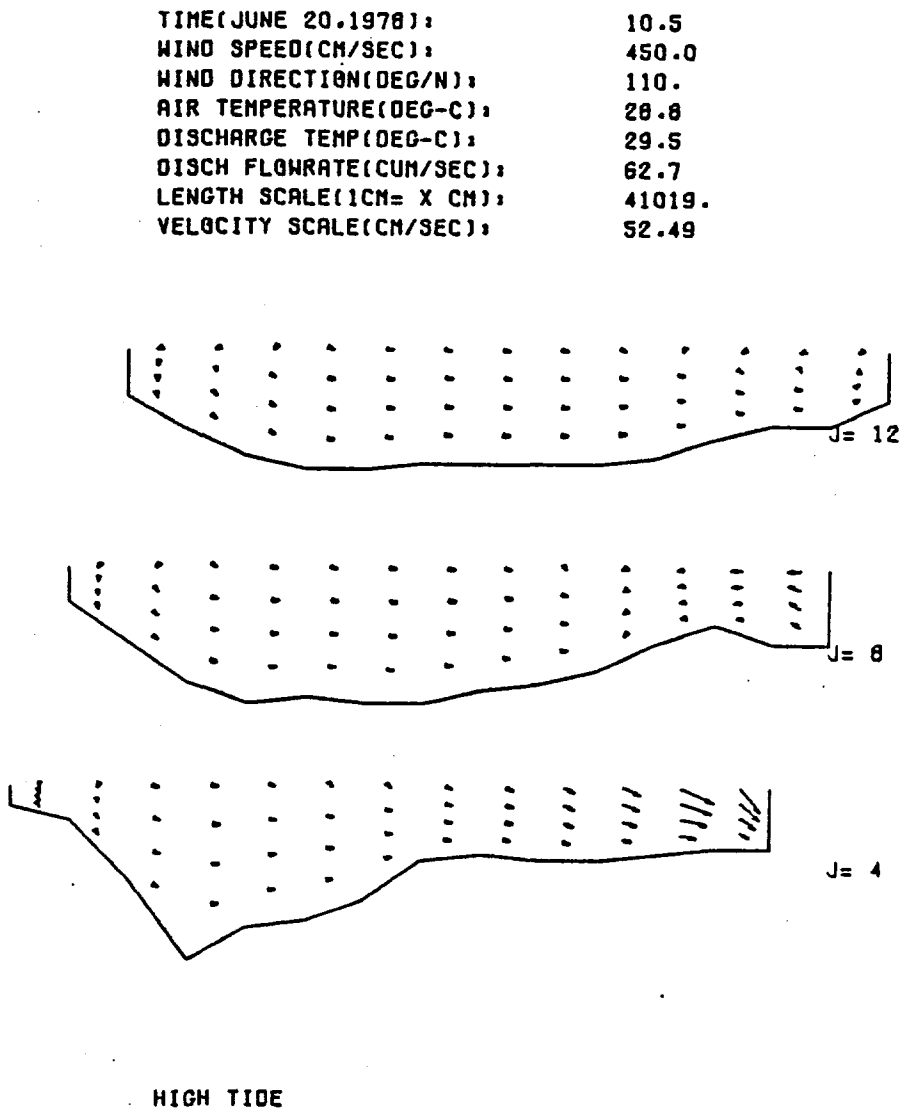

Figure 31. UW velocity, Anclote Anchorage by modeling

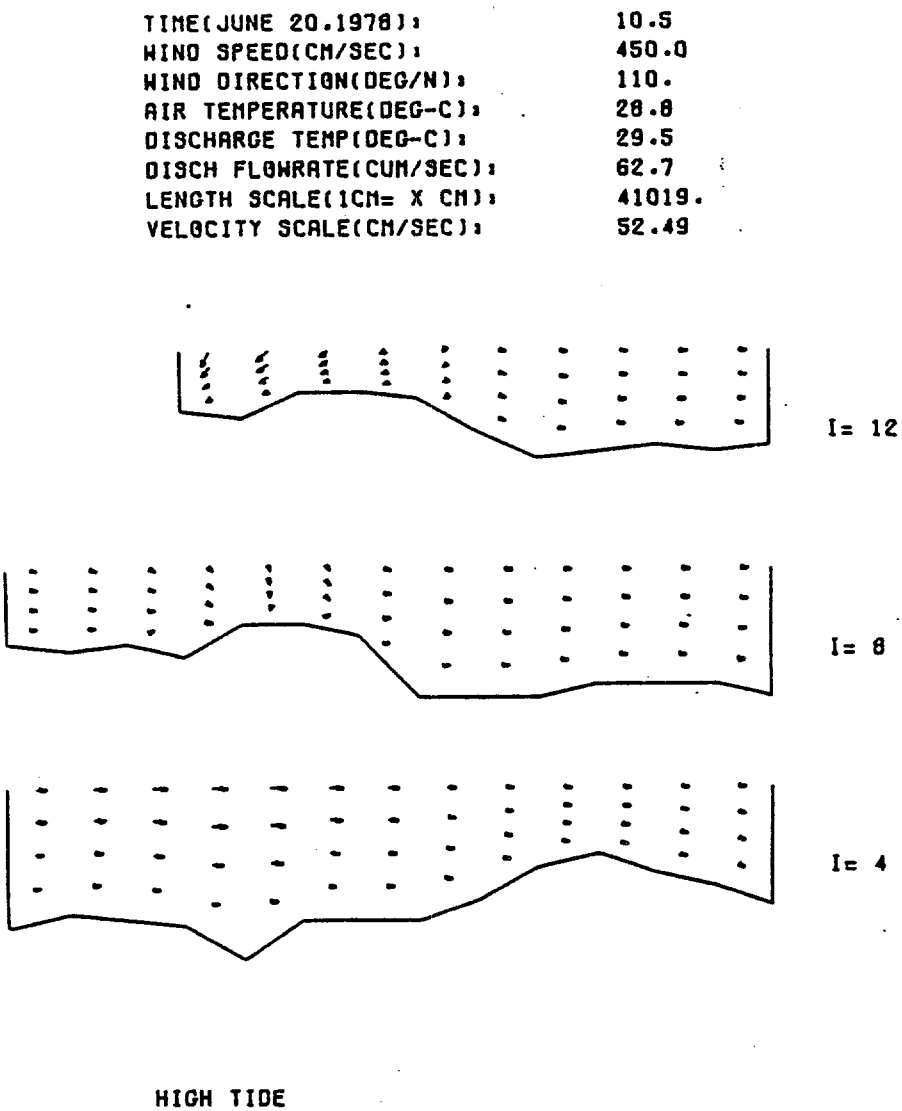

Figure 32. VW velocity, Anclote Anchorage by modeling

TIME(JUNE 20,1978):	11.5
WIND SPEED(CM/SEC):	420.0
WIND DIRECTION(DEG/N):	110.
AIR TEMPERATURE(DEG-C):	29.1
DISCHARGE TEMP(DEG-C):	29.6
DISCH FLOWRATE(CUM/SEC):	62.7
LENGTH SCALE(1CM= X CM):	41019.
VELOCITY SCALE(CM/SEC):	52.49

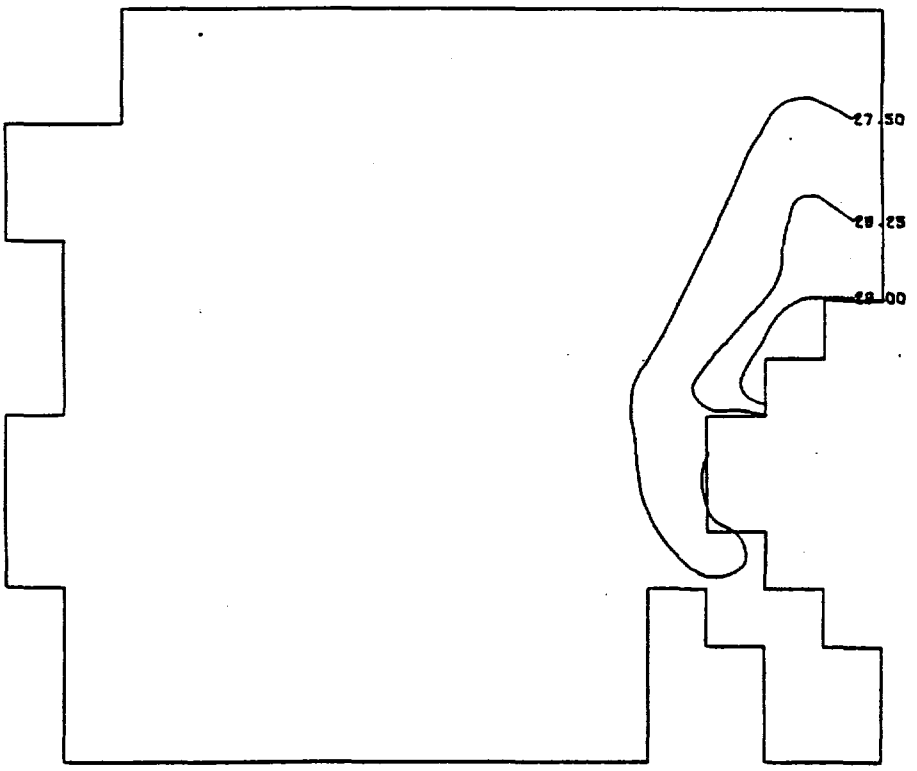

HIGH TIDE

Figure 33. Temperature from IR

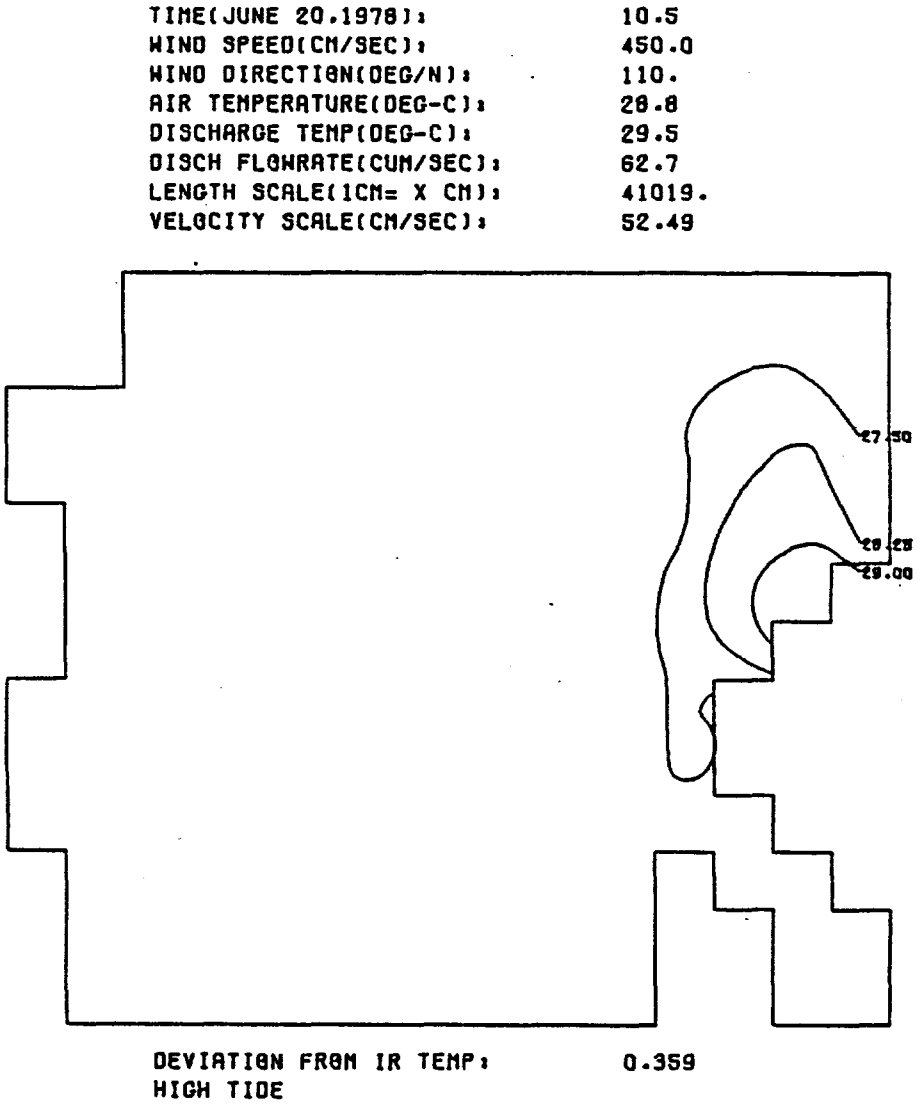

Figure 34. Surface temperature, Anclote Anchorage by modeling

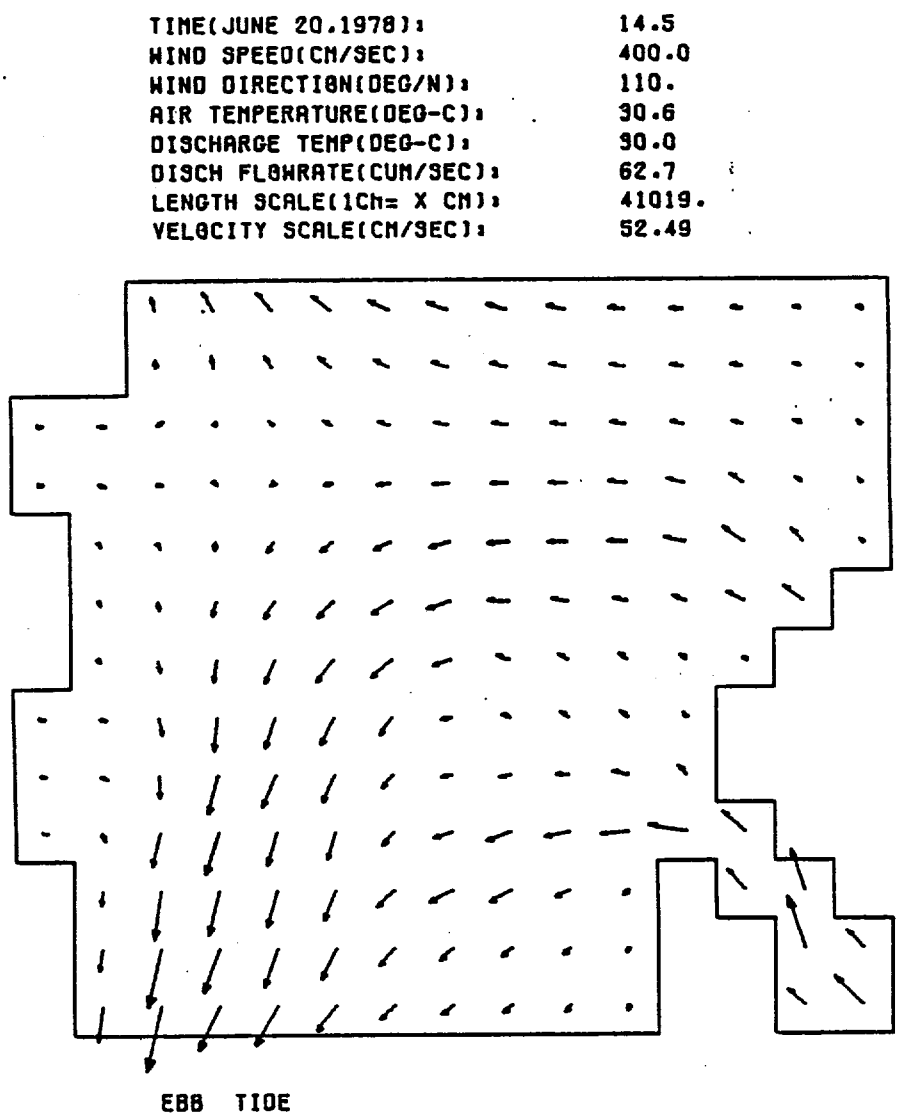

Figure 35. Surface velocity, Anclote Anchorage by modeling

TIME(JUNE 20,1978):	14.5
WIND SPEED(CM/SEC):	400.0
WIND DIRECTION(DEG/N):	110.
AIR TEMPERATURE(DEG-C):	30.6
DISCHARGE TEMP(DEG-C):	30.0
DISCH FLOWRATE(CUM/SEC):	62.7
LENGTH SCALE(1CM= X CM):	41019.
VELOCITY SCALE(CM/SEC):	52.49

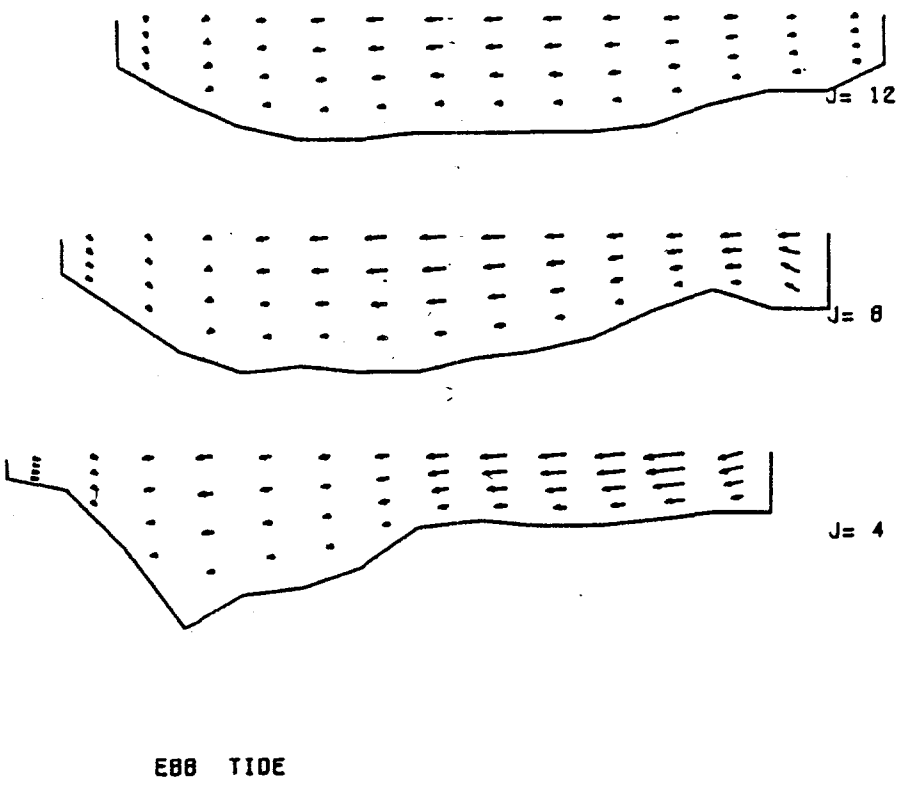

E88 TIDE

Figure 36. UW velocity, Anclote Anchorage by modeling

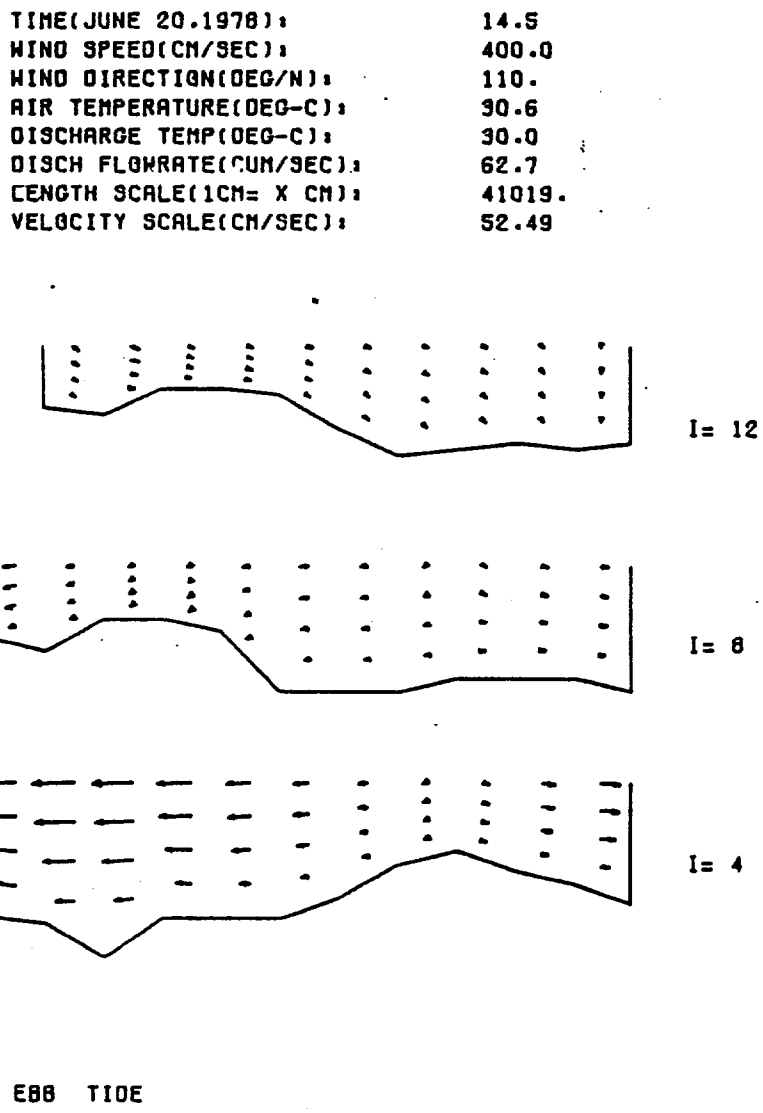

Figure 37. VW velocity, Anclote Anchorage by modeling

TIME(JUNE 20,1978):	15.0
WIND SPEED(CM/SEC):	400.0
WIND DIRECTION(DEG/N):	110.
AIR TEMPERATURE(DEG-C):	30.6
DISCHARGE TEMP(DEG-C):	29.6
DISCH FLOWRATE(CUM/SEC):	62.7
LENGTH SCALE(1CM= X CM):	41019.
VELOCITY SCALE(CM/SEC):	52.49

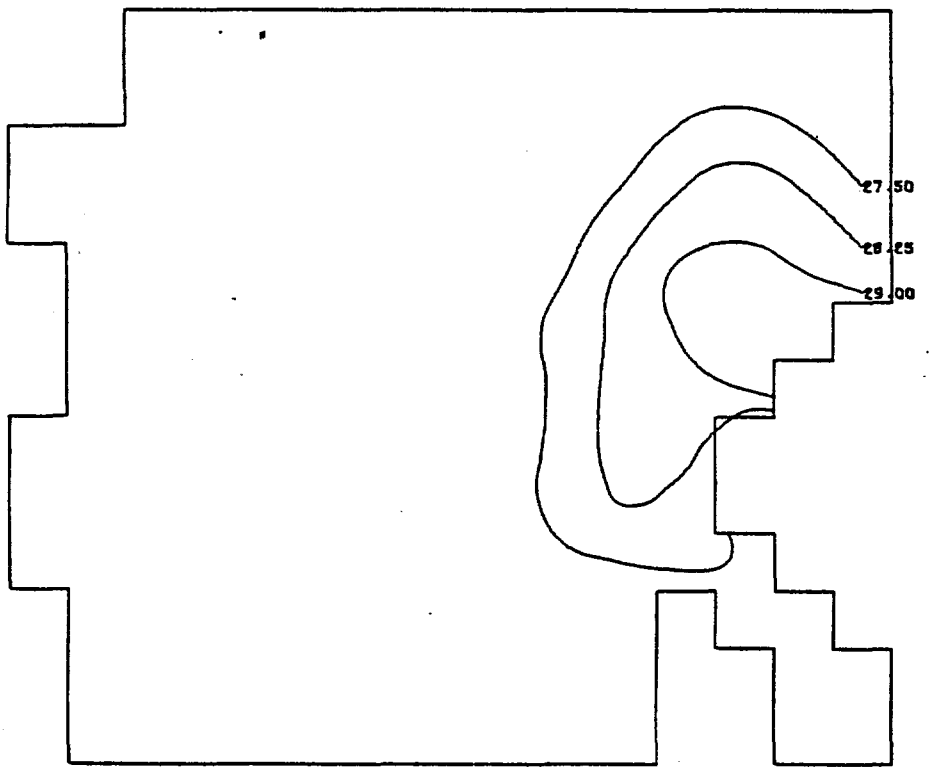

EBB TIDE

Figure 38. Temperature from IR

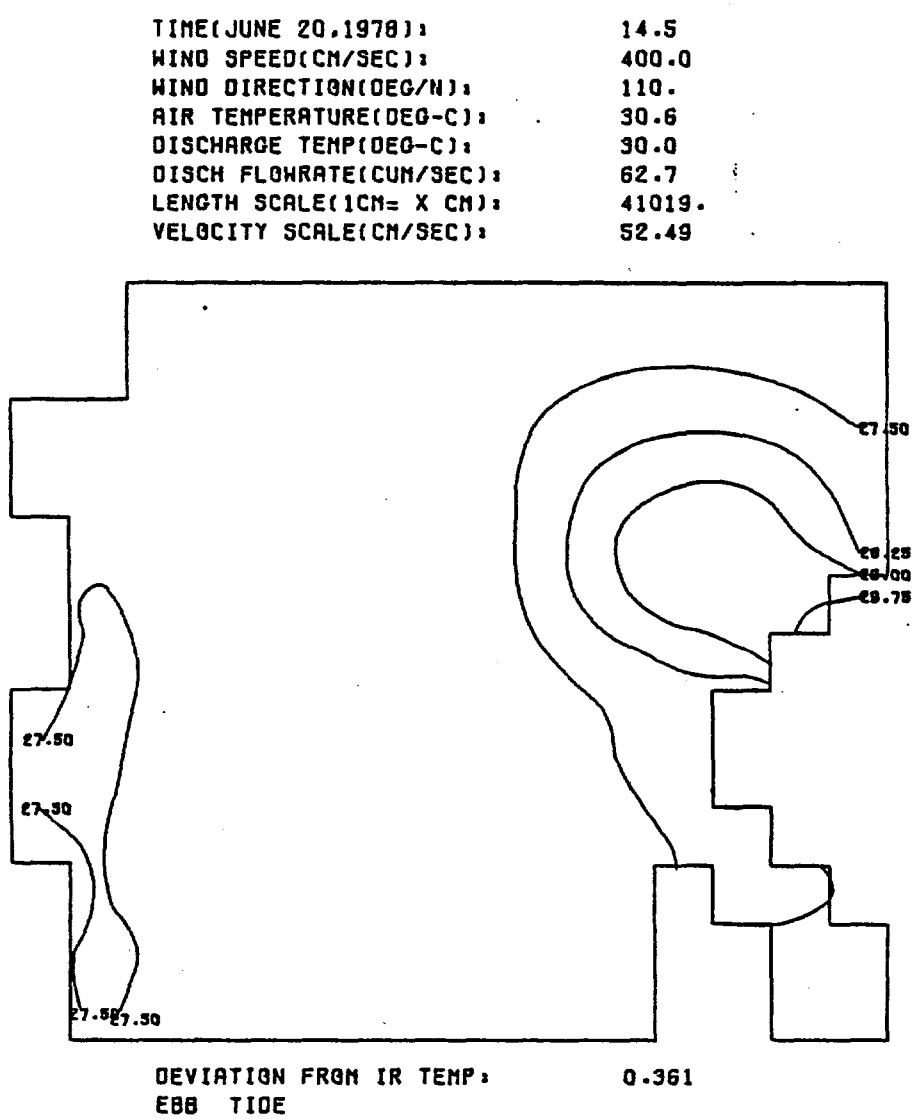

Figure 39. Surface temperature, Anclote Anchorage by modeling

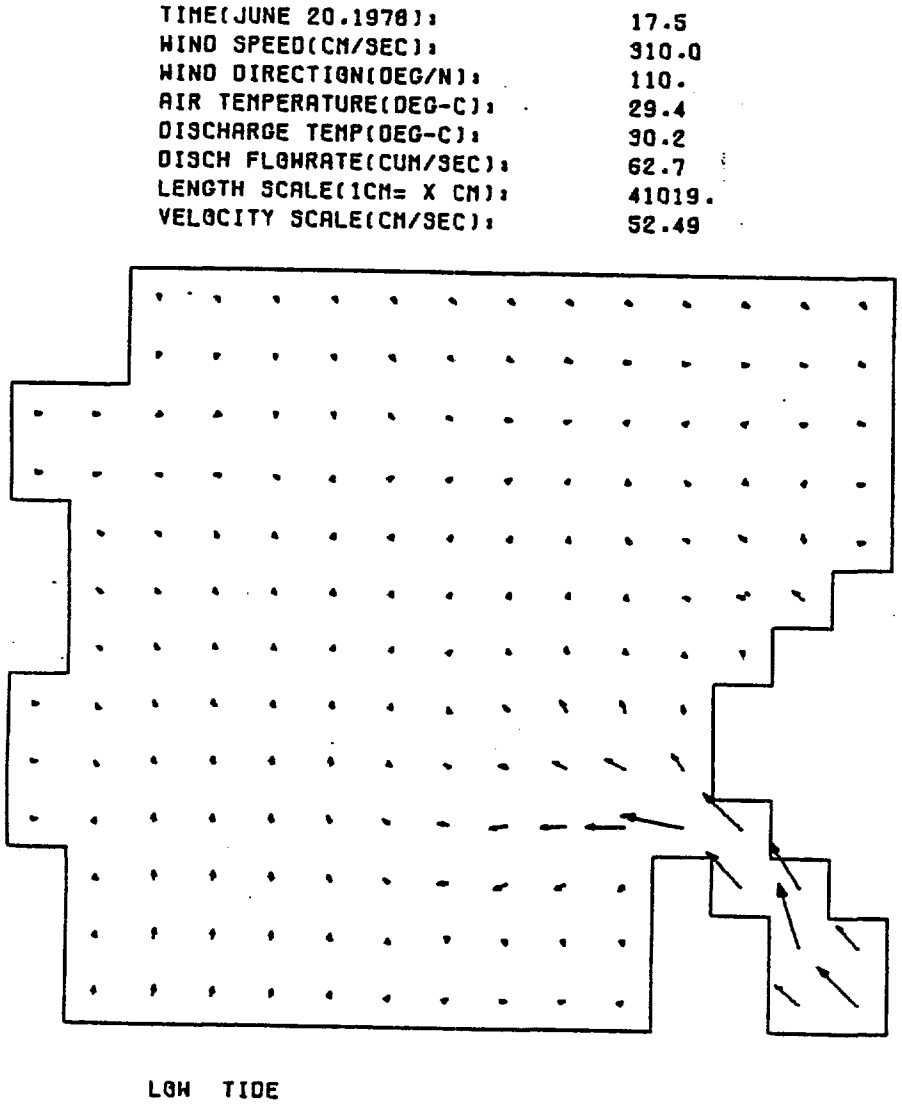

Figure 40. Surface velocity, Anclote Anchorage by Modeling

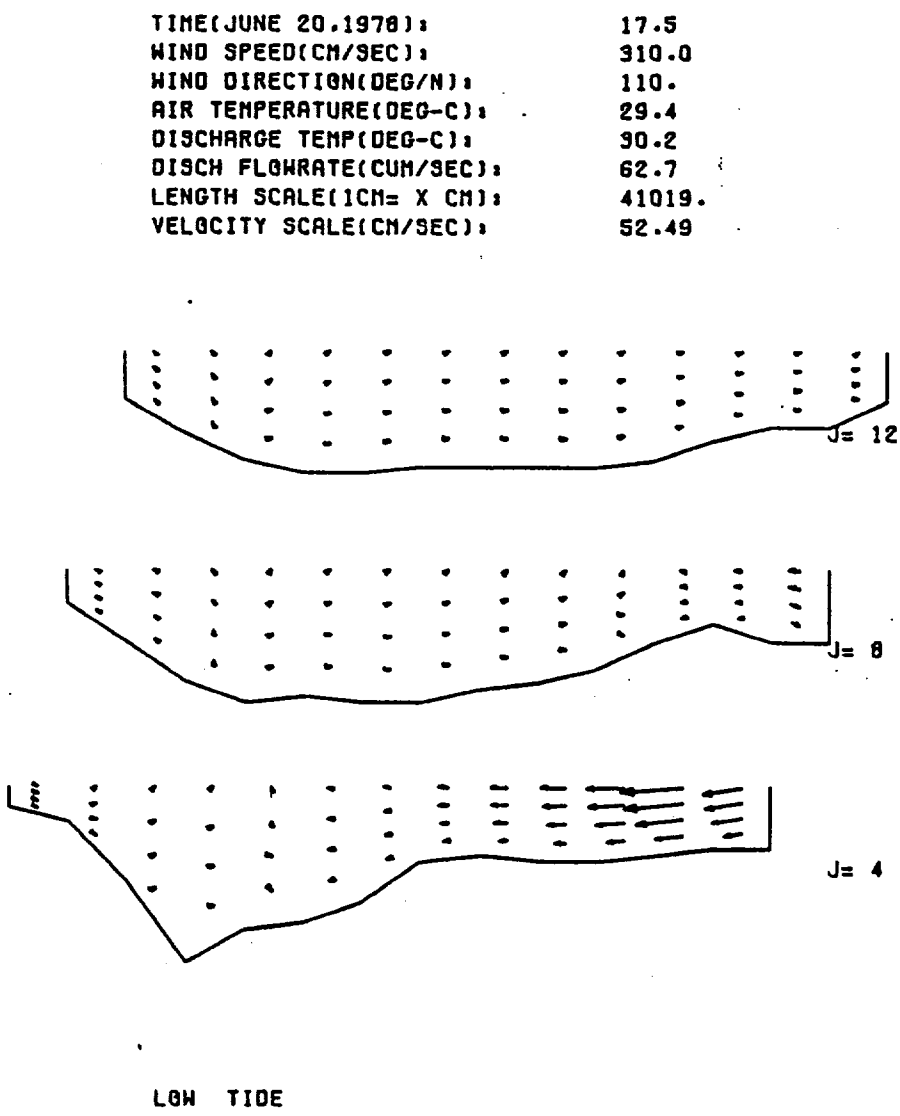

Figure 41. UW velocity, Anclote Anchorage by modeling

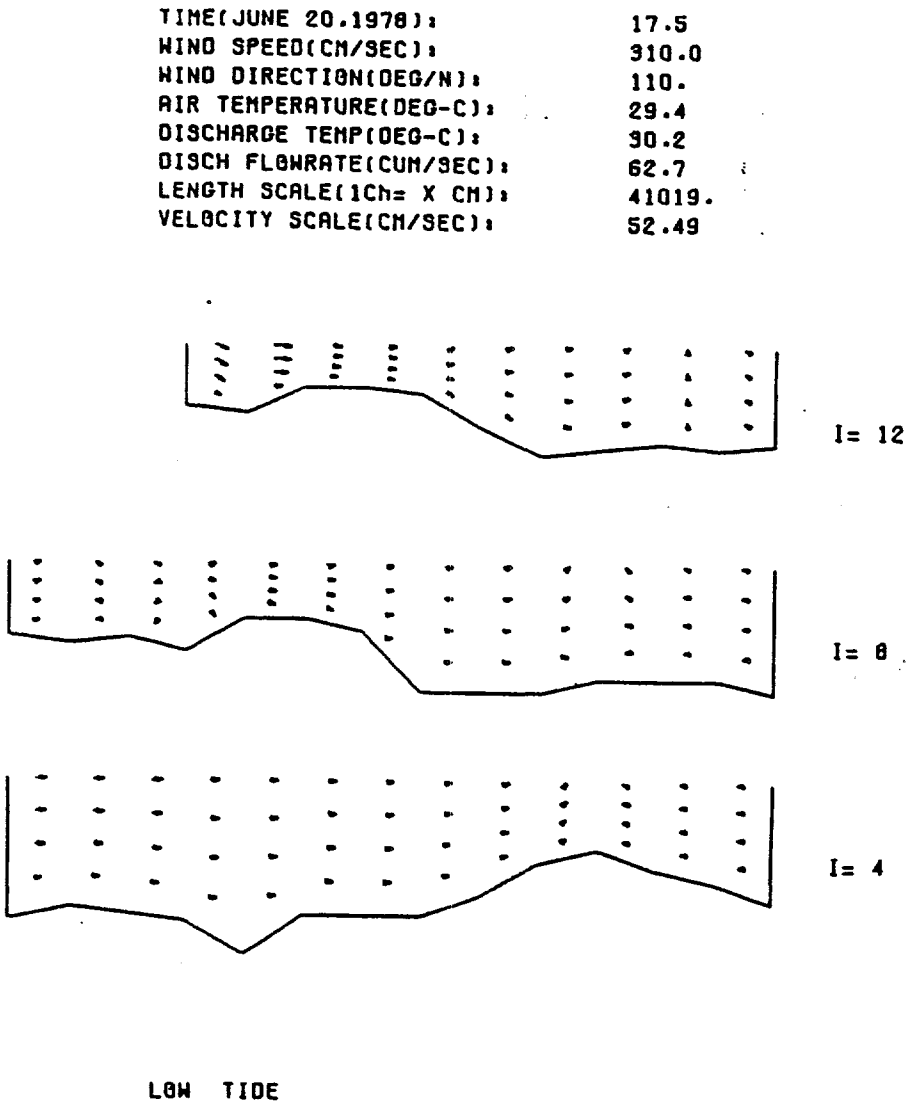

Figure 42. VW velocity, Anclote Anchorage by modeling

TIME(JUNE 20,1978):	17.5
WIND SPEED(CM/SEC):	910.0
WIND DIRECTION(DEG/N):	110.
AIR TEMPERATURE(DEG-C):	29.4
DISCHARGE TEMP(DEG-C):	30.2
DISCH FLOWRATE(CUM/SEC):	62.7
LENGTH SCALE(1CM= X CM):	41019.
VELOCITY SCALE(CM/SEC):	52.49

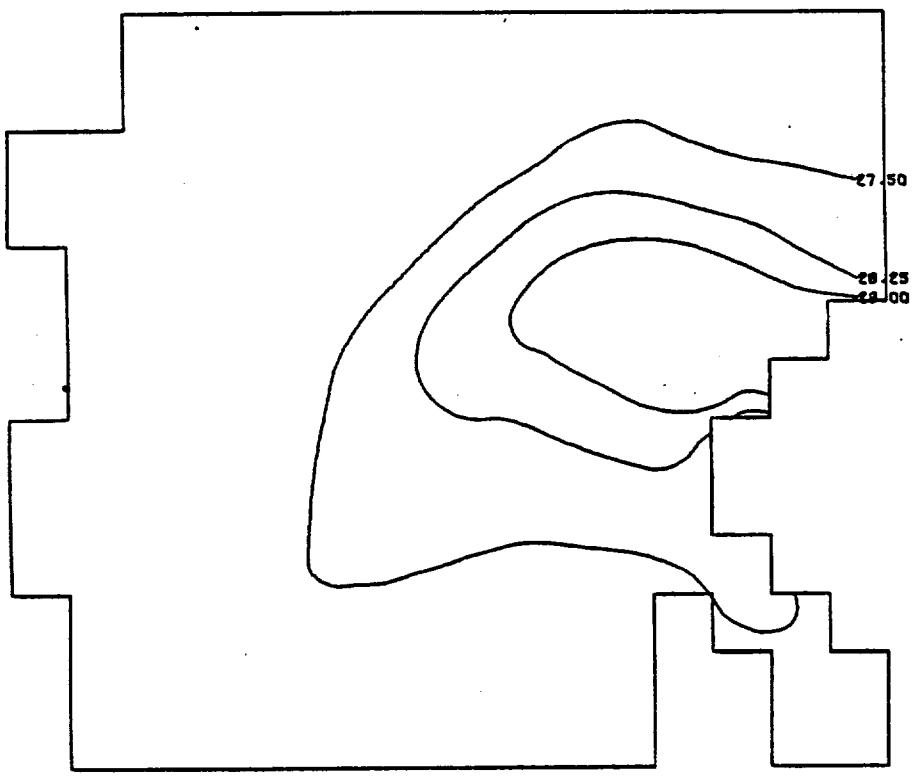

LOW TIDE

Figure 43. Temperature from IR

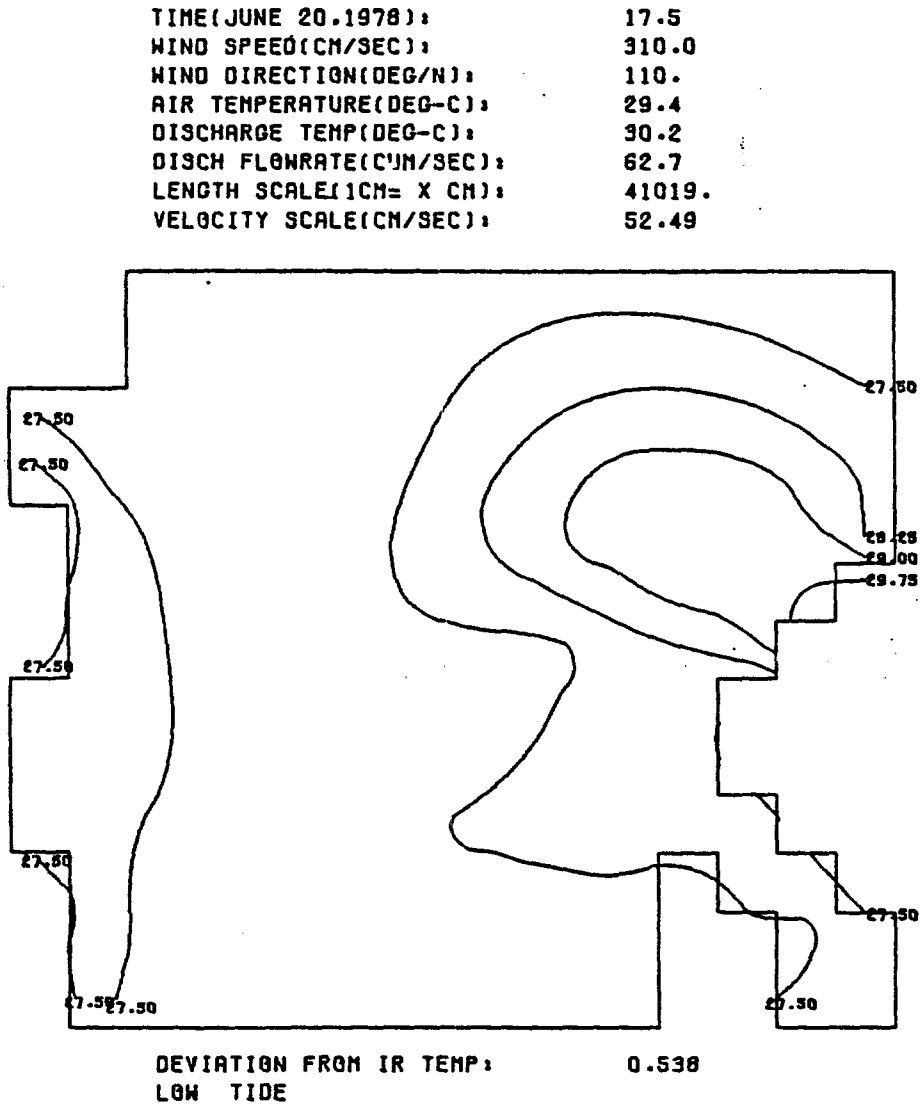

Figure 44. Surface temperature, Anclote Anchorage by modeling

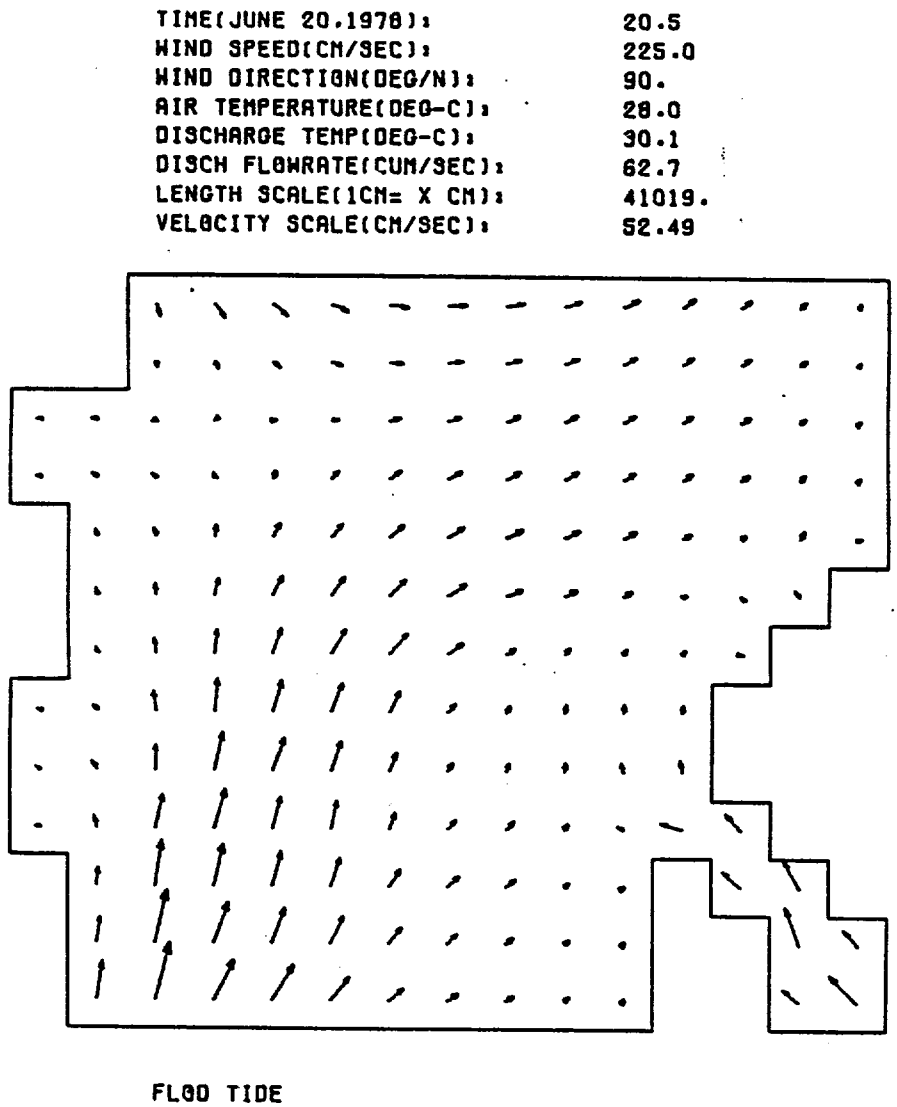

Figure 45. Surface velocity, Anclote Anchorage by modeling

TIME(JUNE 20.1978):	20.5
WIND SPEED(CM/SEC):	225.0
WIND DIRECTION(DEG/N):	90.
AIR TEMPERATURE(DEG-C):	28.0
DISCHARGE TEMP(DEG-C):	30.1
DISCH FLOWRATE(CUM/SEC):	62.7
LENGTH SCALE(1CM= X CM):	41019.
VELOCITY SCALE(CM/SEC):	52.49

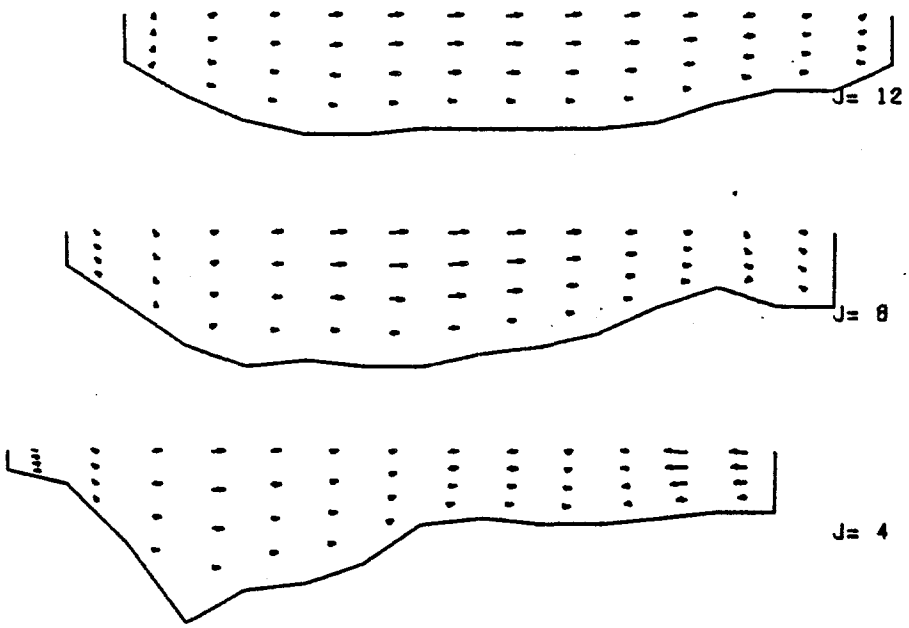

FLOD TIDE

Figure 46. UW velocity, Anclote Anchorage by modeling

TIME(JUNE 20,1978):	20.5
WIND SPEED(CM/SEC):	225.0
WIND DIRECTION(DEG/N):	90.
AIR TEMPERATURE(DEG-C):	28.0
DISCHARGE TEMP(DEG-C):	30.1
DISCH FLOWRATE(CUM/SEC):	62.7
LENGTH SCALE(1CM= X CM):	41019.
VELOCITY SCALE(CM/SEC):	52.49

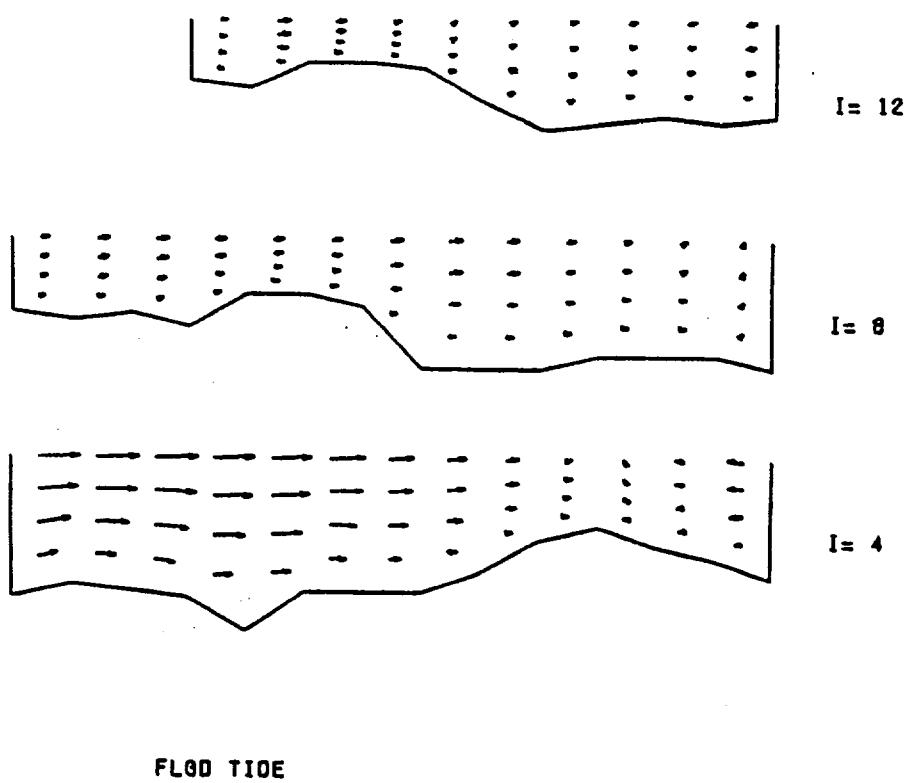

Figure 47. VW velocity, Anclote Anchorage by modeling

TIME(JUNE 20,1978):	20.0
WIND SPEED(CM/SEC):	225.0
WIND DIRECTION(DEG/N):	90.
AIR TEMPERATURE(DEG-C):	28.0
DISCHARGE TEMP(DEG-C):	29.3
DISCH FLOWRATE(CUM/SEC):	62.7
LENGTH SCALE(1CM= X CM):	41019.
VELOCITY SCALE(CM/SEC):	52.49

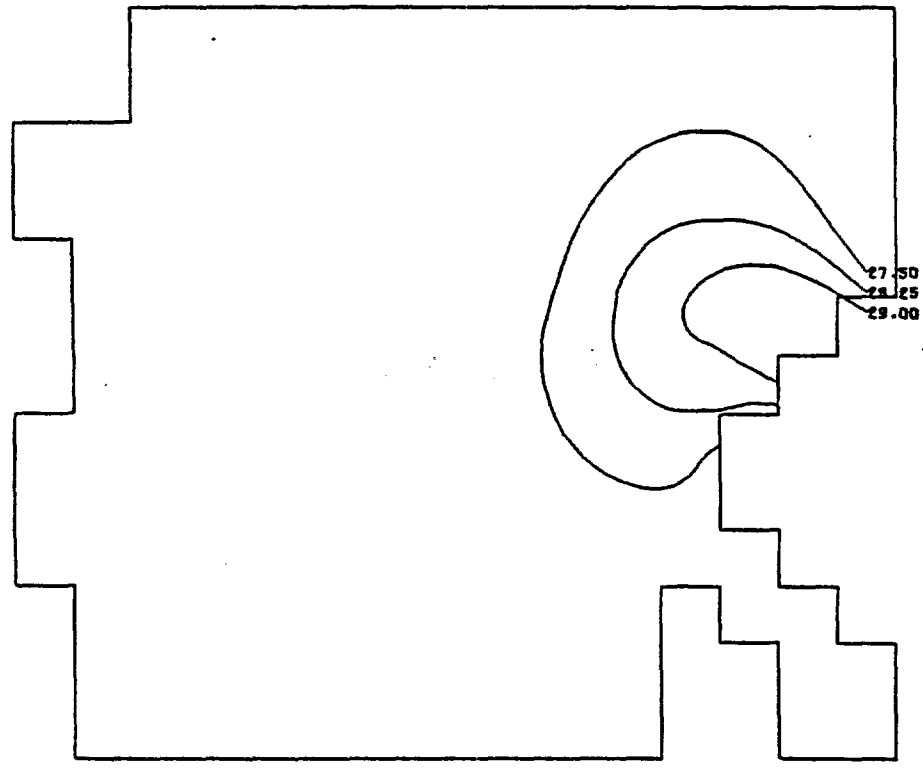

FLOD TIDE

Figure 48. Temperature from IR

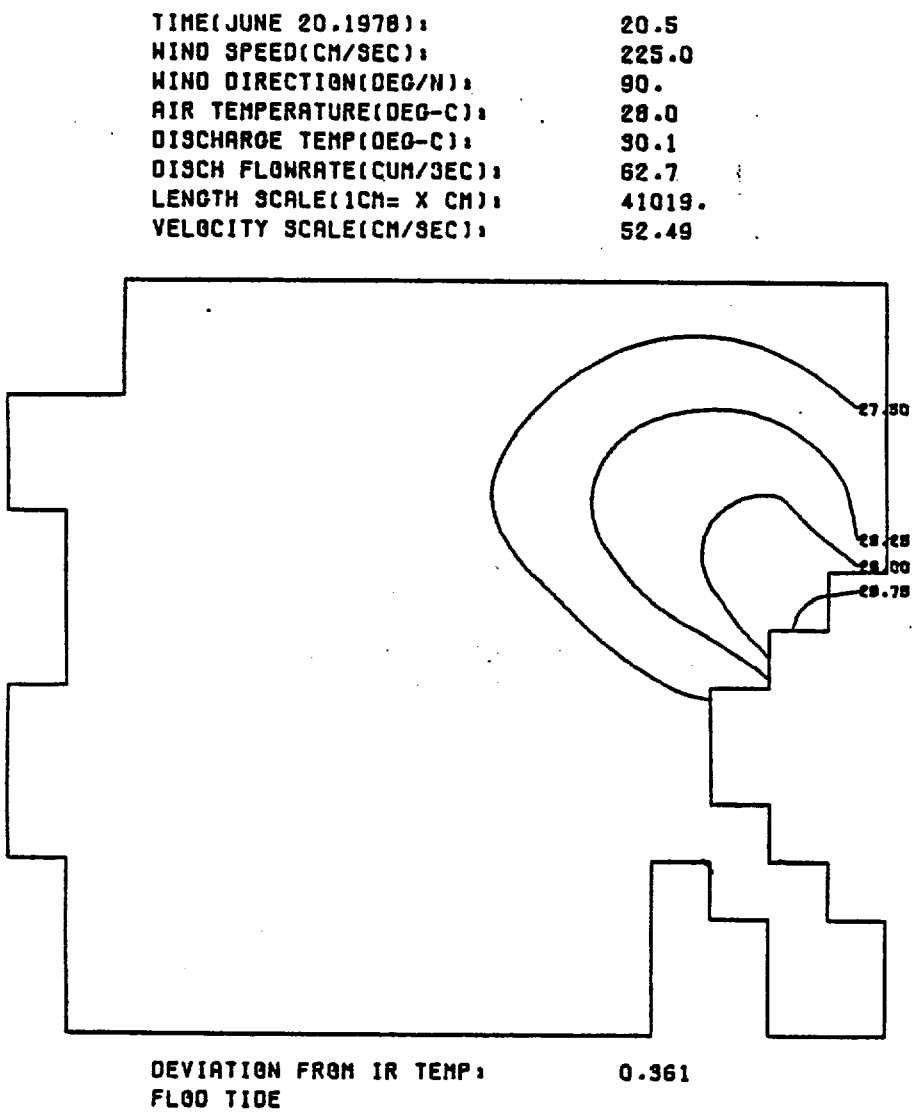

Figure 49. Surface temperature, Anclote Anchorage by modeling

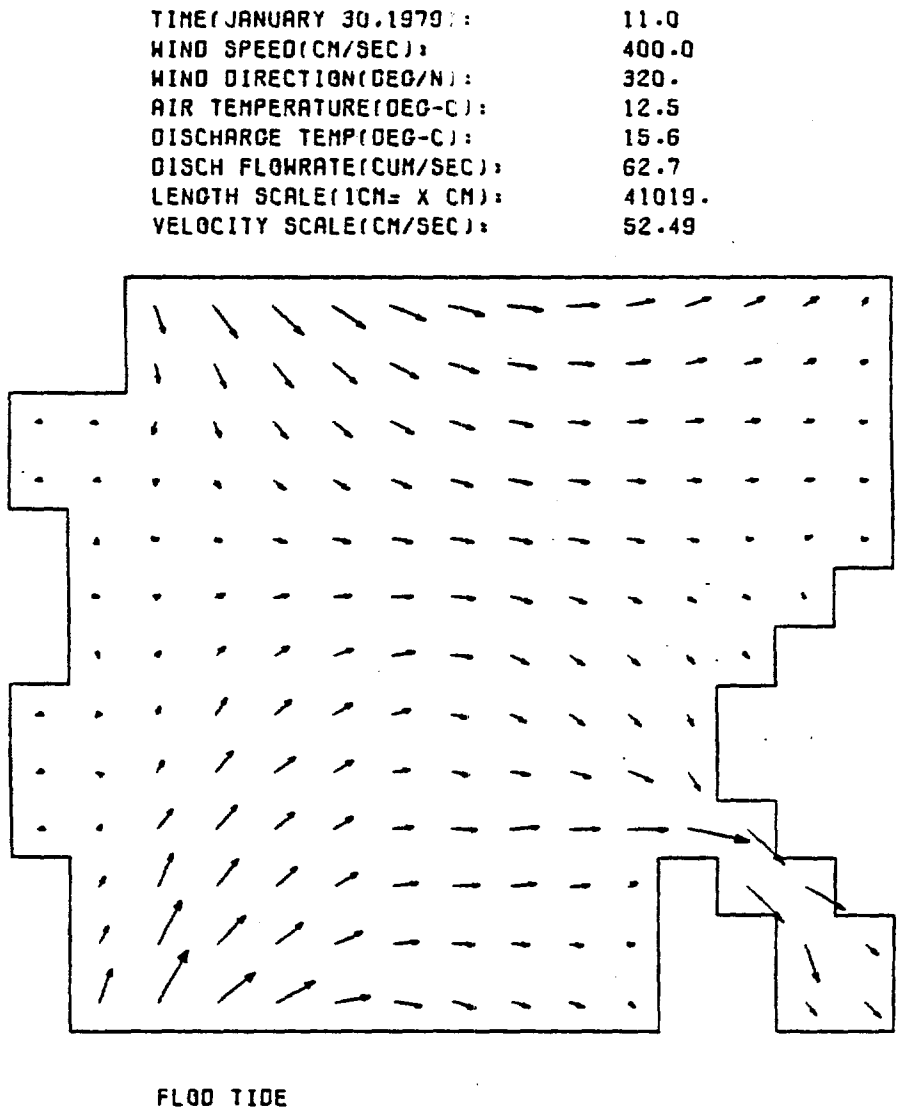

Figure 50. Surface velocity, Anclote Anchorage by modeling

TIME(JANUARY 30,1979):	11.0
WIND SPEED(CM/SEC):	400.0
WIND DIRECTION(DEG/N):	320.
AIR TEMPERATURE(DEG-C):	12.5
DISCHARGE TEMP(DEG-C):	15.6
DISCH FLOWRATE(CUM/SEC):	62.7
LENGTH SCALE(1CM= X CM):	41019.
VELOCITY SCALE(CM/SEC):	52.49

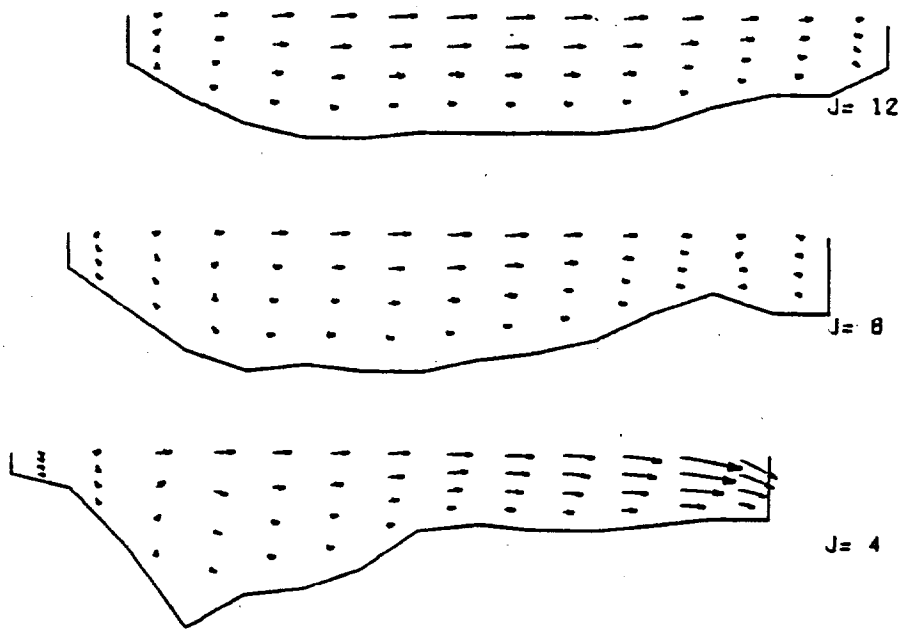

FLOD TIDE

Figure 51. UW velocity, Anclote Anchorage by modeling

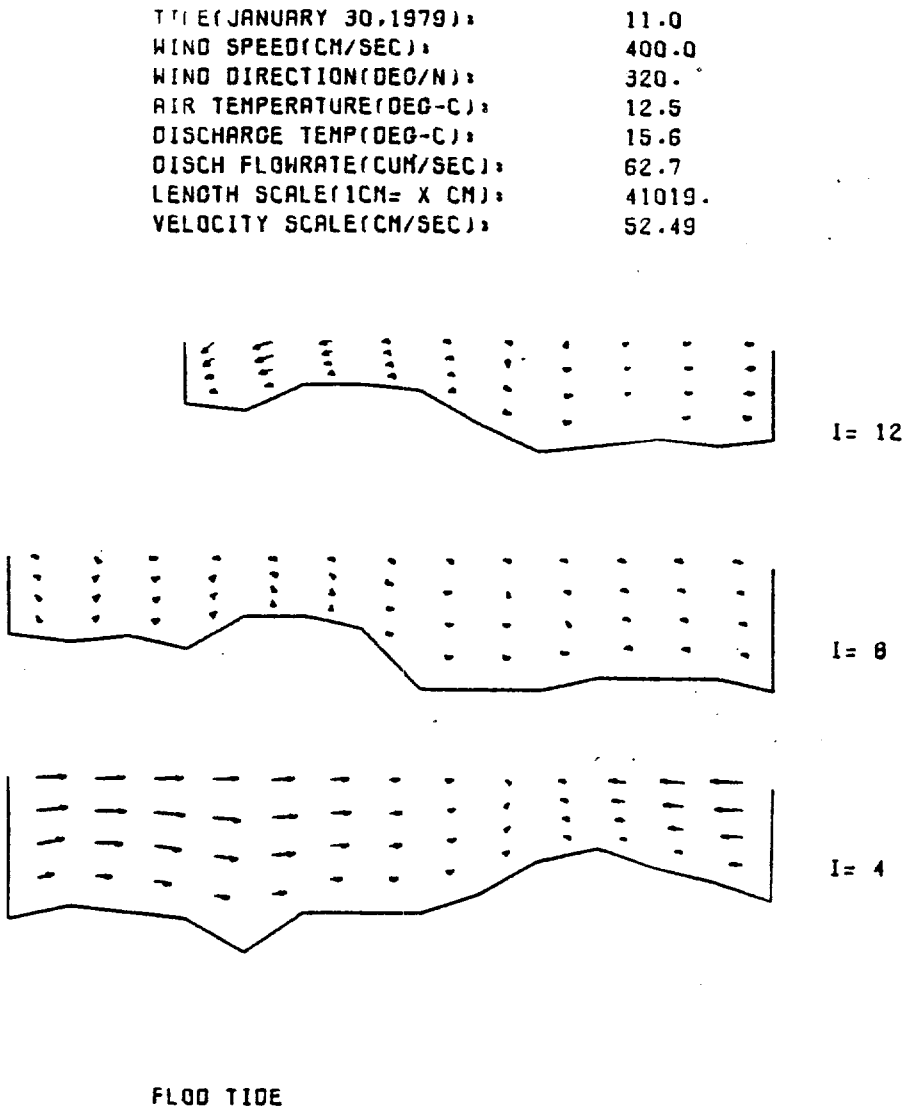

Ficure 52. VW velocity, Anclote Anchorage by modeling

TIME(JANUARY 30,1979):	11.5
WIND SPEED(CM/SEC):	400.0
WIND DIRECTION(DEG/N):	320.
AIR TEMPERATURE(DEG-C):	12.7
DISCHARGE TEMP(DEG-C):	15.5
DISCH FLOWRATE(CUM/SEC):	62.7
LENGTH SCALE(1CM= X CM):	41019.
VELOCITY SCALE(CM/SEC):	52.49

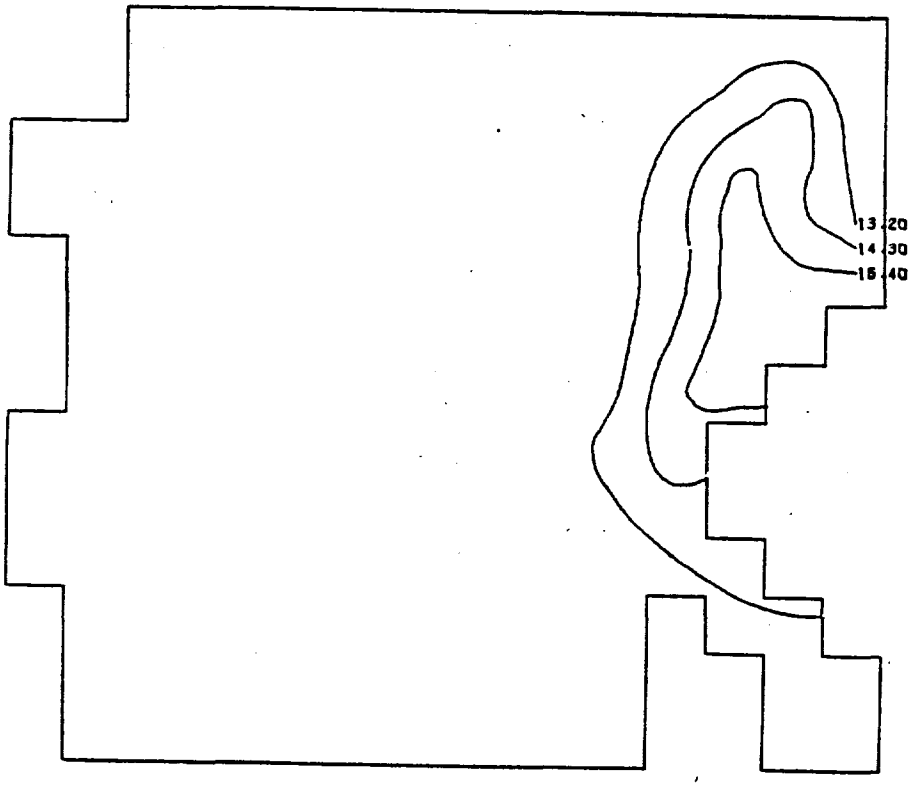

FLOD TIDE

Figure 53. Temperature from IR

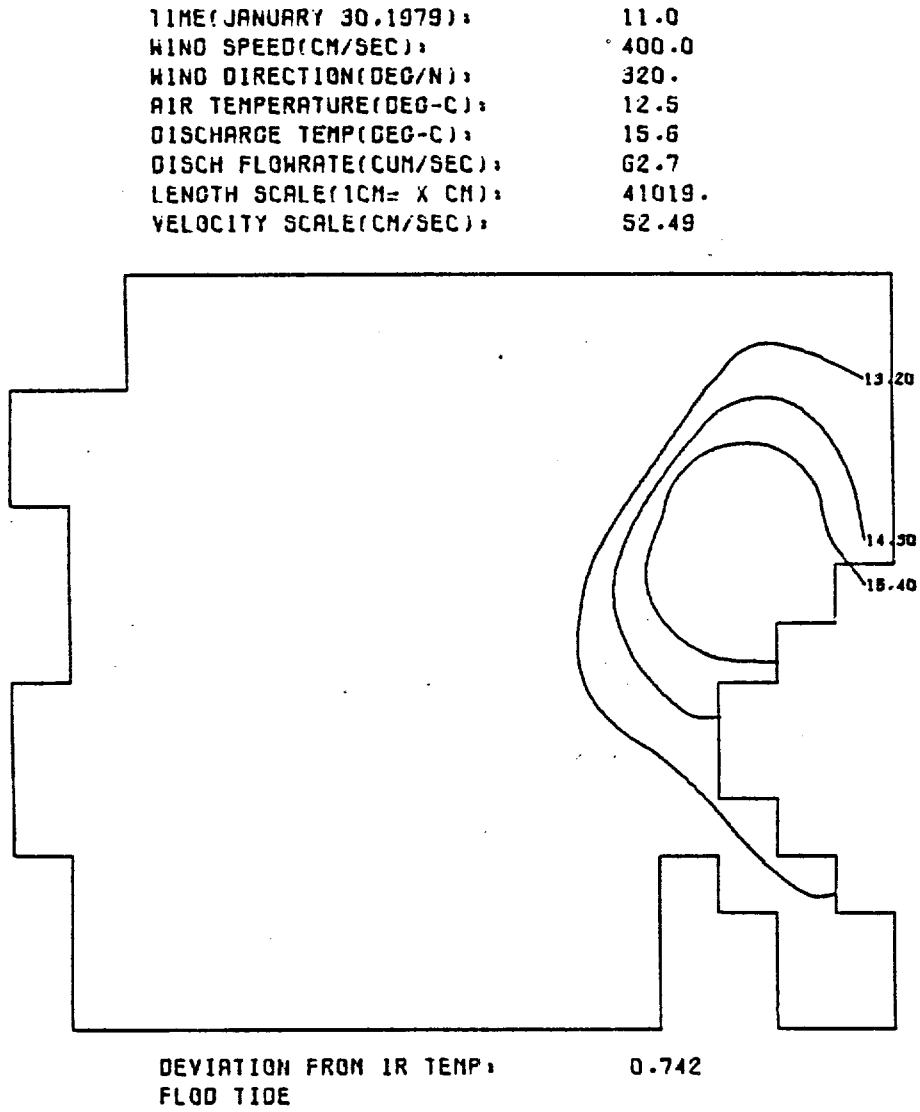

Figure 54. Surface temperature, Anclote Anchorage by modeling

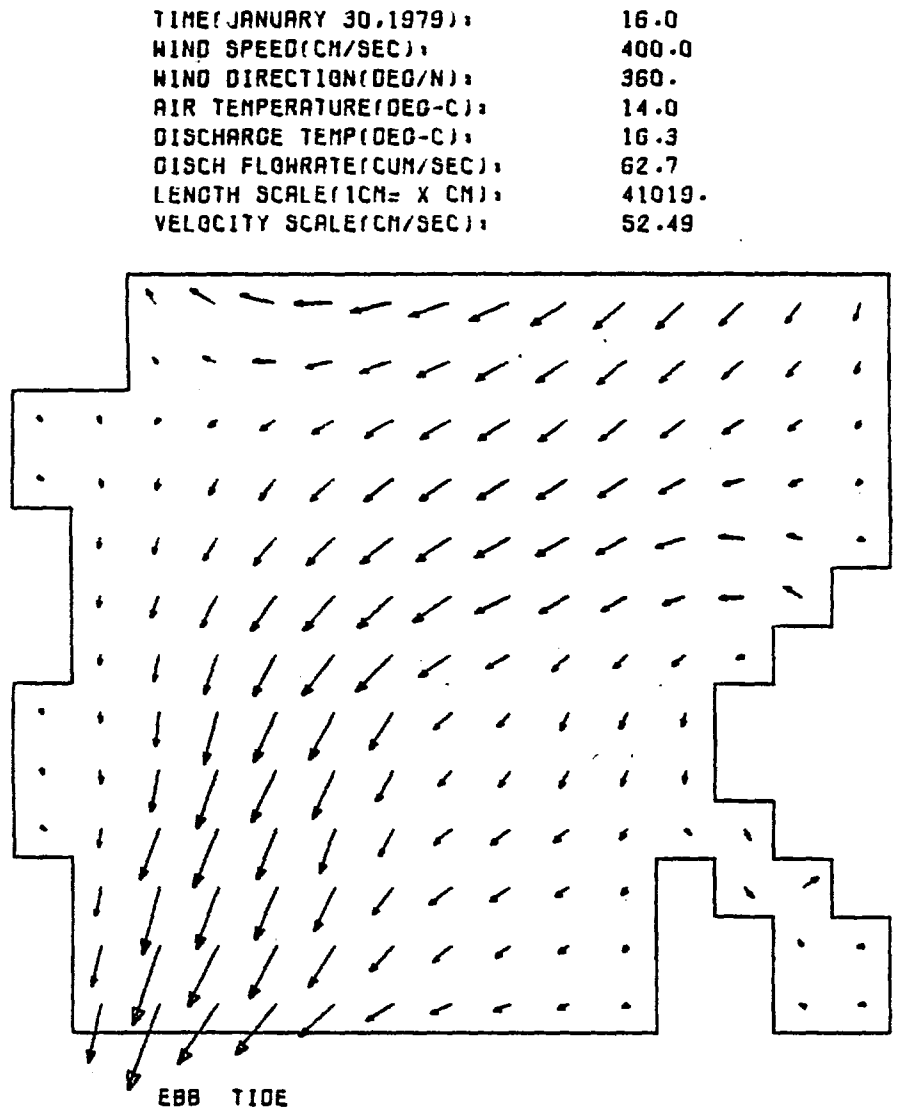

Figure 55. Surface velocity, Anclote Anchorage by modeling

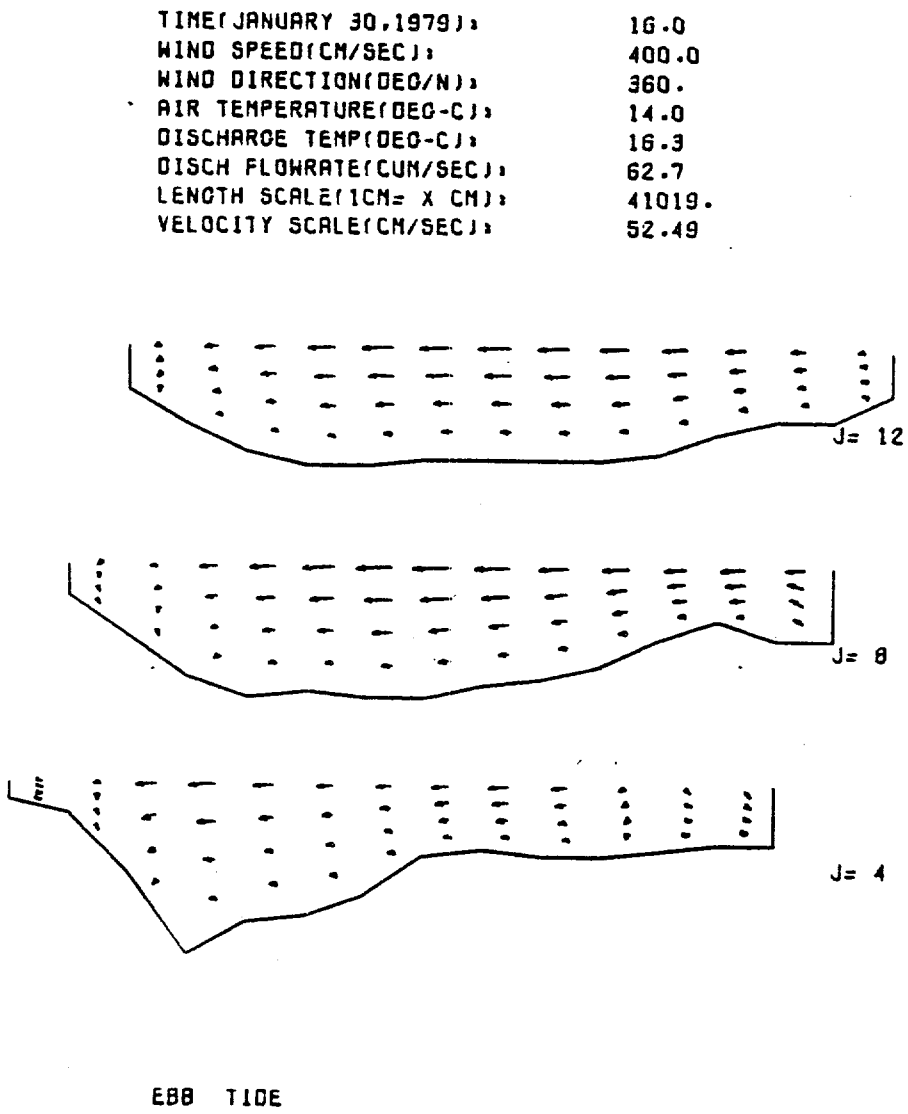

Figure 56. UW velocity, Anclote Anchorage by modeling

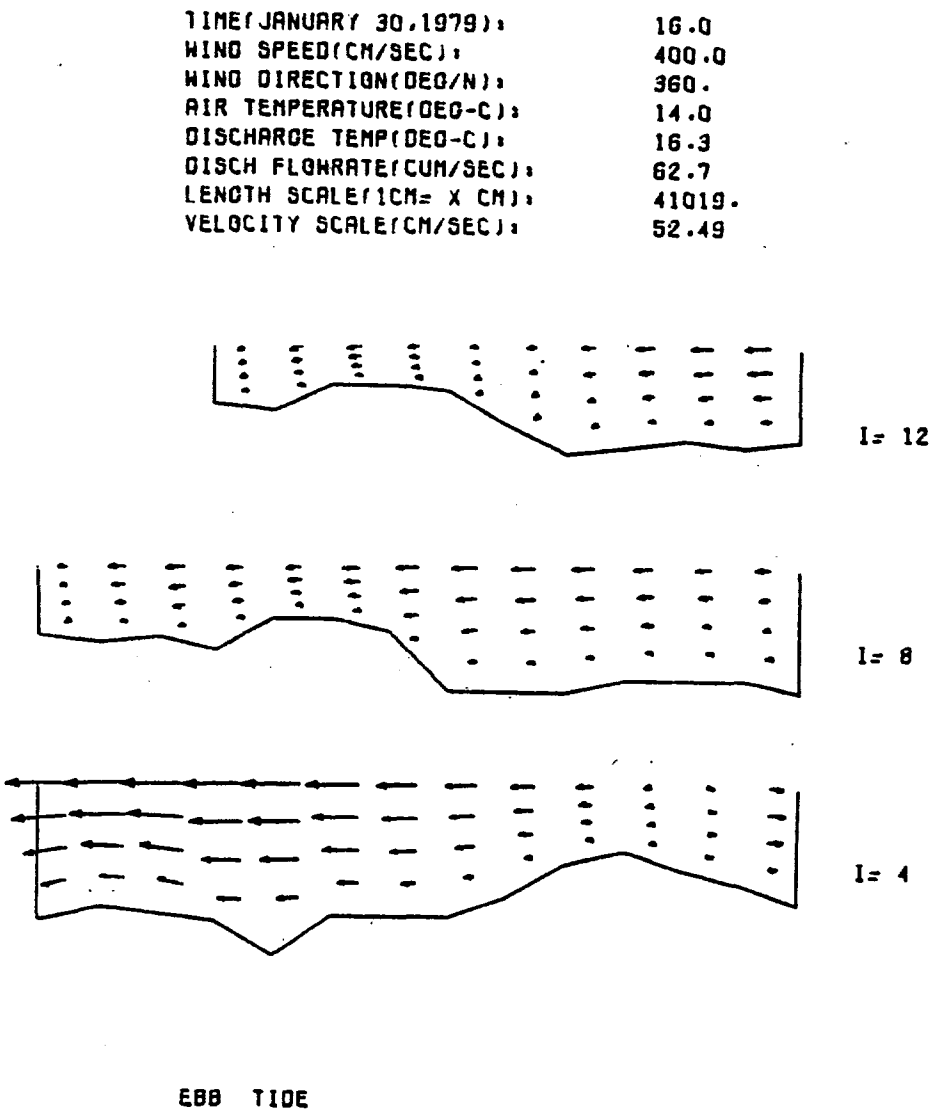

Figure 57. VW velocity, Anclote Anchorage by modeling

TIME(JANUARY 30,1979):	17.0
WIND SPEED(CM/SEC):	400.0
WIND DIRECTION(DEG/N):	360.
AIR TEMPERATURE(DEG-C):	18.0
DISCHARGE TEMP(DEG-C):	16.3
DISCH FLOWRATE(CUM/SEC):	62.7
LENOTH SCALE(1CM= X CM):	41019.
VELOCITY SCALE(CM/SEC):	52.49

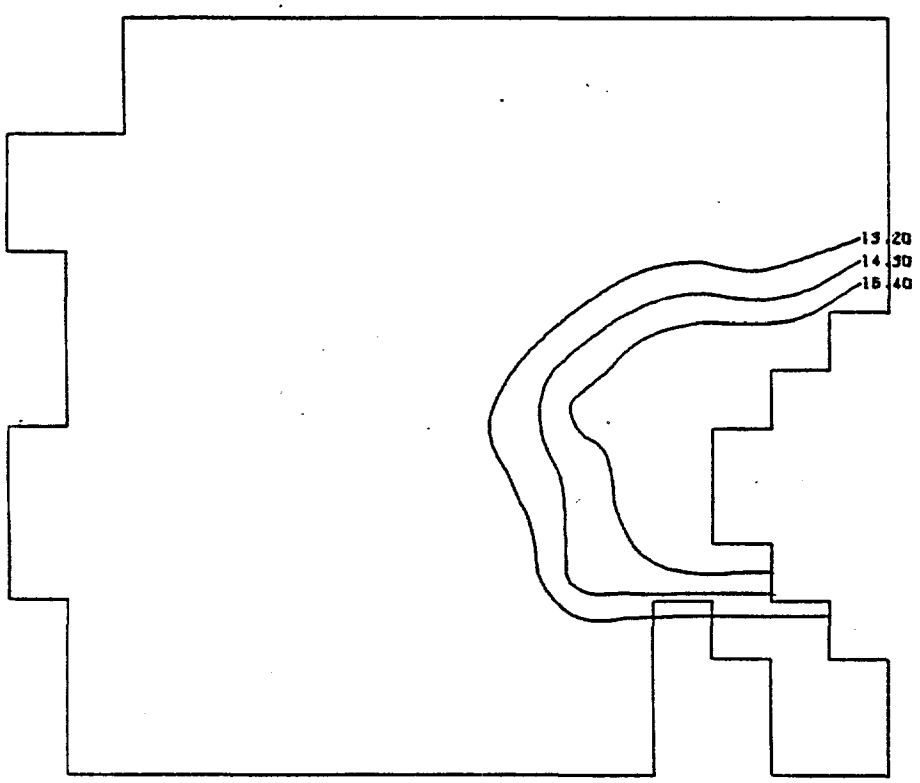

EBB TIDE

Figure 58. Temperature from IR

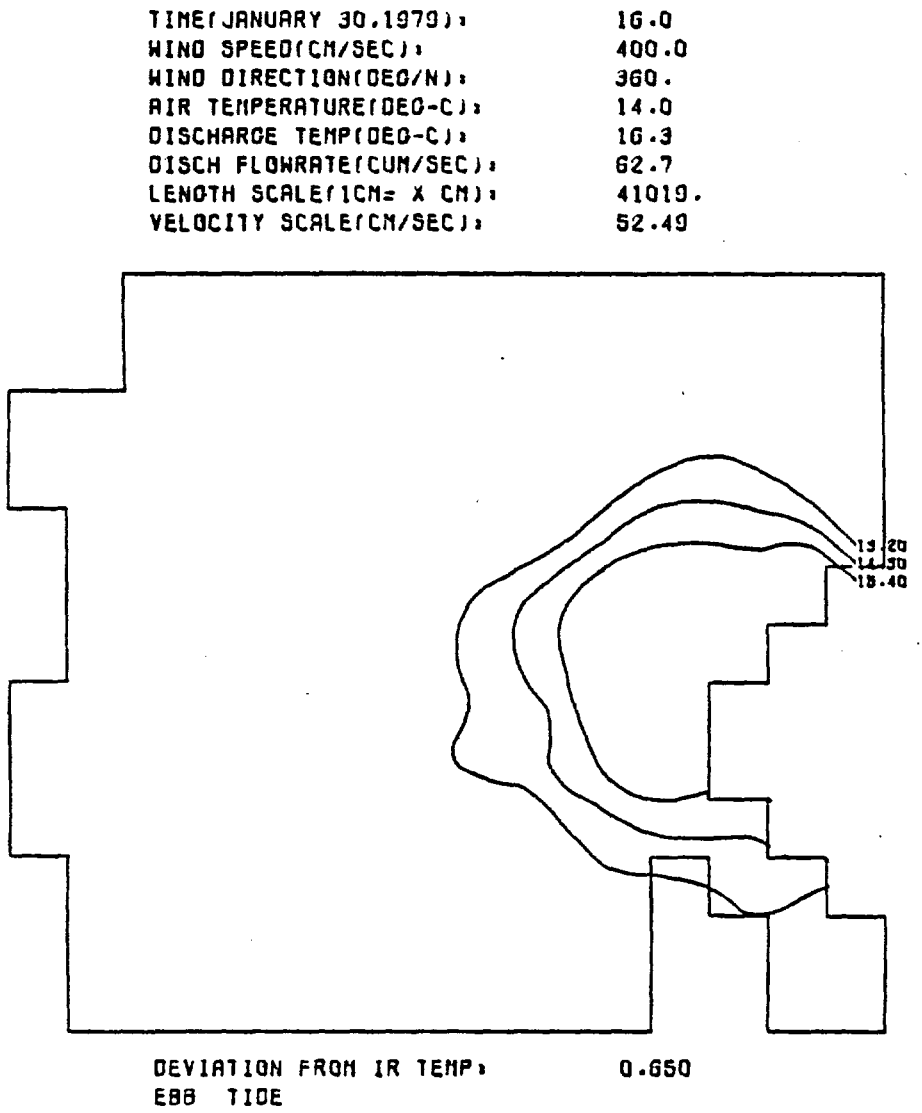

Figure 59. Surface temperature, Anclote Anchorage by modeling

TIME(1ST FEB. ,1979):	16.0
WIND SPEED(CM/SEC):	600.
WIND DIRECTION(DEG/N):	330.0
AIR TEMPERATURE(DEG-C):	11.1
DISCHARGE TEMP(DEG-C):	14.0
DISCH FLOWRATE(CUM/SEC):	62.7
LENGTH SCALE(1CM= X CM):	41019.
VELOCITY SCALE(CM/SEC):	52.49

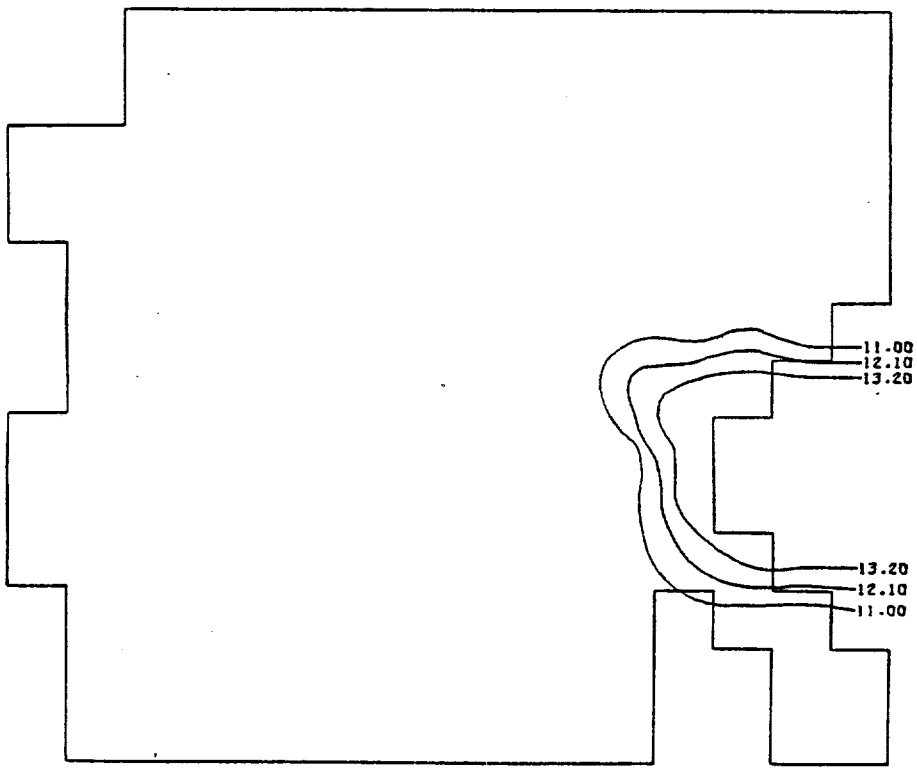

HIGH TIDE

Figure 60. Temperature from IR